Journal of Materials Chemistry A

ROYAL SOCIETY OF CHEMISTRY

REVIEW

View Article Online
View Journal

Cite this: DOI: 10.1039/d4ta08232j

Strategically designed catalysts for ammonia synthesis under mild conditions: recent advances and challenges

Sai Sundara Sandeep Ganti,† Pintu Kumar Roy,† Nayonay Wagh, Kona Naga Surya Siva Sai and Sushant Kumar *

The role of ammonia would continue to be significant in the changing energy landscape with focus on mitigating the carbon footprint per unit of ammonia produced. Since ammonia is a zero-carbon molecule and increasingly considered an important hydrogen energy carrier for future energy systems, its generation under mild conditions and subsequent industrial acceptance are critical. Therefore, the recent challenges include designing and engineering alternative greener methods that can generate ammonia at low input energy and facilitate inexpensive, localized, and renewable energy-coupled ammonia generation. This review underscores the recent developments in the design strategies of novel catalysts, particularly emphasizing the recent advances in different classes of thermal, electrochemical, and non-thermal plasma catalysis that can generate ammonia under mild conditions. Hence, this article can serve as a comprehensive work for engineering novel catalysts and methods, contributing to the generation of sustainable and cost-efficient solutions for expanding the landscape of ammonia applications.

Received 19th November 2024
Accepted 20th March 2025

DOI: 10.1039/d4ta08232j

rsc.li/materials-a

1. Introduction

With the massive increase in the human population following the industrial revolution in the 19th century, there was a fear that mankind would suffer from an acute shortage of food. Fixed nitrogen was found to be a crucial component of fertilisers that promoted healthy crop growth, and most of the nitrogen-containing fertilisers were obtained from nitrate reserves that were limited. Amidst rising concerns of the complete exhaustion of these reserves, there was a pressing need to come up with a scalable method for nitrogen fixation. A major breakthrough occurred in the year 1908, when German chemist Fritz Haber invented a method for ammonia synthesis at high temperature and pressure using a closed circulatory system, which was later industrialised by Carl Bosch. Both scientists received a Nobel Prize for their contribution in developing the process, which is now known as the Haber–Bosch (HB) method for ammonia synthesis and regarded by many as the greatest invention of the 20th century.

The development of this large-scale ammonia production method made fertilisers affordable and readily available, exponentially increasing the crop production. Consequently, Haber's invention is credited to have saved the lives of millions of people, playing a pivotal role in the population growth. To this day, the HB process remains the dominant mode of production of ammonia. Ammonia is the second largest commercially manufactured chemical in the world at an annual production rate of almost 200 million metric tons, with the capacity reaching nearly 240 million metric tons.[1,2] Roughly 80% of the ammonia produced is used for making fertilisers, and ammonia-based nitrogenous fertilisers, indirectly, feed almost 70% of the global population.[3] It is estimated that nearly half of the nitrogen in our body comes from ammonia synthesized in plants.[4]

In addition to fe rtilizers, ammonia is also a building block for the production of many pharmaceuticals and commercial chemicals, such as nitric acid, hydrazine, cyanides and amino acids.[5] It is also commercially used as a refrigerant in large freezing and refrigeration plants because it has high volatility and a high latent heat of vaporisation during phase change from liquid state to gaseous state.[6] The development of CFCs (chlorofluorocarbons) in the early 20th century resulted in a decline in the use of ammonia as a refrigerant, but upon the subsequent discovery of the contribution of CFCs to ozone depletion, a global phase-out of these CFCs was called for under the Montreal Protocol in the year 1989. This shifted the focus back to ammonia, as it is highly energy efficient and also poses the advantage of having a zero rating for both Ozone Depletion Potential (ODP) and Global Warming Potential (GWP), apart from being less expensive and more efficient than CFCs.[6,7] Another common use of ammonia is as a cleaning agent to

Gas-Solid Interaction Laboratory, Department of Chemical and Biochemical Engineering, Indian Institute of Technology Patna, Bihta, Patna, 801106, Bihar, India. E-mail: sushantkumar@iitp.ac.in

† Authors contributed equally.

remove stains because of its ability to dissolve dirt and grime. It evaporates rapidly after application, not leaving behind any streaks on glass surfaces.[8]

Lately, ammonia has gained widespread attention due to its ability to act as an efficient hydrogen carrier. Storing hydrogen as a liquid requires a cryogenic temperature of −253 °C, and compressed hydrogen requires vessels capable of withstanding a pressure of 70 MPa at ambient temperature. Storing and transporting hydrogen is also risky due to the high flammability and low ignition energy of hydrogen gas.[9] However, ammonia can be liquefied at −33 °C (at atmospheric pressure) or at 0.8–1.0 MPa (at 20 °C), making it much easier to store and transport. Liquid ammonia has a greater volumetric hydrogen density than liquid hydrogen. At −253 °C and 0.1 MPa, liquid hydrogen has a density of 70 kg_{H_2} m^{-3}, whereas liquid ammonia at 27 °C and 1.0 MPa has nearly 106 kg_{H_2} m^{-3}.[10] Liquefied ammonia also has a greater energy density (3.83 MW h m^{-3}) than that of liquid hydrogen (2.64 MW h m^{-3}).[11] Therefore, ammonia can easily be transported using the current infrastructure of fossil fuels, giving rise to a broader supply chain, where it can be catalytically cracked to produce hydrogen gas at a site of distribution and use.[12,13]

Due to the above-mentioned reasons, ammonia is being extensively studied for use in internal combustion engines as it seems to be a promising carbon-free fuel. Ammonia has a high octane rating (110–130 *versus* gasoline at 86–93) and a narrow flammability range, and it can increase the engine's compression ratio, resulting in a higher cycle thermal efficiency.[14] However, due to its high ignition energy and low calorific value, it is challenging to directly use pure ammonia as a fuel.[15] Therefore, it is often blended with other fuels, which helps combat the problems of low burning velocity and narrow the flammability range of ammonia, thus enhancing its combustion characteristics.[16] When pure ammonia is ideally combusted ($2NH_3 + 3/2O_2 \rightarrow N_2 + 3H_2O$), it undergoes an exothermic reaction releasing N_2 and H_2O.[17] However, it was found that ammonia practically undergoes incomplete combustion to release NO_x (nitrogen oxides), which cause even more environmental damage than CO_2.[15] The NO_x emission could be mitigated using selective catalytic reduction and recirculation of exhaust gas in the combustion chamber.[18]

It was found that ammonia could be used as a fuel in solid oxide fuel cells (SOFCs), where NO_x formation could be avoided whilst achieving a higher efficiency than that of internal combustion engines.[19,20] SOFCs do not require external cracking of ammonia, and the ammonia decomposition reaction (endothermic) could be combined with the electrochemical reaction (exothermic), eliminating the need for a complex design to increase the thermodynamic efficiency.[21] Thus, due to its vast potential to act as an alternative clean fuel, ammonia-fueled ships have become a reality and its applications as a fuel could soon be expanded to the aviation sector by using it to power aircrafts.[17,22] Ammonia could therefore be used as an energy source across multiple sectors, replacing conventional fossil fuels in any application. The combustion of this "replacement fossil fuel" produces only nitrogen and water, which could again be reused for ammonia production and hydrogen generation, resulting in a sustainable circular economy. Fig. 1 depicts the concept of a circular ammonia economy, envisioned by MacFarlane *et al.* in their article.[12]

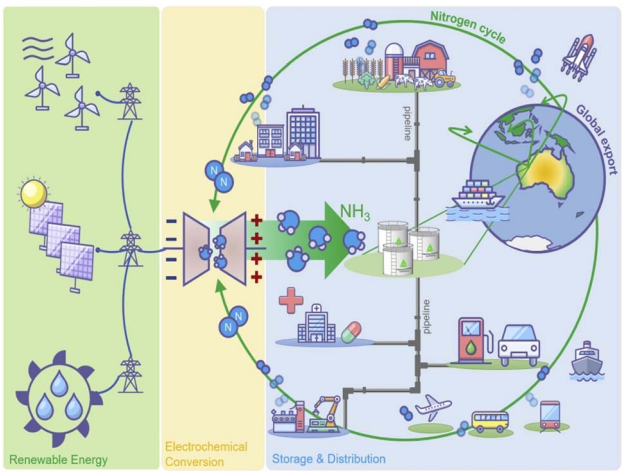

Fig. 1 "Ammonia economy": a model system in which ammonia acts as the central currency for all energy vectors or uses. Adapted with permission from ref. 12. Copyright 2020, Elsevier.

1.1 Thermodynamics

$$N_2 + 3H_2 \rightleftharpoons 2NH_3;\ \Delta H^\circ = -92\ \text{kJ mol}^{-1} \quad (1)$$

Since the forward reaction of ammonia formation is exothermic and reversible, a low temperature favours this reaction.[23] Increasing the pressure shifts the equilibrium to the side with fewer number of moles (according to the Le Chatelier's principle), so it is evident that high pressure would favour the forward reaction of ammonia formation.[24] Thus, the most favourable theoretical operating conditions for the ammonia synthesis reaction are low temperatures and high pressures.[25] Although the theoretical equilibrium concentration of ammonia can be close to 100% at low temperatures and high pressures, the ammonia formation rate is sluggish, making the process very uneconomical from a production point of view.[24] Both nitrogen and hydrogen dissociate at higher temperatures, hence the reaction is carried out at a higher temperature, going against Le Chatelier's principle to make large-scale production more feasible. Notably, at such high temperatures, the equilibrium shifts towards a reverse reaction, *i.e.*, ammonia decomposition to nitrogen and hydrogen, resulting in a lower generation rate. The dependence of the ammonia yield on the reaction temperature and pressure can be found in Fig. 2. We can see that the equilibrium concentration of ammonia significantly reduces as the temperature is increased. Thus, it is necessary to develop an efficient catalyst that could operate under optimum conditions, where neither the reaction rate nor the ammonia yield is compromised.

To optimize the operating conditions, a detailed mechanistic understanding of catalytically produced ammonia from nitrogen and hydrogen is essential. Based on extensive surface

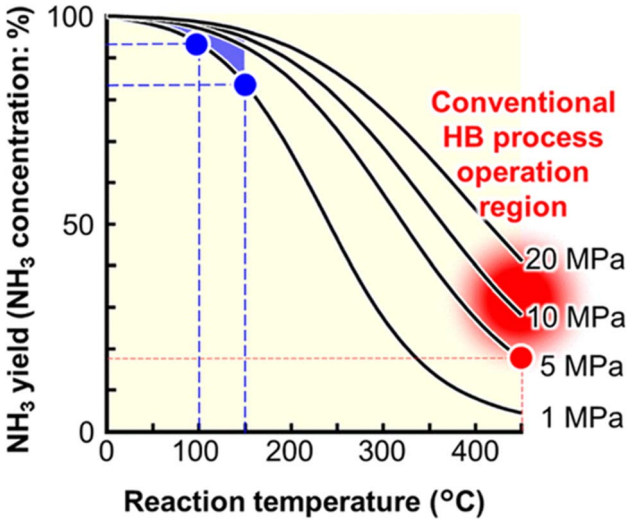

Fig. 2 Temperature- and pressure-dependent production of ammonia with the corresponding yields (%). Adapted from the work of Hattori *et al.*,[26] licensed under CC BY 4.0 (https://creativecommons.org/licenses/by/4.0/).

science experiments, it is widely concluded that the dissociative adsorption of N_2 is the rate-determining step.[27] Interesting, Ertl *et al.* investigated nitrogen interaction on both Fe(100) and Fe(111) surfaces in a wide temperature region (−133–727 °C) using numerous techniques such as Auger electron spectroscopy, thermal desorption spectroscopy, work function measurements, UV photoelectron spectroscopy, and low-energy electron diffraction and found that nitrogen adsorption is the rate-limiting step.[28] Even though numerous experiments have been reported, there is still unclear understanding of the exact mechanistic details for ammonia synthesis. In particular, it is unclear whether N_2 dissociates directly over the catalyst surface or on some intermediates. The experimental observations vary with metals and crystal faces and under different conditions.[29,30] However, under industrial conditions (*i.e.*, high temperature and pressure), such difference in mechanism is most notable.

In one of the previous works of our research group, the expression for the rate-determining step (RDS) for the synthesis of ammonia was determined by fitting the modelled rate equations to observed reaction rates.[31] The rate equations were generated assuming the working mechanism as the Langmuir–Hinshelwood mechanism.[32–34] The following sequence of elementary steps is involved in the overall reaction:

$$H_2(g) \rightarrow H_2(ads) \quad (2)$$

$$N_2(g) \rightarrow N_2(ads) \quad (3)$$

$$H_2(ads) \rightarrow 2H(ads) \quad (4)$$

$$N_2(ads) \rightarrow 2N(ads) \quad (5)$$

$$N(ads) + H(ads) \rightarrow NH(ads) \quad (6)$$

$$NH(ads) + H(ads) \rightarrow NH_2(ads) \quad (7)$$

$$NH_2(ads) + H(ads) \rightarrow NH_3(ads) \quad (8)$$

$$NH_3(ads) \rightarrow NH_3(g) \quad (9)$$

Here, (g) and (ads) refer to gas-phase and adsorption species, respectively. Among the above-mentioned steps, eqn (5)–(8) govern the overall reaction rate owing to the large activation energy. Here, under the employed reaction conditions, it was observed that P_{NH_3} was considerably smaller than P_{N_2} and P_{H_2} at the outlet. Therefore, it becomes logical to eliminate P_{NH_3} term and obtain the following final rate equations:[35–37]

$$r = \frac{\overrightarrow{k_4} K_2 P_{N_2}}{\left(1 + K_1 P_{H_2} + K_2 P_{N_2} + \sqrt{K_1 K_3 P_{H_2}}\right)^2} \quad (10)$$

$$r = \frac{\overrightarrow{k_5}\sqrt{K_1 K_2 K_3 K_4}\sqrt{P_{H_2} P_{N_2}}}{\left(1 + K_1 P_{H_2} + K_2 P_{N_2} + \sqrt{K_1 K_3 P_{H_2}} + \sqrt{K_2 K_4 P_{N_2}}\right)^2} \quad (11)$$

$$r = \frac{\overrightarrow{k_6} K_1 K_3 K_5 \sqrt{K_2 K_4}\sqrt{P_{H_2} P_{N_2}}}{\left(1 + K_1 P_{H_2} + K_2 P_{N_2} + \sqrt{K_1 K_3 P_{H_2}} + \sqrt{K_2 K_4 P_{N_2}} + K_5\sqrt{K_1 K_2 K_3 K_4 P_{H_2} P_{N_2}}\right)^2} \quad (12)$$

$$r = \frac{\overrightarrow{k_7} K_1 K_3 K_5 K_7 \sqrt{K_1 K_2 K_3 K_4}\sqrt{P_{H_2} P_{N_2}}}{\left(1 + K_1 P_{H_2} + K_2 P_{N_2} + \sqrt{K_1 K_3 P_{H_2}} + \sqrt{K_2 K_4 P_{N_2}} + K_5\sqrt{K_1 K_2 K_3 K_4 P_{H_2} P_{N_2}} + K_1 K_3 K_5 K_6 \sqrt{K_2 K_4 P_{H_2} P_{N_2}}\right)^2} \quad (13)$$

where $\overrightarrow{k_4}$, $\overrightarrow{k_5}$, $\overrightarrow{k_6}$, $\overrightarrow{k_7}$ are the rate constants for forward reactions (5)–(8), and K_i is the equilibrium constant in step i. Eqn (10)–(13) are generated assuming that the steps in (5)–(8) are the rate-determining steps (RDSs), respectively. To identify the RDS for ammonia synthesis, the derived equations are fitted into observed experimental rates using a least squares method. Finally, the procedure enables determining which equation best fits and explains the experimental rates.

1.2 Challenges in industrial ammonia production

Over the past few decades, various catalysts were extensively studied and developed in efforts to optimise the HB process. Fig. 3 outlines the timeline of different types of catalysts developed over the last few decades.

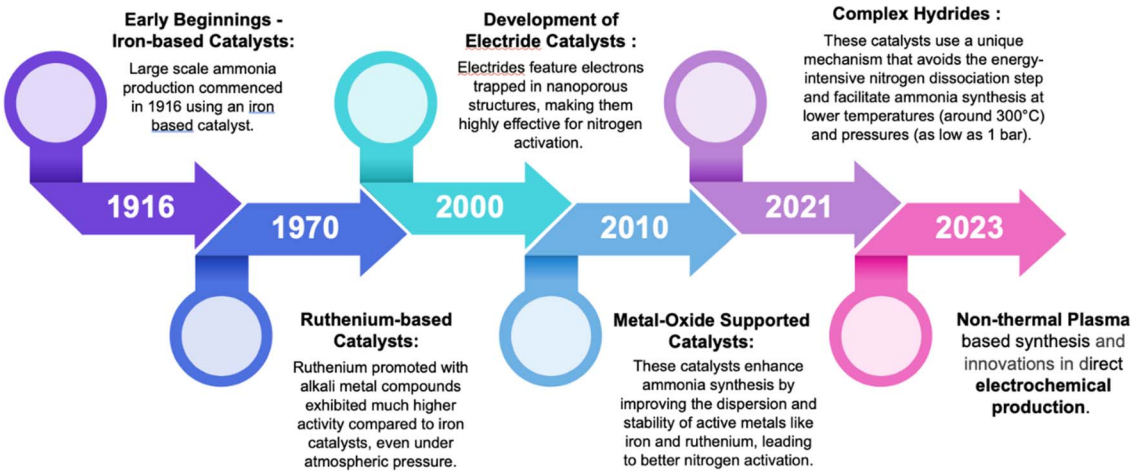

Fig. 3 Timeline showing the development of various catalysts for ammonia synthesis.

Iron catalyst is used in the present-day HB process, with operating conditions (high temperature) going against Le Chatelier's principle to make commercial production more viable. Operating under such harsh conditions consumes enormous energy, owing to both heating and pressurisation, and despite all of this, the resulting yield is nearly 30–40%.[25,26] The low conversion rate of this process calls for an additional recirculation system and a larger reactor, with the unreacted hydrogen and nitrogen being recycled and mixed with the new feedstock, leading to a higher capital and operational cost.[38] Therefore, significant efforts have been made in catalyst development for ammonia synthesis over the past few decades, yet ammonia production accounts for about 2% of the global energy consumption.[39,40]

Alternative methods of ammonia synthesis such as electrochemical and NTP methods, which are discussed in detail in the later part of this paper, may seem as promising alternatives to the HB process as they are completely carbon free and could also be driven by renewable energy sources such as solar and wind energies. They also facilitate the production of ammonia at room temperature and atmospheric pressure, and are also compatible with on-demand, on-site production. However, they are unlikely to achieve the necessary scale and cost to compete with the conventional method as of yet, and hence the HB process is still going to be the dominant method of ammonia production in the foreseeable future.[41]

Considering the aforementioned challenges, it is obvious that new catalysts that can work under mild conditions in a given ammonia synthesis convertor could address some of the prevalent issues such as higher compressor duty and expensive construction materials for ammonia synthesis process. Over these years, several different convertors have been designed and can be broadly categorized as tube-cooled convertors and quench convertors. In general, the ammonia synthesis loop consists of a catalytic ammonia converter; a compressor to attain the desired operating pressure and to recycle the stream before injection into the converter and a condenser to separate the produced ammonia.

Expectedly, the synthesis loop at lower pressures will remarkably reduce the compressor duty, and lower-pressure-rated design materials can also be employed as construction materials. However, once ammonia is condensed and separated, the synthesis loop pressure is reduced, and therefore, the refrigerator power has to be increased to attain the lower temperatures necessary for separation. To operate at low ammonia synthesis loop pressure (*ca.* <10.0 MPa) and achieve the required conversion per pass, it has been suggested to place an ammonia absorption reactor consisting of crystalline salts before the condensation step. The absorption of ammonia should be performed at a partial pressure as low as 0.0002 MPa at moderate temperatures.[42–44]

Similarly, at a lower temperature, the theoretical maximum conversion for ammonia is increased (see Fig. 2). However, convertors operating at relatively low temperatures should be equipped with a better heat removal system, as the ammonia synthesis is an exothermic reaction. Importantly, there has a been significant reduction in operating pressure while maintaining viable condenser temperatures and also a remarkable

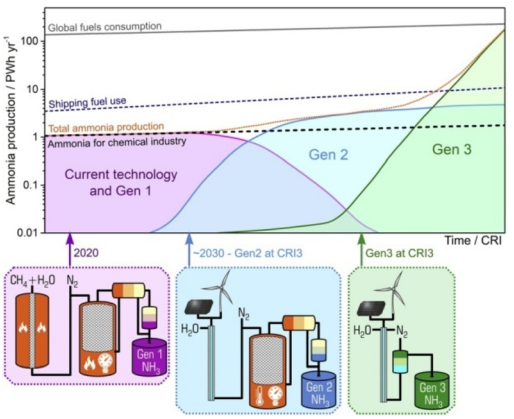

Fig. 4 Forecasted shares of the current and future ammonia production technologies. Adapted with permission from ref. 12. Copyright 2020, Elsevier.

increase in conversion at a lower temperature has been reported that could have limitation on convertor heat removal efficiency. Therefore, the implementation of active catalysts that exhibit improved activity at lower pressures and temperatures would need modifications in the loop designs. Herein, we summarize the activity of catalysts operating at lower temperatures and pressures in a categorical manner, including conventional thermal catalysts and emerging catalysts for electrochemical and NTP processes.

In the future, ammonia economy is expected to grow in line with the increasing global energy consumption and ammonia demand, especially for fertilizers and shipping fuel. Ammonia production will remain dominated by current HB technology, transitioning to Gen 1 with CO_2 sequestration in the next decade. Gen 2, involving green hydrogen, will become commercially viable around 2030, gradually replacing existing methods. Gen 3, fully electrochemical and renewable-powered, will emerge by the end of the decade, initially for ammonia as a maritime fuel followed by its application in energy storage, becoming the preferred technology by the 2040s. Fig. 4 describes the roadmap of ammonia economy.

2. Overview

The rising focus on developing catalysts for ammonia synthesis is evident from the notable rise in the number of publications in this area over the last two decades (Fig. 5). This clearly indicates the increasing realisation of the immense value that ammonia holds, and hence developing a sustainable mode of production of ammonia is of utmost importance to utilise it as a truly "green fuel" or for various other purposes discussed earlier.

Recently, several review articles have attempted to provide an overview of catalyst development for ammonia synthesis across different modes of production. Tian *et al.* delved into the advancements in thermal catalysts for ammonia synthesis, categorising them based on their constituent elements to discuss notable works in each category.[45] In another review article, Tian *et al.* provided a comprehensive understanding of different modes of ammonia production, including photocatalytic and chemical looping methods.[46] Gharahshiran *et al.* provided an in-depth review of the reactor and catalyst development for NTP-assisted ammonia synthesis.[47] Mu *et al.* in their review article discussed important theories behind catalyst design and the underlying reaction mechanisms to address the existing challenges in electrochemical ammonia synthesis.[48] Long *et al.* particularly focused on the evolution of single-atom catalysts for electrochemical nitrate reduction reaction in their detailed work.[49]

In this review article, we particularly focus on thermal catalysts for low-temperature ammonia synthesis, while also discussing the progress in catalysts for NTP-assisted and electrochemical ammonia synthesis, as we believe they are highly likely to shape the future of ammonia production. Our aim is to provide the reader with a concise summary of recent research pertaining to low-temperature ammonia synthesis. A key aspect of this work is the extensive summary of catalysts for each category, and the holistic review of the dominant modes of ammonia production.

We begin with thermal catalysts, broadly categorised in this work as nitrides, hydrides, intermetallic compounds, electrides and oxides. Under each category, the catalysts are further grouped based on similarities in their composition or structure. We then proceed to discuss the catalyst developments in NTP-assisted ammonia synthesis, specifically for dielectric barrier discharge (DBD) as it is the most commonly used reactor configuration. Progress in electrocatalysts for ammonia synthesis is then discussed separately for the nitrogen reduction reaction and nitrate reduction reaction. We conclude by providing our perspective for the rational catalyst design for future research and offer insights into the outlook of green ammonia synthesis.

3. Thermal catalysts

3.1 Nitride and oxy-nitride-based catalysts

Nitride catalysts are highly efficient for ammonia synthesis, offering excellent catalytic activity and stability under reaction conditions. The presence of nitrogen vacancies facilitates the associative pathway, enabling the activation of stable N_2 bond under mild conditions. Additionally, nitride catalysts are prone

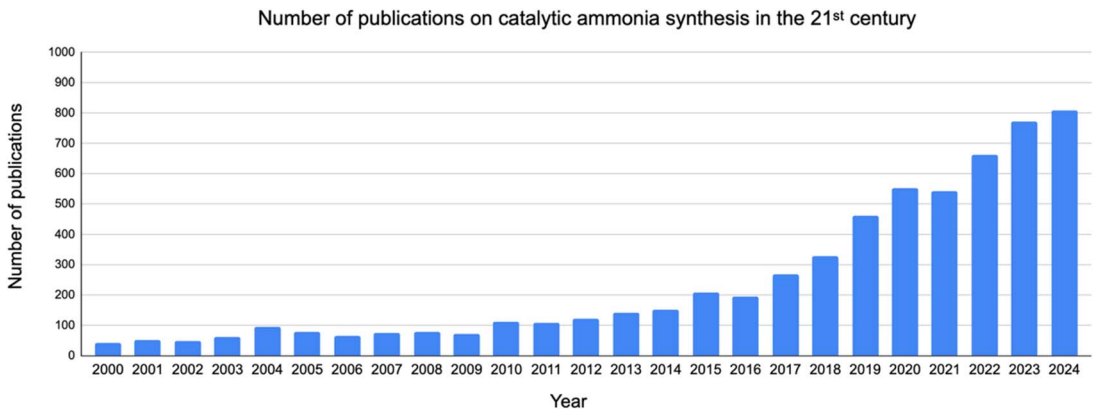

Fig. 5 Plot showing the number of publications per year for articles pertaining to ammonia synthesis.

to oxidation, leading to the formation of oxynitrides during the reaction. Interestingly, this transformation often enhances catalytic activity, as oxynitrides possess a lower work function that promotes efficient N_2 dissociation. Another key factor contributing to the high activity of nitride catalysts is the operation of the Mars-van Krevelen mechanism, wherein lattice nitrogen participates in the reaction as an active species, creating a dynamic cycle of nitrogen replenishment that significantly boosts catalytic performance.

Till date, both binary nitrides (based on cerium,[50] uranium,[51] vanadium,[52] molybdenum,[53] and rhenium[54]) and ternary nitrides (based on Co–Mo, Ni–Mo, and Fe–Mo[55–58]) have been extensively examined and the basis of their design can be understood from the volcano-type plot generated from the turn over frequency (TOF) of various ammonia synthesis catalysts, calculated using density functional theory (DFT). Jacobsen *et al.*[59] calculated the TOF of these catalysts through a combination of a microkinetic model for ammonia synthesis and the linear relation between the nitrogen dissociation potential energy and activation energy. The obtained volcano plot of the TOF of various elements against the nitrogen adsorption energy is shown in Fig. 6.

Fig. 6 exhibits a characteristic volcano-shaped profile, indicating the presence of an optimal nitrogen adsorption energy. This behaviour can be explained through DFT calculations conducted by Jacobsen *et al.*, which demonstrate a linear relationship between the activation energy for nitrogen dissociation and the binding energy of atomic nitrogen across various transition metal surfaces, like the Brønsted–Evans–Polanyi (BEP) relation.[60] Accordingly, the curve identifies two distinct pathways to achieve high catalytic activity: (1) reducing the activation barrier for nitrogen dissociation, which necessitates strong metal–N interactions, or (2) minimizing the surface coverage of adsorbed atomic nitrogen during NH_3 synthesis, which requires weaker metal–N interactions. For instance, the combination of molybdenum (Mo) and cobalt (Co), forming the CoMo system, has demonstrated optimal catalytic activity for ammonia synthesis. Molybdenum exhibits strong nitrogen adsorption, facilitating efficient N_2 dissociation. However, this strong adsorption makes the desorption of nitrogen species from the surface a challenge. In contrast, cobalt, with its weaker nitrogen adsorption, promotes easier desorption. The synergy between these two metals results in an optimal nitrogen adsorption energy, significantly enhancing ammonia synthesis activity compared to the performance of each metal individually. This principle has guided the design of various material combinations for ammonia synthesis reactions.

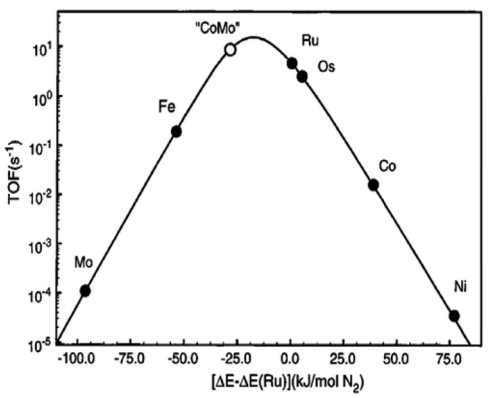

Fig. 6 Calculated TOF (s^{-1}) for ammonia synthesis with variation in nitrogen adsorption energy (400 °C, 5.0 MPa). Adapted with permission from ref. 59. Copyright 2001, the American Chemical Society.

The synthesis of nitride-, nitride-hydride- and oxynitride-based catalysts involves a wide range of methods to achieve specific structural and chemical properties, which enhance the rate of ammonia synthesis. For instance, Ca_3CrN_3 (ref. 61) was synthesized by a topochemical method, which involves chemical transformation of a solid while preserving the key structural motifs of the parent material. Synthesis using this method allows precise control over the arrangement of atoms in the lattice. In this method, Ca_3CrN_3 orthorhombic nitride was heated under hydrogen flow at a temperature of 450 °C for 2 h and then thermally treated in a N_2/H_2/Ar mixture at 400 °C for 24 h. This thermal treatment leads to rotational structural transformation to form a hexagonal nitride hydride, h-Ca_3CrN_3H.

Zhang *et al.* observed that Ru/ZrO_2–N[62] prepared by ammonia-treated ZrO_2 (obtained from $ZrCl_4$) exhibited 4 times higher rate than that prepared using zirconium nitrate. Here, ZrO_2–O and ZrO_2–N were synthesized using a $ZrCl_4$ precursor *via* a UiO-66 route. The UiO-66 route forms nitrogen-modified ZrO_2 (ZrO_2–N) post ammonia treatment which enhances Ru dispersion and electron density. This improves N_2 activation and boosts ammonia synthesis efficiency. For the preparation of UiO-66, $ZrCl_4$ and H_2BDC were dissolved in DMF. This solution was sonicated for 30 minutes followed by heating in an oven at 120 °C for 24 h. Sonication improves precursor dispersion, enhances mixing, and promotes uniform nucleation, which improves the catalyst quality. After sonication at 11 000 rpm for 5 minutes, the product was washed with methanol and DMF and finally dried at 90 °C to obtain UiO-66. It was then calcined in an NH_3 atmosphere at a temperature of 600 °C for 3 h to form ZrO_2. The TEM images for Ru/ZrO_2–O and Ru/ZrO_2–N are shown in Fig. 7g–j.

The solid-state reaction method used for the synthesis of $BaTiO_{3-x}H_x$[63] enables high-temperature-driven phase formation and provides better stoichiometric control. This method is used for the synthesis of complex oxides, nitrides, and hydrogen-substituted materials. BaH_2 and TiO_2 were heated at 800 °C for a period of 20 h under hydrogen flow to obtain $BaTiO_{3-x}H_x$. It was then heated at 600 °C for 12 h in a nitrogen atmosphere, where it undergoes hydride substitution to obtain $BaTiO_{3-x}N_y$ oxy-nitride. Fe, Ru, Co and Ni were loaded on the support by mixing their respective metal precursors with the support in an agate mortar in an Ar environment. The mixture was then treated thermally under hydrogen flow at a temperature of 300 °C or 400 °C for 2 h to obtain the catalysts in their final forms. XRD crystallographs for $BaTiO_{3-x}$, $BaTiO_{3-x}H_x$, $BaTiO_{3-x}N_y$, and $BaTiO_{2.88}$ are shown in Fig. 7e.

In another study, ball milling method was used to synthesize Ru/ZrH_2, Ru/ZrN, Ru/ZrO_2, Ru/TiH_2, Ru/TiN, and Ru/TiO_2 (ref.

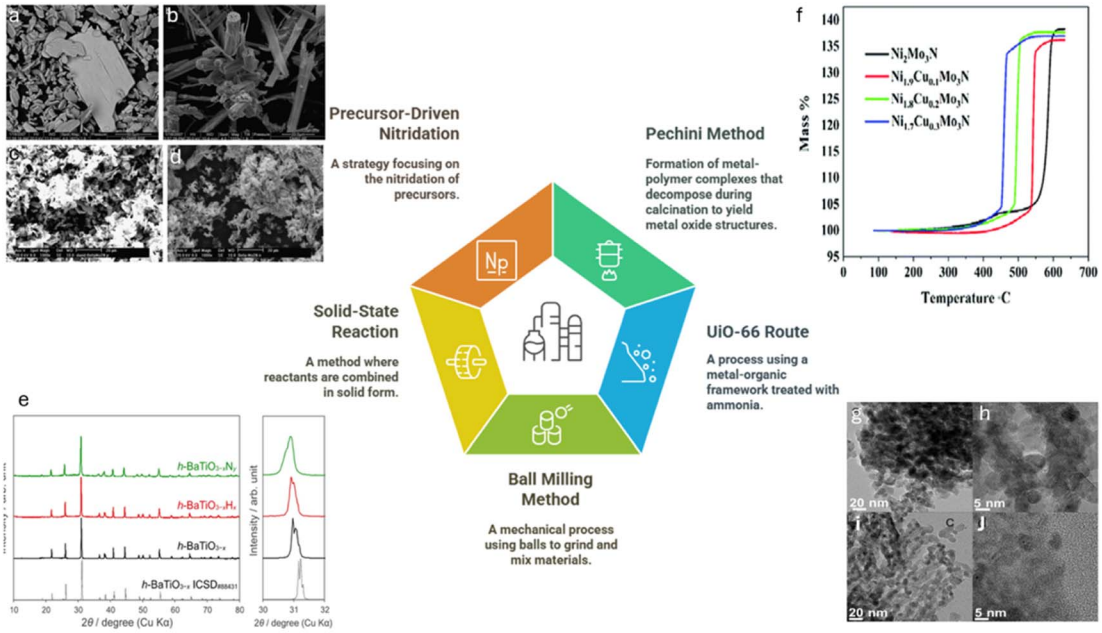

Fig. 7 Various synthesis pathways for nitride and oxy-nitride catalysts. SEM images of (a) γ-Mo_2N derived from MoO_3 powder; (b) nanorods of γ-Mo_2N; (c) β-$Mo_2N_{0.78}$ derived from MoO_3 powder; and (d) β-$Mo_2N_{0.78}$ derived from MoO_3 nanorods prepared *via* a precursor-driven nitridation method. Adapted with permission from ref. 55. Copyright 2007, Elsevier (e) XRD crystallographs of $BaTiO_{3-x}$, $BaTiO_{3-x}H_x$, $BaTiO_{3-x}N_y$, and $BaTiO_{2.88}$ synthesized *via* a solid-state reaction method. Adapted from the work of Miyazaki *et al.*,[63] licensed under CC BY 4.0 (https://creativecommons.org/licenses/by/4.0/). (f) TGA curves showing mass increase% for Ni_2Mo_3N, $Ni_{1.7}Cu_{0.3}Mo_3N$, $Ni_{1.8}Cu_{0.2}Mo_3N$ and $Ni_{1.9}Cu_{0.1}Mo_3N$ catalysts synthesized at 900 °C under ammonia (prepared *via* a citrate gel-assisted ammonolysis method). Adpated from the work of Al Sobhi *et al.*,[64] licensed under CC BY 3.0 (https://creativecommons.org/licenses/by/4.0/). TEM images of (g and h) Ru/ZrO_2–O and (i and j) Ru/ZrO_2–N prepared *via* a UiO-66 route. Adapted with permission from ref. 62. Copyright 2022, Elsevier.

65) catalysts. This method promotes uniform metal dispersion across various supports due to the high-energy impact during milling. ZrH_2 along with ruthenium acetylacetone was taken in an agate jar and then ball milled for a period of 2 h at 300 rpm to obtain Ru/ZrH_2. For the synthesis of K-, Ba- and Cs-promoted Ru/ZrH_2 catalysts, the usual wetness impregnation method was used where nitrate precursors of the respective promoters were dissolved in DI water and then added dropwise to the Ru/ZrH_2 followed by heat treatment at a temperature of 400 °C for 2 h under a 10 vol% H_2/Ar atmosphere.

Precursor-driven nitridation, utilized for synthesizing Co_3Mo_3N, Fe_3Mo_3N, and Ni_2Mo_3N,[55] emphasizes precise precursor preparation followed by high-temperature ammonolysis to form metal nitrides with defined compositions and catalytic properties. This method involves breaking metal–oxygen or metal–halide bonds in the precursor, allowing nitrogen from NH_3 to diffuse and replace oxygen, forming metal–nitrogen bonds. This stabilizes the nitride phase, tuning electronic and catalytic properties. Cobalt molybdate hydrate ($CoMoO_4 \cdot nH_2O$) was prepared by mixing aqueous solutions of Co $(NO)_3 \cdot 6H_2O$ and $(NH_4)_6Mo_7O_{24} \cdot 4H_2O$ at 80 °C followed by vacuum filtration to obtain a purple precipitate. It was then washed with DI water and ethanol and then dried at 150 °C followed by calcination at a temperature of 500 °C. Nitridation of this powder was done in a vertical quartz reactor with 94 mL min^{-1} NH_3 flow. The powder underwent three stages of thermal treatment with the increase in temperature to 357 °C at a ramp rate of 5.6 °C min^{-1} followed by heating to 447 °C at 0.5 °C min^{-1} and finally reaching 785 °C at 2.1 °C min^{-1} with a dwell time of 5 h. The nitrided powder thus obtained was allowed to cool under ammonia flow followed by nitrogen flushing at 100 mL min^{-1} for purging the reactor. Fig. 7a–d shows the SEM images of γ-Mo_2N, nanorods of γ-Mo_2N, β-$Mo_2N_{0.78}$, and β-$Mo_2N_{0.78}$ derived from MoO_3 nanorods.

The Pechini method is used for the synthesis of highly pure metal oxides using citric acid and ethylene glycol to form a gel. This is followed by heat treatment to get the final product. Certain modifications in optimizing precursors, polymerization and nitridation improve the effectiveness of this method. The modified Pechini method used for bimetallic nitride synthesis results in highly pure nitrides such as Ni_2Mo_3N[66] and $CoNiMo_3N$. $NiMoO_4$ oxide precursors were prepared by dissolving $(NH_4)_6Mo_7O_{24} \cdot 4H_2O$ and $M(NO_3)_2 \cdot 6H_2O$ (M = Ni or Co) in aqueous HNO_3 and then in citric acid monohydrate to form a solution. The solution was then evaporated at 70 °C under constant stirring till a light green (Ni–Mo system) or wine-red (Co–Ni–Mo system) gel was obtained. This gel was then calcined in air at 500 °C for a period of 2 h which led to the formation of greyish foams as the final oxide precursor. These oxide precursors were then subjected to ammonolysis in a quartz furnace tube at a temperature of 700 °C under ammonia flow. This method led to the production of high-ceramic yield nitride products.

Table 1 Nitride-, nitride-hydride- and oxynitride-based catalysts (entries from no. 12 onwards have been adapted from the work of Humphreys *et al.*[24])

S. no.	Catalyst	Temp. (°C)	Pressure (MPa)	Rate (mmol g^{-1} h^{-1})	Activation energy (kJ mol^{-1})	Metal %	WHSV	N_2 order	H_2 order	NH_3 order	Surface area (m^2 g^{-1})	Turnover frequency (TOF)	Catalyst synthesis method	Ref.
1	Ca_3CrN_3H	400	5	3.8	75 ± 2	—	66 000	1.13 ± 0.02	2.45 ± 0.29	−0.48 ± 0.07	1	2.1	Topo-chemical method	61
2	Ru/ZrO_2–N	400	1	10.26	—	5.37% Ru	36 000	—	—	—	53	6.1×10^{-3}	Sol–gel, hydrothermal method	62
3	$Fe/BaTiO_{3-x}N_y$	400	0.9	8.3	41.7	1.99% Fe	36 000	0.88	1.51	−1.03	3	—	Solid-state reaction method	63
4	Ru/ZrN	400	1	2.61	108 ± 4	1.95% Ru	60 000	0.48	0.12	−2.63	10	3.8×10^{-3}	Ball milling method	65
5	Ru/N–C	400	1	1.5*	79	1.34% Ru	60 000	0.41	0.95	—	88	2.76×10^{-3}	Solution-based thermal polymerization method	67
6	$Co–N_2$	300	1	2.73	—	3.20% Co	60 000	0.45	0.27	−0.89	230.4	1.41×10^{-3}	Template-assisted nitrogen-doped carbonization method	68
7	$Co–N_3$	300	1	2.23	—	3.24% Co	60 000	—	—	−1.04	221.1	1.09×10^{-3}	Template-assisted nitrogen-doped carbonization method	68
8	$Co–N_4$	300	1	1.42	—	3.66% Co	60 000	—	—	−1.44	191.3	0.76×10^{-3}	Template-assisted nitrogen-doped carbonization method	68
9	γ-Mo_2N	400	0.1	0.034	—	—	9000	—	—	—	—	—	Controlled ammonolysis nitridation method	55
10	β-$Mo_2N_{0.78}$	400	0.1	0.035	—	—	9000	—	—	—	—	—	*In situ* fixed-bed nitridation method	55
11	δ-MoN	400	0.1	0.004	—	—	9000	—	—	—	—	—	Controlled high-temperature ammonolysis nitridation method	55
12	Co_3Mo_3N	400	0.1	0.167	—	—	9000	—	—	—	—	—	Precursor-driven nitridation method	55
13	Co_3Mo_3N	400	0.1	0.652	—	—	9000	—	—	—	—	—	Nitridation method	69
14	Fe_3Mo_3N	400	0.1	0.095	—	—	9000	—	—	—	—	—	Molybdate nitridation method	55
15	Ni_2Mo_3N	400	0.1	0.029	—	—	9000	—	—	—	—	—	Molybdate nitridation method	55
16	Ni_2Mo_3N	400	0.1	0.395	—	—	9000	—	—	—	—	—	Modified Pechini method-	57
17	Co_3Mo_3N Cs promoted	400	0.1	0.869	—	—	9000	—	—	—	—	—	Promoter-enhanced nitridation method	69

Table 1 (*Contd.*)

S. no.	Catalyst	Temp. (°C)	Pressure (MPa)	Rate (mmol g^{-1} h^{-1})	Activation energy (kJ mol^{-1})	Metal %	WHSV	N_2 order	H_2 order	NH_3 order	Surface area (m^2 g^{-1})	Turnover frequency (TOF)	Catalyst synthesis method	Ref.
18	Co_3Mo_3N K promoted	400	0.1	0.986	—	—	9000	—	—	—	—	—	Promoter-enhanced nitridation method	69
19	$NiCoMo_3N$	400	0.1	0.166	—	—	12 000	—	—	—	—	—	Modified Pechini method	66
20	Ni–LaN	400	0.1	5.543	—	—	36 000	—	—	—	—	—	Nitridation method	70
21	$Ni_{1.1}Fe_{0.9}Mo_3N$	500	0.1	0.354	—	—	5200	—	—	—	—	—	Citrate gel-assisted ammonolysis method	64
22	CeN NPs	400	0.9	1.450	—	—	36 000	—	—	—	—	—	Hydride-based nitridation	71
23	$K_2[Mn(NH_2)_4]$	400	1	11.141	—	—	6000	—	—	—	—	—	Mechanochemical ammoniation method	23
24	γ-Mo_2N	400	10	30 (mL g^{-1} h^{-1})	—	—	—	—	—	—	—	—	Controlled ammonolysis method	58
25	Co_3Mo_3N	400	10	120 (mL g^{-1} h^{-1})	—	—	—	—	—	—	—	—	Controlled ammonolysis method	58
26	Fe_3Mo_3N	400	10	90 (mL g^{-1} h^{-1})	—	—	—	—	—	—	—	—	Controlled ammonolysis method	58
27	Ni_2Mo_3N	400	10	80 (mL g^{-1} h^{-1})	—	—	—	—	—	—	—	—	Controlled ammonolysis method	58
29	Co_3Mo_3N (5% Cs)	400	10	1040 (mL g^{-1} h^{-1})	—	—	—	—	—	—	—	—	Controlled ammonolysis method	58
29	Fe_3Mo_3N (5% Cs)	400	10	440 (mL g^{-1} h^{-1})	—	—	—	—	—	—	—	—	Controlled ammonolysis method	58
30	Ni_2Mo_3N (5% Cs)	400	10	530 (mL g^{-1} h^{-1})	—	—	—	—	—	—	—	—	Controlled ammonolysis method	58

In a similar method, citric acid was used as a chelating agent in the citrate gel-assisted high-temperature ammonolysis method, which led to the formation of nanocrystalline metal nitrides such as $Ni_{1.1}Fe_{0.9}Mo_3N$.[64] $(NH_4)_6Mo_7O_{24}\cdot 4H_2O$, along with either $Cu(NO_3)_2\cdot 4H_2O$ or $Fe(NO_3)_2\cdot 6H_2O$, was dissolved in HNO_3, which led to the formation of a green solution. Citric acid monohydrate was added to this solution followed by evaporation at 70 °C to form a gel, which was then thermally treated in an ashing furnace at 500 °C for 2 h. Finally, the furnace tube was purged with N_2 and then passivation of the sample surfaces was done by letting air to diffuse slowly to finally obtain a black crystalline product. Fig. 7f displays the TGA curves showing mass increase% for Ni_2Mo_3N, $Ni_{1.7}Cu_{0.3}Mo_3N$, $Ni_{1.8}Cu_{0.2}Mo_3N$ and $Ni_{1.9}Cu_{0.1}Mo_3N$ catalysts synthesized at 900 °C under ammonia.

Recently, a number of metal nitride phases have been reported, which exhibit excellent catalytic activity for ammonia synthesis under mild conditions. Often, metal nitrides offer high stability, greater catalytic activity, and high yield, comparing traditional metals (Fe, Ru, and Co)-catalysts.

In addition to nitrides, ternary amides of transition and alkali metals have been reported. For instance, Cao *et al.* prepared $Rb_2[Mn(NH_2)_4]$ and $K_2[Mn(NH_2)_4]$ *via* mechanical milling of the respective metals at room temperature under 0.7 MPa of ammonia.[23] These catalysts showed better performance than the best performing ternary nitride (*i.e.*, Co_3Mo_3N). Ammonia synthesis rates of 11 mmol g^{-1} h^{-1} and 6 mmol g^{-1} h^{-1} were observed for $K_2[Mn(NH_2)_4]$ and $Rb_2[Mn(NH_2)_4]$, respectively, at 400 °C and 1.0 MPa. Notably, under similar conditions, the synthesis rate was merely 5.3 mmol g^{-1} h^{-1}over the Co_3Mo_3N catalyst.[58] Therefore, ternary amides could be a better choice than nitrides for use as ammonia synthesis catalysts. The reported catalytic activities for nitride-based catalysts are provided in Table 1.

Because of the low binding energy for N_2, Ni metal has illustrated poor performance towards ammonia synthesis, even if the metal was used with excellent supports such as $C_{12}A_7$:e^- and MgO. Based on the volcano plot (Fig. 6), our group has demonstrated ammonia synthesis reaction using bi-metal catalysts such as Co/Fe, Ru/Fe, and Ni/Fe.[31] All the tested catalysts have shown different trends for nitrogen dissociation and ammonia synthesis activity. In comparison to Ru/Fe and Co/Fe, the catalytic activity of Ni/Fe was very poor even under high-temperature reaction conditions, which is in line with the Jacobsen volcano plot for transition metals.[59] Ru/Fe and Co/Fe catalysts have shown NH_x formation as the rate-determining step while for Ni/Fe, the rate-determining step was N_2 dissociation. This observation clearly indicates that both Ru/Fe and Co/Fe catalysts can efficiently break N_2 molecules, whereas the Ni/Fe catalyst has difficulty to break it. On the contrary, Ye *et al.*

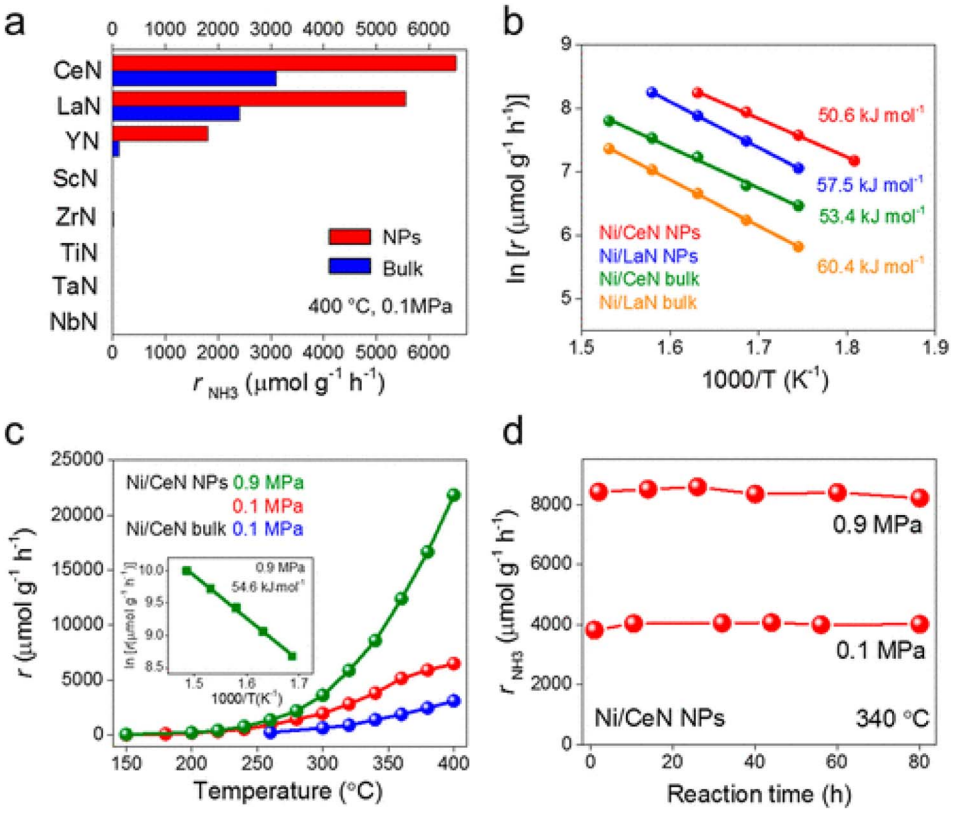

Fig. 8 (a) Catalytic performance of Ni-loaded nitride catalysts at 400°Cand 0.1 MPa (b) Arrhenius plots of Ni/CeN, Ni/LaN bulk and nanoparticles (NPs) at 0.1 MPa. (c) Temperature-dependence of ammonia synthesis activity over NPs and bulk particles of Ni/CeN at 0.1 and 0.9 MPa (d) time course of ammonia synthesis over Ni/CeN NPs at 340 °C and different pressures (0.1 and 0.9 MPa). Other reaction conditions: 0.1 g catalyst, N_2 : H_2 = 15 : 45 mL min^{-1}, 150–400 °C. Adapted with permission from ref. 71. Copyright 2020, the American Chemical Society.

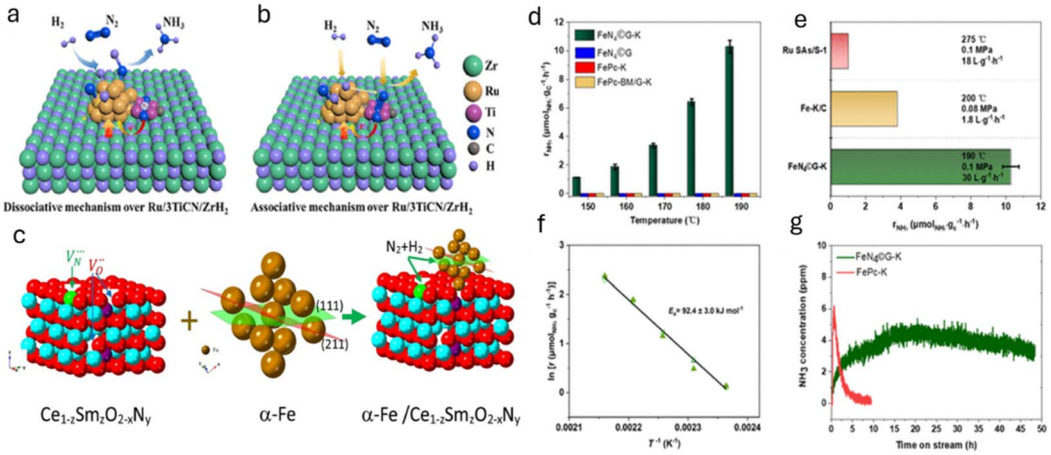

Fig. 9 (a) Dissociative and (b) associative mechanisms of NH_3 synthesis on Ru/3TiCN/ZrH_2. Atoms are coloured as follows: Ru (gold), Zr (green), Ti (purple), N (dark blue), C (grey), and H (light blue). Adapted with permission from ref. 72. Copyright 2022, the American Chemical Society. (c) Illustration showing the interaction of anion vacancies with α-Fe particles and reactants H_2 and N_2. The (111) plane in α-Fe is shown in green, and the (211) plane in red. Adapted with permission from ref. 73. Copyright 2021, Elsevier. (d) Ammonia production rates for FeN_4©G-K, FeN_4©G, FePc-K, and FePc-BM/G-K at different temperatures at 0.1 MPa. (e) Comparison of FeN_4©G-K ammonia production rate with Fe-K/C and Ru SAs/S-1 under similar conditions. (f) Arrhenius plot showing the ammonia synthesis activity of FeN_4©G-K from 150 to 190 °C at 0.1 MPa. (g) Stability test of FeN_4©G-K *versus* FePc-K at 170 °C and 0.1 MPa. Reaction conditions: $N_2/H_2 = 1/3$, WHSV = 30 L g_{cat}^{-1} h^{-1}, unless otherwise noted. Adapted with permission from ref. 74. Copyright 2023, the American Chemical Society.

synthesized a Ni–LaN catalyst and found an excellent rate of 5.543 mmol g^{-1} h^{-1} at 400 °C and 0.1 MPa.[70] In this exemplary work, surface nitrogen vacancies present in the LaN catalyst facilitate the weakening of the N triple bond and the hydrogen dissociation over the Ni surface. In a similar work by the same group, Ni–CeN was used as a novel catalyst and displayed an activity of 6.5 mmol g^{-1} h^{-1} at 400 °C and 0.9 MPa.[71] Under these conditions, the effluent NH_3 concentration was equal to the thermodynamic equilibrium value (% effluent concentration NH_3 = 0.45 vol%). In addition to CeN, other nitrides such as YN and LaN were investigated. The catalytic performance and reaction kinetics of all the catalysts used in this work are summarised in Fig. 8.

In this work, ammonia was produced from the reaction between lattice N in the CeN (validated by *in situ* experiment with $^{15}N_2$ and H_2 using the CeN catalyst) and adsorbed hydrogen. Hence, nitrogen vacancy containing nitride can activate the stable N_2 bond easily under low-temperature and low-pressure reaction conditions. Such works successfully demonstrate the possible application of Ni for ammonia synthesis, as more expensive Ru catalysts have.

In an interesting article by Zhou *et al.*, both associative and dissociative routes were utilized for enhancing the catalytic activity of Ru for the generation of ammonia under mild conditions.[72] In particular, the authors ball milled desired amounts of ZrH_2, TiCN, and ruthenium acetylacetone to synthesize TiCN-promoted Ru/ZrH_2. The as-developed catalyst demonstrates a rate of 25.6 mmol g^{-1} h^{-1} at 400 °C and 1.0 MPa. This study disclosed that TiCN donates electrons to Ru clusters, which not only readily dissociate the N_2 bond *via* the dissociative mechanism but also prohibit Ru NPs from sintering. Additionally, the nitrogen vacancies on TiCN favor the N_2 hydrogenation to NNH *via* the associative pathway. Both the associative and dissociative pathways are depicted in Fig. 9a and b.

Since nitrides offer excellent properties as ammonia synthesis catalysts, the stability of these nitrides has to be evaluated in the presence of oxygenates such as O_2, CO, and H_2O at high temperatures. As is known, at high temperatures, nitrides are prone to oxidation and can transform to oxynitrides or oxides in the presence of oxygenates.[75] Recently, Prof. Hosono and his group have remarkably enhanced the performance of Ru by using barium oxynitride as a promoter. In this work, an electride (BaO_xN_y:e_z^-) was used, which increased the ammonia synthesis activity by 40–100 times, comparing the conventional BaO promoter at 400 °C and 0.1 MPa.[23] Under this condition, the ammonia formation rate of Ru supported with BaO_xN_y was 2.05 mmol g^{-1} h^{-1}.

To assess the high catalytic activity for the production of ammonia, barium oxynitride was generated by the solid-state reaction of Ba_2N and BaO. Specifically, a mixture consisting of a definite molar ratio of Ba_2N and BaO was sealed in Ar-filled stainless-steel tubes and were heated at 750 °C for 24 h. This results in the formation of dark-brown BaO_xN_y, and Ru nanoparticles (precursor: triruthenium dodecacarbonyl, $Ru_3(CO)_{12}$, 99%, Sigma-Aldrich) were loaded onto this support *via* a chemical vapor deposition method. It is reported that the inclusion of N^{3-} into the O^{2-} site of BaO_xN_y:e_z^- led to an increase in the concentration of low-work-function electrons in the lattice sites, which strengthen the electron donating ability of the BaO_xN_y:-e_z^- catalyst.

In the same line, Humphreys *et al.* reported the use of oxynitrides as promoters for the low-cost Fe catalyst for ammonia synthesis.[73] The authors introduced a large amount of anion vacancies in CeO_2 by incorporating cations (Sm^{3+} ions) and anions (N^{3-} ions), which significantly increased the nitrogen

vacancies. In particular, 80 wt% Fe-20 wt% $Ce_{1-z}Sm_zO_{2-x}N_y$ ($z \leq 0.5$) was synthesized using a facile one-step combustion synthesis method and has demonstrated the highest ammonia synthesis rate of 18.8 mmol g^{-1} h^{-1} at a temperature of 400 °C and a pressure of 3.0 MPa. It is deduced that, during the reaction and high concentration of hydrogen, the cerium oxynitride could resemble $BaCeO_{3-x}N_yH_z$, suggesting the formation of hydride intermediates. The apparent activation energy of the as-prepared catalyst with $z \geq 0.3$ was 45 kJ mol^{-1}, the lowest activation energy for all reported ammonia synthesis catalysts. It is believed that the higher catalytic activity is directly related to the larger lattice volume of the support that allows large mobility of the N^{3-}/H^- ions. Here, the reaction proceeds through the Mars-van Krevelen mechanism mediated by the anion vacancies. The high concentration of anion vacancies in $Ce_{1-z}Sm_zO_{2-x}N_y$ will facilitate the nesting/anchoring of Fe particles, resulting in strong metal support interaction (SMSI). This SMSI can prohibit the sintering of Fe particles even under a strong oxidising environment. Therefore, a large amount of anion vacancies in cation-doped cerium oxynitride improved both the stability and catalytic activity for ammonia synthesis. High N^{3-} ion conductivity can expand the ammonia synthesis reaction zone by allowing N^{3-} ions to form anywhere on the surface and quickly move through oxynitride particles to active sites. These sites, where α-Fe contacts $Ce_{1-z}Sm_zO_{2-x}N_y$, complete the reaction, boosting the catalytic activity. This is depicted in Fig. 9c.

The development of heterogeneous catalysts by replicating the nitrogenase structure has attracted wide attention, as it can enable nitrogen fixation under mild conditions. Hence, nanomaterials with enzyme-like characteristics have been recently used for ammonia production. For instance, Zhang *et al.* performed hydrogenation of a thiolate-bridged $Fe^{IV}Fe^{IV}$μ-nitrido complex at 2.0 MPa and room temperature to generate ammonia.[76] Similarly, Chen *et al.* reported the catalytic performance of an iron-single-site catalyst (FeN_4©G-K) confined within the graphene matrix, synthesized by milling iron phthalocyanine with graphene for 2 h at 450 rpm in ethanol and promoted by alkali metals such as K.[74] Herein, an activity of 1.1μmol g^{-1} h^{-1} at 150 °C and 10.3 μmol g^{-1} h^{-1} at 190 °C was observed using the as-prepared catalyst. The reaction intermediates such as $N_2H_2^*$ and $N_2H_3^*$ were identified by TOF-MS, which clearly indicates that ammonia synthesis process follows an associative hydrogenation mechanism. Moreover, this study also finds that alkali metal, K, significantly reduces the hydrogenation barriers of N_2^* and, therefore, accelerates the reaction rate.

The catalytic performance of FeN_4©G-K for ammonia synthesis was analyzed with a gas mixture of 25% N_2–75% H_2 at a weight hourly space velocity (WHSV) of 30 L g_{cat}^{-1} h^{-1}. The results show FeN_4©G-K to be active at atmospheric pressure in the temperature range of 150–190 °C, with the NH_3 formation rate increasing from 1.1 μmol NH_3 g_c^{-1} h^{-1} at 150 °C to 10.3 μmol NH_3 g_{cat}^{-1} h^{-1} at 190 °C. This contrasts sharply with FePc-K and FePc-BM/G-K, which showed no activity despite possessing FeN_4 sites and K promotion. This difference highlights the importance of the FeN_4 sites embedded in a graphene lattice

Table 2 Metal hydride catalysts

S. no.	Catalyst	Temp. (°C)	Pressure (MPa)	Rate (mmol g^{-1} h^{-1})	Activation energy (kJ mol^{-1})	Metal%	WHSV	N_2 order	H_2 order	NH_3 order	Surface area (m^2 g^{-1})	Turnover frequency (TOF)	Catalyst synthesis method	Ref.
1	$1Ru/ZrH_2$	400	0.1	0.056	72.5	1% Ru	—	0.79	0.74	−0.65	—	—	Dispersion and deposition method	77
2	$7Ru/ZrH_2$	400	0.1	0.574	70.3	7% Ru	—	1.63	0.98	−1.70	0.51	—	Dispersion and deposition method	77
3	$7Ru–0.2K/ZrH_2$	400	0.1	0.698	64.5	7% Ru	—	0.75	0.31	−0.26	—	—	Dispersion and deposition method	77
4	Ru/ZrH_2	400	1	8.98	70 ± 1	1.93% Ru	60 000	0.51	0.04	−1.50	4	13.1×10^{-3}	Ball milling method	65
5	Ru/ZrH_2	400	1	11.6	97	1.70% Ru	60 000	—	—	—	2.0	0.019	Ball milling method	72
6	$VH_{0.39}$	400	5	3.2	118 ± 6	—	66 000	0.39 ± 0.04	1.04 ± 0.06	−1.2 ± 0.2	—	—	Ball milling method	78

and the role of K in promoting the reaction. Compared with previous catalysts, FeN_4©G-K demonstrates superior performance; its NH_3 formation rate at 0.1 MPa and 190 °C is about 2.5 times higher than that of Fe–K/C and significantly outperforms Ru SAs/S-1. This improvement is attributed to the unique structure of FeN_4©G-K and its higher Fe loading. Additionally, the catalyst exhibits a relatively low activation energy (92.4 kJ mol^{-1}), indicating efficient N_2 dissociation. Stability tests reveal FeN_4©G-K to remain active over 48 hours at 170 °C and 0.1 MPa, while FePc-K quickly deactivates, likely due to hydrogenation of FeN_4 sites. This distinction underscores the stability and effectiveness of FeN_4©G-K, making it a promising catalyst for ammonia synthesis (Fig. 9d–g).

Nitride catalysts therefore present several benefits such as the operation of the Mars-van Krevelen mechanism and the ability to form oxynitride phases, which play a pivotal role in enhancing the ammonia synthesis rate. To fully exploit these advantages, future efforts could focus on controlling oxynitride formation and optimizing nitrogen vacancy concentrations, thereby maximizing the synergy between these mechanisms and further enhancing catalyst efficiency for ammonia synthesis.

3.2 Hydride-based catalysts

As discussed earlier, the dissociation of strong nitrogen bonds is one of the difficult steps for the ammonia synthesis, and conventional catalysts produce ammonia through a relatively energy-expensive pathway. Recently, hydrides have emerged as potential candidates to break nitrogen bonds under mild conditions, and found to dissociate nitrogen bonds in two ways: (i) by reacting hydrogen with an adsorbed N-atom from the transition metal to form ammonia, (ii) by splitting hydrogen into electrons and protons; where, electrons transfer to the antibonding π-orbital of nitrogen molecules and readily break the nitrogen bonds (see Tables 2–4 for detailed summary of hydride-based catalysts).

The unique ability of these catalysts to exhibit exceptional ammonia synthesis activity under low-temperature conditions, where the rate-determining step shifts from N_2 dissociation to NH_x formation, makes them highly promising for efficient ammonia production.

The process of synthesizing hydride-based catalysts for ammonia synthesis entails the preparation of metal hydrides that facilitate catalytic activity through rapid hydrogen release. Generally, preparation of these catalysts is carried out by reducing metals in hydrogen-rich atmospheres. Through careful engineering, the preparation has been optimized to favor metal dispersion for hydrogen storage and electronic characteristics of the catalyst. Because of their high reactivity, hydride-based catalysts can make efficient use of hydrogen in ammonia synthesis, thus posing an important avenue for improving catalytic processes in ammonia production.

Vacuum-assisted metal deposition has been employed in Ru-based catalyst deposition on $TiMn_2$, ZrH_2,[77] MgO, and carbon substrates. Here Ru atoms diffuse on the substrate surface and then transit to stable sites. This is followed by their nucleation into clusters and then adhesion *via* chemical bonding, van der Waals forces or mechanical interlocking, which ensures better dispersion and strong attachment. $TiMn_2$ and ZrH_2 powders were prepared by hand milling in an alumina mortar and pestle. Ruthenium(III) acetylacetonate ($Ru(acac)_3$) along with $TiMn_2$ and ZrH_2 powder, was dispersed in tetrahydrofuran (THF) and then the resulting solution was evaporated at a high temperature with constant stirring under vacuum. In this technique, evaporation under vacuum pressure ensures that the metal loading and dispersion are completely uniform. This is particularly beneficial in hydrogenation reactions because it allows modulation in the electron-donating and hydrogen-storing abilities, which, in turn, helps to boost the activity of the catalyst.

Ball-milling synthesis is another more widely used method applied for Ru/ZrH_2,[72] Ru/ZrN, Ru/ZrO_2, Ru/TiH_2, Ru/TiN, and Ru/TiO_2 as catalysts. Here, high-energy mechanical impacts ensure uniform distribution of metals with the stability and reactivity of the catalyst. By impregnating with alkali metal promoters K, Ba, and Cs, the catalytic properties are subsequently modified by changing electronic interactions and adsorption energies in Ru/ZrH_2 systems. ZrO_2 was prepared by dissolving a $Zr(NO_3)_2$ precursor in DI water followed by the addition of a NaOH solution to tune the pH to 9.5. After continuing the stirring for 1 h, the resulting sediment was washed with DI water till the pH turned 7. Thereafter, it was dried at 60 °C for a period of 12 h and lastly calcined at 550 °C for 4 h to form a ZrO_2 support. Ruthenium was then added to these supports by a ball-milling method in which support (ZrH_2/ZrO_2) along with ruthenium acetylacetone was taken in an agate jar and ball-milled at 300 rpm for a 2 h period. For the synthesis of promoted Ru/ZrH_2 catalyst, nitrate precursors of K, Ba and Cs were dissolved in DI water and then this solution was added dropwise to the ZrH_2 support followed by drying using an infrared lamp. At last, these powders were treated thermally at a temperature of 400 °C for 2 h in a 10 vol% H_2/Ar atmosphere to obtain the promoted Ru/ZrH_2 catalysts.

Similarly, several routes for the synthesis of metal hydride catalysts with oxide support catalysts are developed for specific properties of the material. Examples include calcination of the ball-milled mixture of LiH (or LiD) or BaH_2 with Ru powder in H_2 (or D_2) at elevated temperatures and pressures to give Li_4RuH_6 and Ba_2RuH_6 (ref. 79) samples. Ball milling ensures fine mixing, and calcination at high temperatures promotes the diffusion of hydrogen for the formation of desired hydrides through solid-state reactions. For this, hydrides of Li, Na, K, Ba and Ca were milled with Ru powder at a high temperature (700 °C) and pressure (50 bar). However, under these conditions, only partial synthesis of Na_4RuH_6 and K_3RuH_7 is possible and some amount of NaH/KH and Ru remain unreacted.

In another method of preparation of Li_4RuH_6/MgO catalysts, reduced Ru/MgO was impregnated in a lithium–ammonia solution (Li : Ru ≈ 4 : 1), followed by hydrogenation at 300 °C to form Li_4RuH_6. In this method, ammonia stabilizes metal ions ensuring uniform precursor distribution, while metallic Li or Ba reacts with ammonia to form metal amides. Subsequent hydrogenation at 300 °C facilitates the conversion of these

Table 3 Metal hydride catalysts with oxide supports

S. no.	Catalyst	Temp. (°C)	Pressure (MPa)	Rate (mmol g^{-1} h^{-1})	Activation energy (kJ mol^{-1})	Metal%	WHSV	N_2 order	H_2 order	NH_3 order	Surface area (m^2 g^{-1})	Turnover frequency (TOF)	Catalyst synthesis method	Ref.
1	Ca_2RuH_6/MgO	300	0.1	8.6	75.4 ± 2.4	9%	60 000	0.94	0.26	−0.57	—	8.0×10^{-3}	Ball milling-calcination method	79
2	Na_4RuH_6/MgO	300	0.1	8.3	118.8 ± 1.7	7.6%	60 000	0.92	−0.32	−0.29	—	7.9×10^{-3}	Ball milling-calcination method	79
3	K_3RuH_7/MgO	300	0.1	15.7	139.7 ± 6.8	8.2%	60 000	1.17	−0.53	−0.36	—	13.7×10^{-3}	Ball milling-calcination method	79
4	Li_4RuH_6/MgO	300	0.1	9.1	71.2	8.0%	60 000	0.91	0.30	−0.59	—	8.6×10^{-3}	Ball milling-calcination method	79
5	Ba_2RuH_6/MgO	300	0.1	13.8	63.9	5.0%	60 000	0.92	1.00	−0.63	—	24.2×10^{-3}	Ball milling-calcination method	79
6	Li_4RuH_6/MgO	225	0.1	—	102.8 ± 3.3	8% Ru	60 000	0.82 ± 0.02	−0.47 ± 0.01	−0.18 ± 0.02	—		Ball milling-calcination method	79
7	Li_4RuH_6/MgO	300	0.1	—	71.2 ± 1.5	8% Ru	60 000	0.91 ± 0.03	0.30 ± 0.03	−0.59 ± 0.01	—	6×10^{-3}	Ball milling-calcination method	79
8	LiH/Co–Mg–O	300	1	19	55.8 ± 2.2	21.3% (Co), 17.2% (Li)	60 000	0.76 ± 0.06	1.19 ± 0.06	0.52 ± 0.02	96	—	Ball milling method	79
9	LiH–Ir/MgO	400	1	0.99	53.4 ± 2.6	12.9% Ir	60 000	1.27 ± 0.06	−0.36 ± 0.02	−0.65 ± 0.02	—	—	Ball milling method	80
10	Ba_2RuH_6/MgO	200	0.1	0.5	90.3 ± 2.1	5% Ru	60 000	0.92 ± 0.01	−0.49 ± 0.02	−0.39 ± 0.01	—	1×10^{-3}	Impregnation–reduction method	81
11	Ba_2RuH_6/MgO	300	0.1	12.6	63.9 ± 4.5	5% Ru	60 000	0.83 ± 0.03	1.00 ± 0.01	−0.63 ± 0.02	—	0.017	Impregnation–reduction method	81

Table 4 Catalysts with oxyhydride/oxide + hydride supports

S. no.	Catalyst	Temp. (°C)	Pressure (MPa)	Rate (mmol g^{-1} h^{-1})	Activation energy (kJ mol^{-1})	Metal%	WHSV	N_2 order	H_2 order	NH_3 order	Surface area (m^2 g^{-1})	Turnover frequency (TOF)	Catalyst synthesis method	Ref.
1	BaH_2–BaO/Fe/CaH_2	300	0.9	5.5	40 ± 5	—	36 000	1.0	1.5	−1.1	7	12.2	Impregnation–reduction method	26
2	Ru/BaH_2–BaO	300	0.9	16.5	79 ± 5	10%	36 000	1.4	−1.6	−1.7	20	3.5×10^{-3}	Impregnation–reduction method	26
3	BaH_2/Ni–MgO	300	1	1.76	87 ± 6	20.5% (Ni)	60 000	0.79 ± 0.04	−0.98 ± 0.09	0.83 ± 0.03	45.3	—	Co-precipitation–impregnation method	82
4	Ru/$Ba(OH)_2$–TiH_2 (10% $Ba(OH)_2$)	400	0.1	3.05	—	1% Ru	24 000	0.79	0.15	−0.36	1.65–1.91	6×10^{-2}	Wetness impregnation method	83
5	Fe/$BaTiO_{3-x}H_x$	400	0.9	4.8	42.3	1.83% Fe	36 000	—	—	—	2.6	—	Solid-state reaction method	63
6	BaH_2–BaO/Fe	300	0.9	5.5	40	—	36 000	0.77	0.47	−1.13	7	12.2	Impregnation–reduction method	84
7	Ru/BaO–BaH_2	300	0.9	16.5	69	10% Ru	36 000	0.70	−0.79	−1.65	20	3.5×10^{-3}	Reduction–deposition method	84

intermediates into hydride compounds (Li_4RuH_6 or Ba_2RuH_6) on the MgO support. The Ba_2RuH_6/MgO[81] catalyst was prepared similarly by an ammonia-mediated impregnation method. Using ammonia helps in stabilizing metal ions and controls precursor distribution. A barium–ammonia solution (molar ratio: Ba/Ru = 4/1) was used for the impregnation of Ru/MgO, where metallic Ba was converted into barium amide ($Ba(NH_2)_2$) in the presence of Ru. Then excess of ammonia was removed followed by hydrogenation at a temperature of 300 °C, which led to the formation of Ba_2RuH_6 on MgO. Fig. 10 shows the rate of ammonia synthesis for Ca_2RuH_6-based catalysts at 300 °C and apparent activation along with STEM and elemental mapping images of the Ca_2RuH_6/MgO hydride catalyst. It also shows the FT-IR spectra of $Ca_2Ru(H/D)_6$, $Ca_2Ru(H/D)_6$/MgO, and post-reaction $Ca_2Ru(H/D)_6$/MgO catalysts (reaction conditions: $N_2/(H_2/D_2) = 1:3$, 20 bar, 400 °C).

A LiH–Ir[80] composite was synthesized by a ball milling method by reacting $IrCl_3$ with LiH at a molar ratio of 18/1, followed by ball-milling at 200 rpm for 3 h, and washing with THF to remove LiCl, resulting in a composite with a molar ratio of 15/1. The BaO–Ru/MgO catalyst was prepared by impregnating $Ba(NO_3)_2$ on Ru/MgO, followed by reduction at 400 °C. All these methods guarantee controlled incorporation of Ba and dispersion of Ru with great significance regarding catalytic activity.

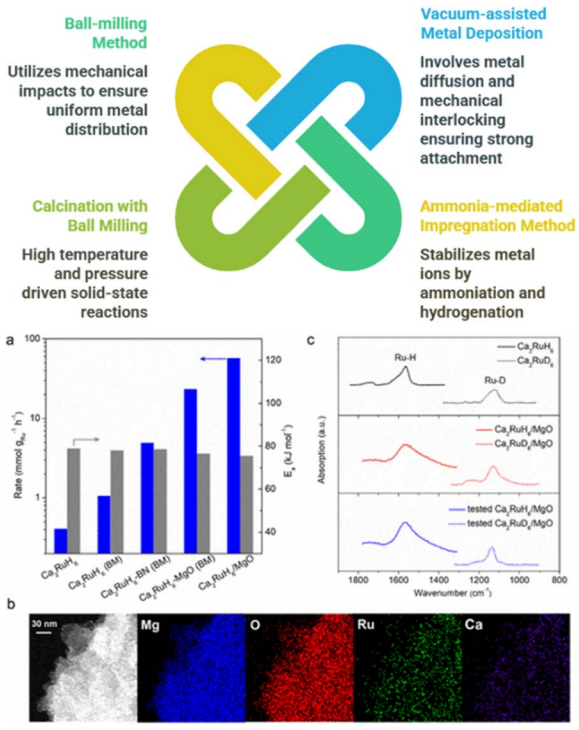

Fig. 10 Various synthesis pathways for hydride and oxy-hydride catalysts. (a) Rate of ammonia synthesis for Ca_2RuH_6-based catalysts prepared *via* an ammonia-mediated impregnation method and corresponding activation energies. (b) STEM and elemental mapping images of the Ca_2RuH_6/MgO hydride catalyst. (c) FT-IR spectra of $Ca_2Ru(H/D)_6$, $Ca_2Ru(H/D)_6$/MgO, and post-reaction $Ca_2Ru(H/D)_6$/MgO catalysts (reaction conditions: $N_2/(H_2/D_2) = 1:3$, 20 bar, 400 °C). Adapted with permission from ref. 81. Copyright 2022, the American Chemical Society.

BaH_2–BaO/Fe/CaH_2 (ref. 26)-based oxyhydride was formed using the impregnation–reduction method for uniform depositions of transition metal nanoparticles on the BaH_2–BaO phase. The reduction step is essential to convert precursors into active metal nanoparticles. Fe $(NO_3)_3 \cdot 9H_2O$ was dissolved in DI water followed by evaporation at 70 °C. The resulting red solid was heated at a temperature of 300 °C for a period of 10 h to obtain α-Fe_2O_3. BaH_2–BaO/Fe/CaH_2 was prepared by dissolving α-Fe_2O_3 and Ba $(NO_3)_2$ in DI water followed by evaporation. Ba $(NO_3)_2$-impregnated α-Fe_2O_3 thus formed was heated to 300 °C for a 10 h period in air. At last, it was mixed with CaH_2 in an alumina mortar to obtain the final catalyst.

In co-precipitation of Ni–Mg–O[83] solid solutions, Ni and Mg precursors with oxalic acid were mixed homogeneously followed by controlled aging and filtration, drying, and reduction in hydrogen, facilitating uniform metal dispersion and catalytic stabilization. Oxalic acid and magnesium acetate were dissolved in DI water to prepare their solutions. The magnesium acetate solution was then added dropwise to the oxalic acid solution and allowed to age at 30 °C for 10 h. The solid thus obtained was dried for 10 h at a temperature of 100 °C. Finally, it was reduced at 420 °C for 5 h in a hydrogen atmosphere in a Ni–Mg–O solid solution.

In the case of BaH_2/Ni–Mg–O,[82] BaH_2 was dispersed well on the Ni–Mg–O support through modification of Ba ammonium solution, and this was followed by hydrogenation under high-temperature and -pressure conditions, which further optimized catalytic activity in the second step. In another work, $BaTiO_{3-x}N_y$[63] was prepared by a solid-state reaction method, which involved high-temperature hydrogen treatment (800 °C), hydride substitution at 600 °C, and oxidation at 900 °C essential to get the desired composition of oxyhydride.

Catalytic materials frequently involve some transition metals, which have strong nitrogen dissociation energy. This implies that transition metals can easily break the nitrogen molecules but have challenges in desorbing them from the surface. Hence, most of the active sites are unavailable for the subsequent nitrogen activation, which severely impedes the ammonia formation rate. To address this issue, Wang *et al.* have recently provided a potential solution to the long-standing scaling relationship between the apparent activation energy and the nitrogen binding energy.[85]

They mixed LiH to early and late 3d transition metals (TM) such as Mn, Fe, Co, V, Cr and Ni to offer another catalytic site for nitrogen molecules. In particular, negatively charged hydrogen atoms of LiH reduces activated nitrogen atoms from the transition metal or its nitride, and combines with nitrogen atoms to synthesize lithium amide. Subsequently, the lithium amide splits into H_2 to release NH_3 and regenerates LiH. The following are the reactions involved:

$$N_2 + 2^* \rightarrow 2N^* \quad (14)$$

$$N^* + LiH \rightarrow {}^* + [LiNH] \quad (15)$$

$$[LiNH] + H_2 \rightarrow LiH + NH_3 \quad (16)$$

Moreover, at a lower temperature, the rate-determining step shifts from nitrogen dissociation to the hydrogenation of surface-adsorbed nitrogen atoms. At 300 °C and under 1.0 MPa, the activities were at least four (Cr–, Mn– and Co–LiH), three (V–LiH), two (Ni–LiH), and one (Fe–LiH) orders of magnitude greater than that of the pristine TM. The reported activity for Fe–LiH and Co–LiH were *ca.* 11 mmol g^{-1} h^{-1}, at 350 °C and 1.0 MPa pressure. Importantly, the apparent activation energies for these selected catalysts were close to 50–60 kJ mol^{-1}. In the same line, Yan *et al.* synthesized MgO-supported LiH–Ir catalyst, which exhibits an ammonia production rate of 7.7 mmol g^{-1} h^{-1} at 400 °C and 1.0 MPa. This rate was *ca.* 100-fold higher comparing the bulk LiH–Ir composite and the MgO-supported Ir metal catalyst. The study disclosed that the *in situ* formation of Li–Ir complex hydride species led to the activation and hydrogenation of nitrogen to ammonia.[86]

Inoue *et al.* reported ammonia synthesis over flat-shaped Ru NPs decorated on calcium amide, $Ca(NH_2)_2$.[87] The catalyst was able to fix N_2 to ammonia at a temperature as low as 200 °C under 0.1 MPa. The ammonia production using $Ca(NH_2)_2$ was primarily *via* its decomposition reaction ($Ca(NH_2)_2 \rightarrow CaNH + NH_3$). However, 10 wt% $Ru/Ca(NH_2)_2$ acted as a stable catalyst and produced *ca.* 37.8 mmol ammonia within 45 h, at 340 °C and 0.1 MPa. The rate significantly reached to a maximum of 9.6 mmol g^{-1} h^{-1} at 350 °C. Such high activity was attributed to the high electron promotion effect of $Ca(NH_2)_2$. While $Ca(NH_2)_2$ alone shows a rapid decline in ammonia production over time (Fig. 11a), $Ru/Ca(NH_2)_2$ remains highly efficient, with a substantial increase in ammonia production compared to the decomposition of $Ca(NH_2)_2$. The catalytic activity of $Ru/Ca(NH_2)_2$ is shown to be superior to that of Cs–Ru/MgO across the entire temperature range, with ammonia production

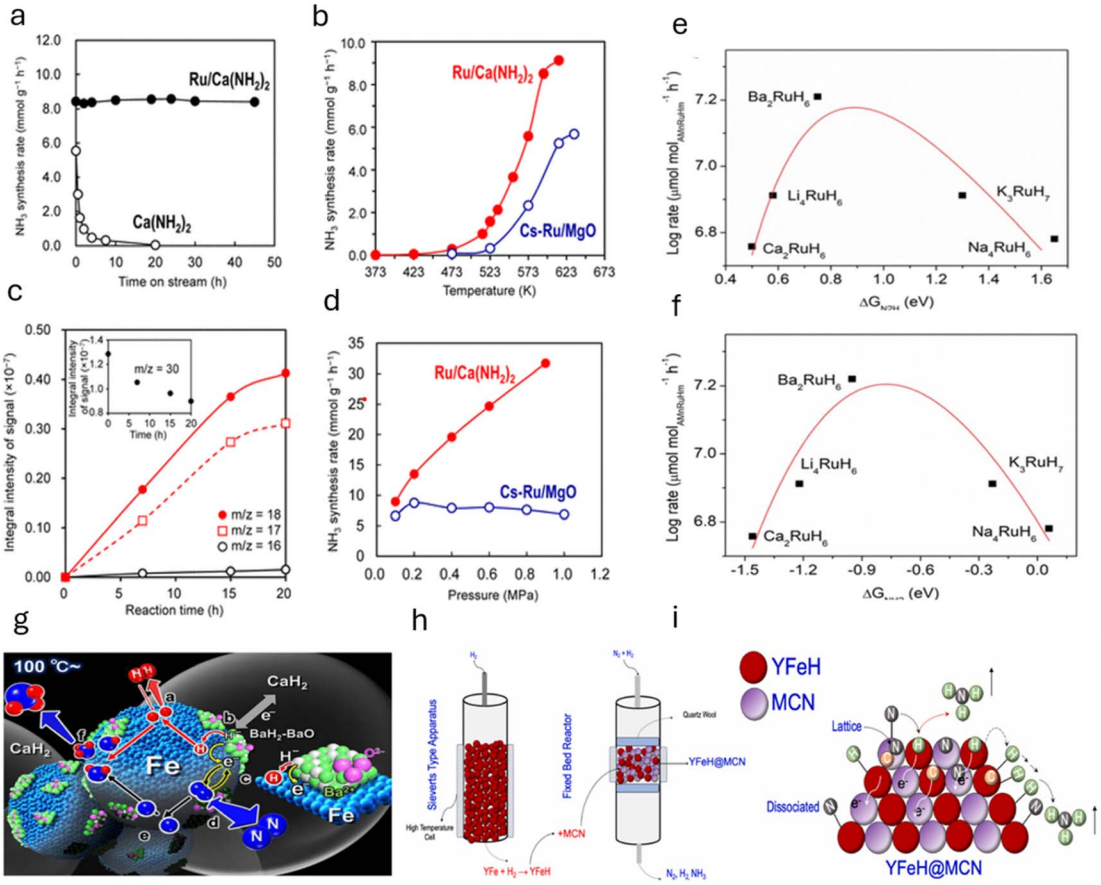

Fig. 11 (a) NH_3 synthesis over $Ca(NH_2)_2$ and 8 wt% $Ru/Ca(NH_2)_2$ at 613 K (340 °C) and 0.1 MPa over time. (b) NH_3 synthesis rate *versus* temperature for 10 wt% $Ru/Ca(NH_2)_2$ and 10 wt% Ru–Cs/MgO at 0.1 MPa. (c) NH_3 synthesis over $Ru/Ca(NH_2)_2$ from $^{15}N_2$ and H_2 at 473 K (200 °C) and 45 kPa; the inset shows $^{15}N_2$ concentration over time. (d) NH_3 synthesis rate at 613 K (340 °C) for 10 wt% $Ru/Ca(NH_2)_2$ and 10 wt% Ru–Cs/MgO at different pressures. Adapted with permission from ref. 87. Copyright 2016, the American Chemical Society. (e) Volcano-type plot for ammonia synthesis reactions over $AM_n[RuH_m]$ (AM = Li, Na, K, Ca, and Ba) catalyst series at 300 °C and 0.1 MPa with the descriptor of the interaction strength between AM cations and N_xH_y species as the N_2H adsorption energy and (f) NH_2 adsorption energy. Adapted with permission from ref. 79. Copyright 2023, American Chemical Society. (g) Illustration of the reaction mechanism for ammonia synthesis on BaH_2–BaO/Fe/CaH_2. Adapted from the work of Hattori *et al.*,[26] licensed under CC BY 4.0 (https://creativecommons.org/licenses/by/4.0/). (h) YFeH is synthesized in a Sieverts-type apparatus and then mixed with MCN to form YFeH@MCN, which subsequently reacts with N_2 and H_2 to produce ammonia. (i) Schematic representation of ammonia formation on YFeH@MCN catalyst, which contains both dissociated and lattice nitrogen, which reacts with hydrogen from YFeH or dissociated hydrogen in sequential steps to form ammonia. Adapted with permission from ref. 88. Copyright 2024, Elsevier.

starting as low as 473 K (200 °C), whereas Cs–Ru/MgO shows no detectable ammonia production below 523 K (250 °C) (Fig. 11b). The time-course of ammonia synthesis from $^{15}N_2$ and H_2 at 473 K (200 °C) further confirms that ammonia is synthesized directly from the gas phase, and the signals for $^{15}NH_3$ and $^{15}NH_2$ increase over time, providing clear evidence of N_2 dissociation and NH bond formation (Fig. 11c). The ammonia synthesis rate over $Ru/Ca(NH_2)_2$ is shown to increase with reaction pressure, with the catalyst remaining unaffected by hydrogen poisoning, unlike Cs–Ru/MgO. These findings demonstrate that $Ru/Ca(NH_2)_2$ offers a highly efficient, stable, and low-temperature alternative for ammonia synthesis (Fig. 11d).

This study also unveils the role of Ba-doping into the catalytic system that led to no degradation in the activity profile after *ca.* 700 h of operations, since most of the conventional catalysts have a dissociative path for ammonia synthesis, which leads to a lower ammonia yield under low-temperature conditions.

Keeping this in mind, Wang *et al.* examined the catalytic performance of strategically designed ternary ruthenium complex hydrides, Li_4RuH_6 and Ba_2RuH_6, consisting of electron- and hydrogen-rich $[RuH_6]$ anionic centers.[89] Herein, it is illustrated that the reduction of nitrogen occurs through the dual effect of multiple electron-rich sites and lattice hydridic hydrogen (acting as a proton and electron carrier). This resulted in an activity of 150 and 120 μmol g^{-1} h^{-1} observed for the bulk phase of Li_4RuH_6 and Ba_2RuH_6, respectively, at (<300 °C, 0.1–1.0 MPa). In the as-designed catalysts, Ru is in the ionic state and coordinated with six hydridic hydrogens, which forms electron-rich anions ($[RuH_6]^{4-}$) spatially located in the K_4CdCl_6 (or K_2PtCl_6)-type framework of Li (or Ba) cations. Such configuration promotes the associative hydrogenolysis of nitrogen through the support of $[RuH_6]^{4-}$ centers, lattice hydridic hydrogens, and nearby Li or Ba cations. Additionally, the intermediates N_xH_y were enhanced by the Li/Ba cations, which positively impact the effectiveness of the catalyst. Hence, this work successfully exhibits that a transition-metal complex can reduce nitrogen *via* a non-dissociative pathway. As a follow-up work, the authors performed both experimental and theoretical works to gain more insights into the mechanistic details for ammonia formation over Ba_2RuH_6. The work unveils that Ba_2RuH_6 offers multifunctional and redox-active catalytic center for non-dissociative N_2 reduction. Herein, Ba provides the site for N_2 activation and H_2 dissociation in synergy with Ru metals. Hence, at 300 °C and 0.1 MPa, the production rates of NH_3 over Ba_2RuH_6 were *ca.* 25, 6.3 and 9.5 times greater than that of Ru/MgO, Cs_2O–Ru/MgO, and BaO–Ru/MgO catalysts and reached the thermodynamic limit at 325 °C under a space velocity of 7500 mL g^{-1} h^{-1}. Importantly, the catalyst displayed a positive reaction order (=1.0) with respect to H_2 at 300 °C. The findings suggest that barium donates electrons and bonds with N_xH_y species.

In a similar study by Prof. Chen's group, the performance of a series of ruthenium complex hydrides $AM_n[RuH_m]$ (AM = Li, Na, K, Ca, or Ba) was examined to compare the catalytic performance with Li_4RuH_6 and Ba_2RuH_6 catalysts.[79] In comparison, under a total pressure of 1.0 MPa and at temperatures above 300 °C, the activities of supported Ru complex hydride catalysts were following this trend: $Ba_2RuH_6/MgO \approx K_3RuH_7/MgO > Li_4RuH_6/MgO > Na_4RuH_6/MgO > Ca_2RuH_6/MgO$, whereas, at temperatures below 300 °C, the activity order was $Ba_2RuH_6/MgO > Li_4RuH_6/MgO > Ca_2RuH_6/MgO > Na_4RuH_6/MgO > K_3RuH_7/MgO$. In particular, the Ca_2RuH_6 sample demonstrated an activity of *ca.* 0.22 mmol g^{-1} h^{-1} at 300 °C and 0.1 MPa. The authors also tested the kinetic parameters and found that in general, Ca_2RuH_6/MgO, Li_4RuH_6/MgO, and Ba_2RuH_6/MgO catalysts exhibited low values of apparent activation energies than the Ru metal catalysts, indicating their high activity at lower temperatures. Interestingly, Ru-metal-based catalysts exhibit negative H_2 orders, which lead to notorious hydrogen poisoning of the catalysts; however, Ca_2RuH_6/MgO, Li_4RuH_6/MgO, and Ba_2RuH_6/MgO have positive reaction orders with respect to H_2, suggesting that these catalysts alleviate the issue of hydrogen poisoning. Insights into the mechanistic details reveal that the bonding strengths between AM cations and the reacting N_xH_y species govern the excellent features of AM-promoted Ru metal catalysts.

The N_2H and NH_2 adsorption energies of these hydrides were plotted against their respective activities, and a volcano-shaped plot was observed in both cases (Fig. 11e and f). Ca_2RuH_6 and Li_4RuH_6 work well at lower temperatures due to their low N_xH_y adsorption energies. This favors the activation of N_2 over the formation and desorption of NH_3. Ba_2RuH_6 has a moderate N_xH_y adsorption energy (exactly in between both plots), indicating that it would enhance ammonia synthesis for a wide range of temperatures. K_3RuH_7 and Na_4RuH_6, however, have high N_xH_y adsorption energies owing to which NH_3 formation is preferred over N_2 activation, resulting in good ammonia production at higher temperatures.

Next, Fe-based catalysts are considered first-generation classical transition metals for ammonia synthesis due to their significantly high rate under high-temperature and high-pressure reaction conditions. However, these catalysts have low activity at low temperatures. Using support materials with Fe can enhance the activity of the catalyst under mild reaction conditions. Hattori *et al.* discovered that metallic iron particles can help make ammonia from hydrogen (H_2) and nitrogen (N_2) at 100 °C when combined with BaH_2. Iron works much better than other metals such as Ru, Co, and Ni because it releases hydrogen atoms (H adatoms) as H_2 molecules at low temperatures (<100 °C). Other metals such as Ru, Co, and Ni hold onto hydrogen atoms more strongly, which can poison the catalyst and make it less effective at higher temperatures (>150–200 °C). Using support materials with Fe can enhance the activity of the catalyst under mild reaction conditions. For instance, in 2024, Michikazu Hara's group reported that Fe-based catalysts can produce ammonia *via* low-temperature reactions when supported with BaH_2. An ammonia synthesis rate of 720 μmol g^{-1} h^{-1} was obtained at a temperature of 200 °C and a pressure of 0.9 MPa for the catalyst $BaH_2/BaO/Fe/CaH_2$. Such significantly high rate observed at low temperatures was attributed to the strong electron-donating nature of Fe in the presence of BaH_2. Moreover, it was observed that the hydrogen poisoning effect

Table 5 Intermetal-based catalysts

S. no.	Catalyst	Temp. (°C)	Pressure (MPa)	Rate (mmol g^{-1} h^{-1})	Activation energy (kJ mol^{-1})	Metal%	WHSV	N_2 order	H_2 order	NH_3 order	Surface area (m^2 g^{-1})	Turnover frequency (TOF) (s^{-1})	Catalyst synthesis method	Ref.
1	$Ru/Ti_{0.04}$–Ce	400	1	11.009	—	1.9% Ru, 5.1% TiO_2	36 000	—	—	—	62	10.8×10^{-3}	Hydrothermal; co-precipitation method	96
2	$Ru/Ti_{0.13}$–Ce	400	1	15.2	—	2.2% Ru, 14.8% TiO_2	36 000	0.27	0	−0.56	61	—	Hydrothermal; co-precipitation method	96
3	$Ru/Ti_{0.18}$–Ce	400	1	18.912	—	2.1% Ru, 19.4% TiO_2	36 000	0.5	0.47	−1.07	65	18.7×10^{-3}	Hydrothermal; co-precipitation method	96
4	$Ru/Ti_{0.25}$–Ce	400	1	13.5	—	2.2% Ru, 25.3% TiO_2	36 000	0.61	0.20	−1.14	64	—	Hydrothermal; co-precipitation method	96
5	$Ru/Ti_{0.35}$–Ce	400	1	9.773	—	2.2% Ru, 32.0% TiO_2	36 000	—	—	—	62	9.6×10^{-3}	Hydrothermal; co-precipitation method	96
6	$Ru/Ti_{0.98}$-Ce	400	1	7.120	—	2.0% Ru, 57.2% TiO_2	36 000	0.84	−0.17	−1.53	55	7.0×10^{-3}	Hydrothermal; co-precipitation method	96
7	$LaNi_{5\ (bulk)}$	400	0.1	0.25	50.1	67.269 (Ni)	36 000	—	—	—	0.4	—	Arc melting method	97
8	$LaNi_5$ NPs	400	0.1	4.487	53.8	67.235 (Ni)	36 000	1.28	1.60	−1.74	38.7	—	Ar/H_2 arc evaporation method	97
9	Ru/LaCoSi	400	0.1	3.4	50	4.3 (Ru)	18 000	1	1.17	−1.06	2.6	0.03	Arc melting; CVD method	98
10	Ru/LaFeSi	400	0.1	2.8	56	4.4	18 000	0.99	0.94	−1	3.1	0.027	Arc melting; CVD method	98
11	Ru/LaMnSi	400	0.1	1.1	57	4.7	18 000	0.98	1.10	−0.93	3.9	0.012	Arc melting; CVD method	98
12	$Ru_{1.4}$/LaScSi	400	0.1	3.9	—	1.4	36 000	—	—	—	1	2	Arc melting and annealing method	99
13	$Ru_{1.7}$/LaScSi	400	0.1	2.33	—	1.7	36 000	—	—	—	1	2.4	Arc melting and annealing method	99
14	$Ru_{1.7}$/CeScSi	400	0.1	2.25	—	1.7	36 000	—	—	—	1	1.9	Arc melting and annealing method	99
15	$Ru_{1.7}$/PrScSi	400	0.1	2.2	—	1.7	36 000	—	—	—	1	2.6	Arc melting and annealing method	99
16	$Ru_{1.7}$/NdScSi	400	0.1	2	—	1.7	36 000	—	—	—	1	1.4	Arc melting and annealing method	99
17	$Ru_{1.5}$/SmScSi	400	0.1	1.2	—	1.5	36 000	—	—	—	1	1.9	High-frequency induction melting method	99
18	$Ru_{1.3}$/GdScSi	400	0.1	0.5	—	1.3	36 000	—	—	—	1	1	Arc melting and annealing method	99

was not happening under low-temperature reaction conditions. A plausible reaction mechanism of ammonia synthesis on BaH_2–BaO/Fe/CaH_2 is shown in Fig. 11g.

Recently, our group has shown that combining yttrium hydride with molybdenum carbonitride can play a pivotal role in low-temperature ammonia synthesis reactions. As reported in one of our work,[88] molybdenum-based carbide can give ammonia under ambient pressure conditions; however, the reaction occurs at high temperatures. This work succeeds a previous work by our group on enhancing ammonia synthesis using a transition metal (Fe and Co)-modified Mo_2C catalyst.[90] Mixing it with yttrium hydride has started producing ammonia even at 200 °C. The ammonia synthesis activity 232 μmol g^{-1} h^{-1} was given at 200 °C and 0.1 MPa for the catalyst composition 10 : 90 (MCN : YH). YFeH was synthesized in a Sieverts-type apparatus followed by mixing with MCN to form YFeH@MCN. The synthesis method is depicted in Fig. 11h. Moreover, the ammonia synthesis rate was increased after changing the catalysts' weight ratio and temperature. For example, the catalyst MCN : YH (5 : 95) has shown a rate of 448 μmol g^{-1} h^{-1} at a temperature of 255 °C and a pressure of 0.1 MPa. Such high activity for ammonia synthesis under low-temperature reaction conditions could be possible due to the presence of hydride support, as it is found that the hydride-based materials under ammonia synthesis reaction conditions have the ability to generate electrons by splitting into protons and electrons. Moreover, *in situ* generated hydride directly participates in an ammonia synthesis reaction by following M–H pathways (M = metals), which plays an essential role in high ammonia generation rate. From our experimental findings, we observed that yttrium hydride enhanced the electron density, which was used by MCN to dissociate nitrogen molecules efficiently under low-temperature reaction conditions. The schematic mechanism of ammonia formation over YFeH@MCN is shown in Fig. 11i.

The low stability of hydride-based catalysts under reaction conditions remains a critical challenge, as they tend to degrade during prolonged exposure to synthesis environments. One effective strategy to address this issue is the implementation of chemical looping reactions, which can not only prevent stability issues but also enhance ammonia synthesis activity by maintaining the catalyst's structural integrity. Furthermore, designing hydrides with improved thermal and chemical stability, along with exploring novel hydride compositions, could further augment their durability and broaden their applicability in industrial ammonia synthesis.

3.3 Intermetallic-based catalysts

In recent years, a significant shift in ammonia synthesis methods has been underway, with a growing consensus to utilize intermetallic compounds. Intermetallic catalysts are composed of two or more metals that form a crystalline structure, offering unique properties beneficial for ammonia synthesis. These catalysts are highly active due to the synergy between the metal components, optimizing electronic properties and enhancing catalytic sites for nitrogen activation. In particular, these compounds consist of a rare earth metal and an active transition metal, and therein, the rare earth metal transfers electrons to the transition metal that facilitates dissociation of nitrogen molecules by lowering the activation barrier of ammonia synthesis.[91,92] Their ability to reversibly store hydrogen prevents hydrogen poisoning, maintaining active catalytic sites and improving overall efficiency.[93–95] Table 5 lists the ammonia synthesis activity of intermetallic-based catalysts under low-pressure and low-temperature conditions.

Optimally tuned electronic and geometric structures conferred by the intermetallic catalyst, which is a well-defined ordered metal alloy, provide better catalytic performance for ammonia synthesis. Optimizing metal–metal interactions promotes nitrogen activation by decreasing the energy barrier for N≡N bond cleavage.

Arc melting method was used to synthesize $LaNi_5$ bulk.[97] For this preparation, lanthanum and nickel in their elemental form were taken in a copper hearth and then arc melted in an inert (Ar) atmosphere, which resulted in the formation of silver-coloured ingots. The intense heat during arc melting allows proper mixing and alloying of the metals, which leads to the formation of homogeneous $LaNi_5$ ingots upon solidification. These ingots were then ground in an agate mortar. For the preparation of $LaNi_5$ nanoparticles (NPs), the obtained $LaNi_5$ ingots were treated in an Ar/H_2 arc evaporation system, where the temperature goes as high as 10 000 °C, which vaporizes the base materials. In this process, the partial pressures of Ar and H_2 were set to 0.03 and 0.03 MPa, respectively, at an air flow rate of 60 mL min^{-1}. To avoid exposing $LaNi_5$ NPs to air, the filter room was detached from the evaporation system and NPs were directly collected from there.

The chemical vapour deposition method incorporates Ru-loaded catalysts on La–TM–Si[98] intermetallic compounds in which $Ru_3(CO)_{12}$ was deposited through a programmable temperature ramp method. In the CVD method, the metal precursors vaporize and decompose at controlled temperatures allowing Ru atoms to deposit on the La–TM–Si surface, which allows a uniform Ru catalyst layer. La rods, TM granules and Si pieces were taken in stoichiometric amounts and arc melted in an argon atmosphere. The ingots thus obtained were annealed for a duration of 5 days at a temperature of 1000 °C and then cooled down to 800 °C and held for 10 more days. The final step was grounding in a glovebox to obtain fine powders. Ru was loaded on La–TM–Si by a chemical vapour deposition method using a $Ru_3(CO)_{12}$ precursor. Both the powders were taken in a silica tube, which was temperature programmed to heat to 70 °C, held for 1 h and then to 120 °C for another 2 h and finally to 250 °C for last 2 h followed by cooling to room temperature to obtain the catalyst in its final form. The SEM images of LaCoSi, Ru/LaCoSi, Ru/LaFeSi and Ru/LaMnSi can be seen in Fig. 12c–f, respectively.

In a similar work, *R*ScSi[99] with *R* = La, Ce, Pr, Nd, Sm, and Gd were synthesized by melting the metallic powders beginning with rare earth ingots, Sc pieces and Si lumps. A high-frequency furnace was used to vaporize volatile oxides while melting the rare earth metals. The metal samples were arc melted for 5 times in an argon atmosphere followed by annealing at

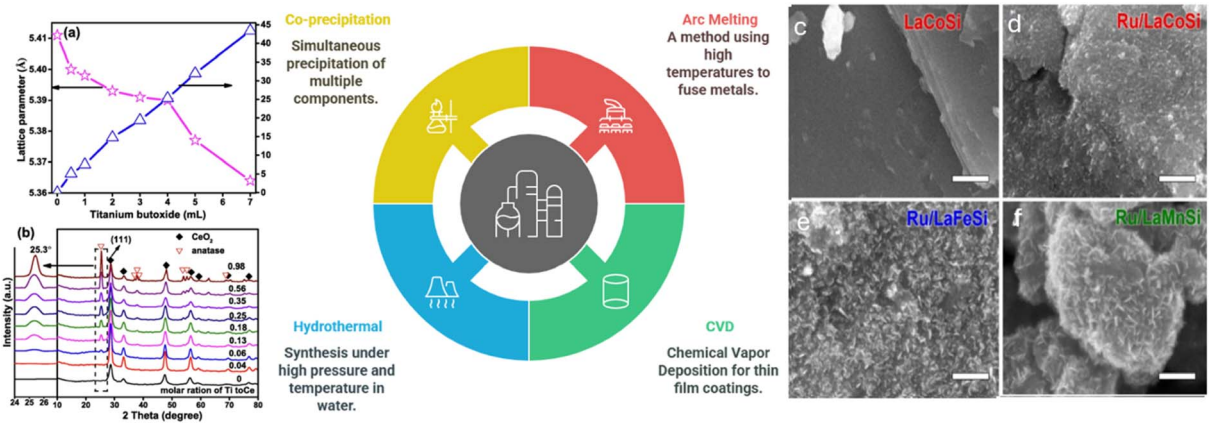

Fig. 12 (a) Lattice parameters and TiO_2 content variation with titanium butoxide volumes. (b) XRD crystallographs of Ti-doped CeO_2 prepared *via* a combination of hydrothermal and co-precipitation methods. Adapted with permission from ref. 96. Copyright 2022, Elsevier. SEM images of (c) LaCoSi, (d) Ru/LaCoSi, (e) Ru/LaFeSi and (f) Ru/LaMnSi catalysts prepared *via* a combination of arc-melting and CVD methods. Adapted with permission from ref. 98. Copyright 2022, Elsevier.

a temperature of 900 °C for a period of 4 weeks. The buttons so obtained were crushed and sieved before depositing Ru NPs. Ru was loaded on *R*ScSi pristine phases by a chemical vapor deposition method using $Ru_3(CO)_{12}$ as a Ru precursor.

The combination of hydrothermal and co-precipitation methods was used to synthesize a Ru/Ti_x–Ce[96] catalyst. Cerium nitrate was dispersed in ethanol, added to an aqueous NaOH solution, and stirred for 30 minutes followed by hydrothermal treatment at 100 °C for 24 h. During hydrothermal treatment, the nitrate precursors react with NaOH under heat and pressure, which leads to phase transformation and controlled crystallization in a liquid medium. The resulting precipitate was washed with DI water and ethanol to make the pH 7, which yielded a gel. This gel was dried and calcined at a temperature of 550 °C for 4 h to obtain CeO_2. Now titanium butoxide and ethanol mixed solution was added to this gel followed by pH adjustment to 10 using ammonia solution and then the mixture was heated at 80 °C for 2 h. In the co-precipitation method, simultaneous precipitation of multiple components occurs by adjusting pH, ensuring uniform composition and fine particle dispersion. Finally, after drying and calcination, ruthenium was loaded on Ti_x–Ce by the usual wetness impregnation method using ruthenium nitrosyl nitrate as the precursor. Fig. 12a shows the variation of lattice parameters and TiO_2 contents with titanium butoxide volumes.

$LaNi_5$ is a famous and well-investigated hydrogen storage material, which can store up to 1.40 wt% H_2 at room temperature.[100] Therefore, $LaNi_5$ has attracted attention for designing ammonia synthesis catalysts in combination with inexpensive transition metals. For instance, Ye *et al.* designed a Ni–LaN core–shell structure by mixing $LaNi_5$ (prepared from arc-melting method) and Ni (from thermal decomposition of nickelocene ($Ni(C_5H_5)_2$)) in an Ar-filled glovebox. The mixture was subsequently heated to 250 °C for 1.5 h in pure H_2 (flow rate = 2.5 mL min^{-1}; pressure = 0.1 MPa).[97] The catalytic activity of the as-prepared Ni–LaN catalyst was as high as 4.5mmol g^{-1} h^{-1} at 400 °C and 0.1 MPa with low activation energy (*ca.*50 kJ mol^{-1}), which was about 20-fold greater than that of the $LaNi_5$ bulk particles. However, one of the issues with $LaNi_5$ is its phase separation of LaH_x and Ni metal after reversible H_2 storage, even at room temperature.[101–103] Herein, during ammonia synthesis reaction, high temperatures readily induced such phase separation of $LaNi_5$ to LaH_x, which combined with N_2 to form LaN (*i.e.*, $LaNi_5 + 1.5H_2 + N_2 \rightarrow LaN + 5\,Ni + NH_3$). Notably, these thin layers of LaN further prevent the decomposition of the internal $LaNi_5$, providing stability to the catalytic performance. The decomposition process of $LaNi_5$ in the bulk and nanoparticle samples is represented in Fig. 13a and b.

Therefore, this work illustrates the excellent application of Ni by combining with early transition metal La, which is supposed to have low activity for ammonia synthesis, obeying the scaling rules of pure metals predicted from the volcano plot.

The application of intermetallic compounds for ammonia synthesis is not limited to the combination of two metals. In the absence of Ru metals, a dual-site mechanism was reported for LaCoSi and LaFeSi in a study by Li *et al.*[104] The ammonia synthesis rates of LaCoSi, LaFeSi and LaMnSi were 1.22, 0.62, and 0.12 mmol g^{-1} h^{-1}, respectively, at 0.1 MPa and 400 °C. The activation energies were 42, 43, and 54 kJ mol^{-1} for LaCoSi, LaFeSi and LaMnSi, respectively. The reaction order for H_2 was positive, suggesting the absence of the hydrogen poisoning effect. Further findings indicate that N_2 activation occurs on the transition metals site and N hydrogenation happens on the La site. However, in the case of La–Mn–Si, the mobility of N from Mn to La was inhibited, which led to poor hydrogenation of N atoms on the Mn site, and therefore, low activity was observed for this catalyst system. The illustration for the same can be found in Fig. 13c and d.

Gong *et al.* synthesized La–TM–Si (TM = Co, Fe, and Mn) by a conventional arc-melting method. Further, these powders were mixed with an Ru precursor (*i.e.*, $Ru_3(CO)_{12}$), sealed in a silica tube, and heated. The as-prepared catalysts were then examined for their ability to shift the rate-limiting step from the

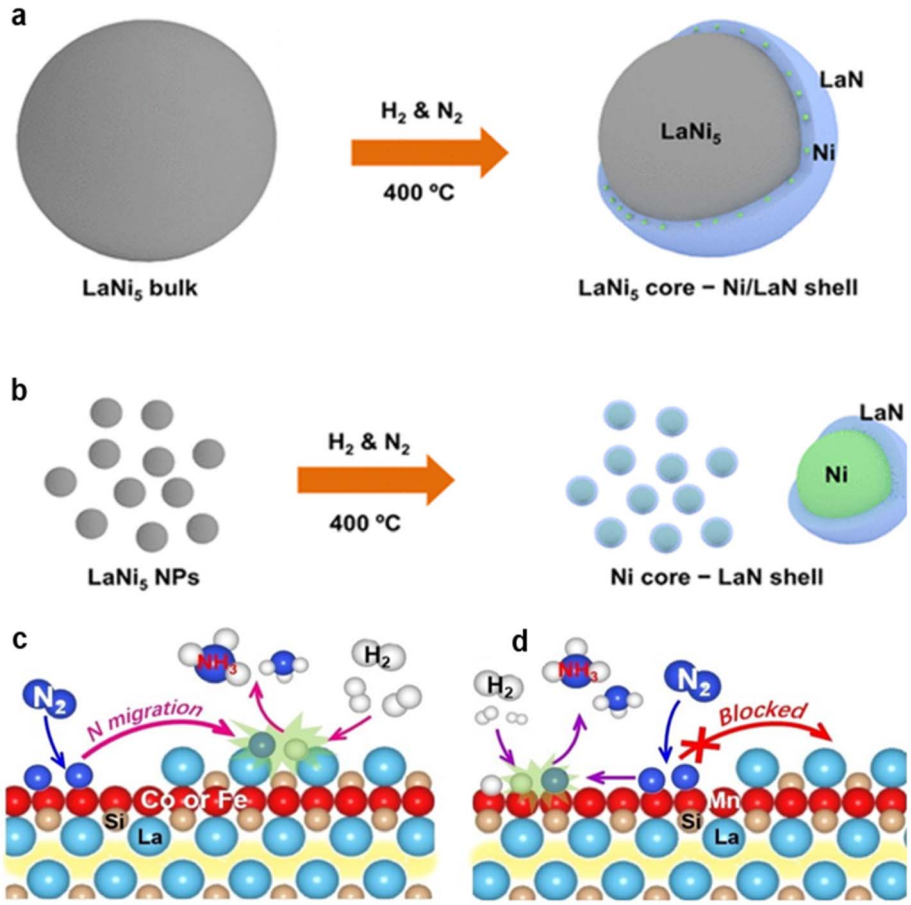

Fig. 13 (a) Illustrations of the decomposition process during ammonia synthesis reaction over $LaNi_5$ bulk and (b) $LaNi_5$ nanoparticles. Adapted with permission from ref. 97. Copyright 2020, the American Chemical Society. (c) Ammonia synthesis mechanism over La–TM–Si (TM = Co and Fe) and (d) LaMnSi. Colour scheme of elements is as follows-light blue: La; red: TM; tawny: Si; dark blue: N; white: H. Adapted with permission from ref. 104. Copyright 2023, John Wiley and Sons.

slow nitrogen dissociation to NH_x formation.[93] With 2 wt% Ru loading, these catalysts exhibited ammonia synthesis rate as high as 1.28, 3.88, and 5.23 mmol g^{-1} h^{-1} for Ru/LaMnSi, Ru/LaFeSi, and Ru/LaCoSi, respectively. Despite the fact that Ru/LaMnSi and Ru/LaFeSi have identical work function values, the latter showed a much higher activity, which clearly demonstrate that the activity is not solely dependent on the electron donation ability of the support (or electride materials). However, the activity was observed to be dependent on Ru-loading but independent of the surface area of the catalysts.

Fig. 14a highlights the superior catalytic performance of Ru/La–TM–Si catalysts, where increased Ru loadings and favourable reaction kinetics result in enhanced ammonia synthesis. The low activation energies (Fig. 14b) confirm a distinct reaction pathway that differs from conventional catalysts, with efficient N_2 activation, as shown by the N_2 reaction orders (near-unity) (Fig. 14c). Additionally, the positive H_2 reaction orders (Fig. 14d) imply resistance to hydrogen poisoning, which is typically problematic for other catalysts. The synthesis rate consistently rises with increasing pressure, underscoring the catalyst's robust performance under different conditions, particularly for Ru/LaCoSi (Fig. 14e and f). This highlights the role of La–TM–Si supports in enabling effective ammonia production by providing reversible hydrogen storage and minimizing adverse interactions with H_2.

Croisé *et al.* used Ru/*R*ScSi (*R* = La, Ce, Pr, Nd, Sm, and Gd) to investigate the activity of various rare earth metals for ammonia synthesis at 300–450 °C and under 0.1–0.5 MPa.[99] The activity trend from La to Gd lanthanide series is as follows: $Ru_{1.7}$/LaScSi = $Ru_{1.7}$/CeScSi = $Ru_{1.7}$/PrScSi > $Ru_{1.7}$/NdScSi > $Ru_{1.5}$/SmScSi > $Ru_{1.3}$/GdScSi, which was found to be strongly dependent on their respective hydride phases. These catalysts were arc-melted under a pure argon atmosphere. Notably, $Ru_{1.7}$/CeScSi displayed catalytic activity of 0.58 mmol g^{-1} h^{-1} at 300 °C and 0.1 MPa, which is closely related to its reversible hydrogen-storage properties. Moreover, this was ascribed to the prevention of hydrogen poisoning of the Ru surface, and therefore, it is concluded that the electron-donating effect of such electrides can be tuned *via* partial hydrogenation of the *R*ScSi materials. Through extensive experiments, it was evident that the *R*ScSi support facilitates the nitrogen dissociation with possible storage of N-species and the hydrogen present in the formed ammonia stems from hydrogen gas and not from the hydride

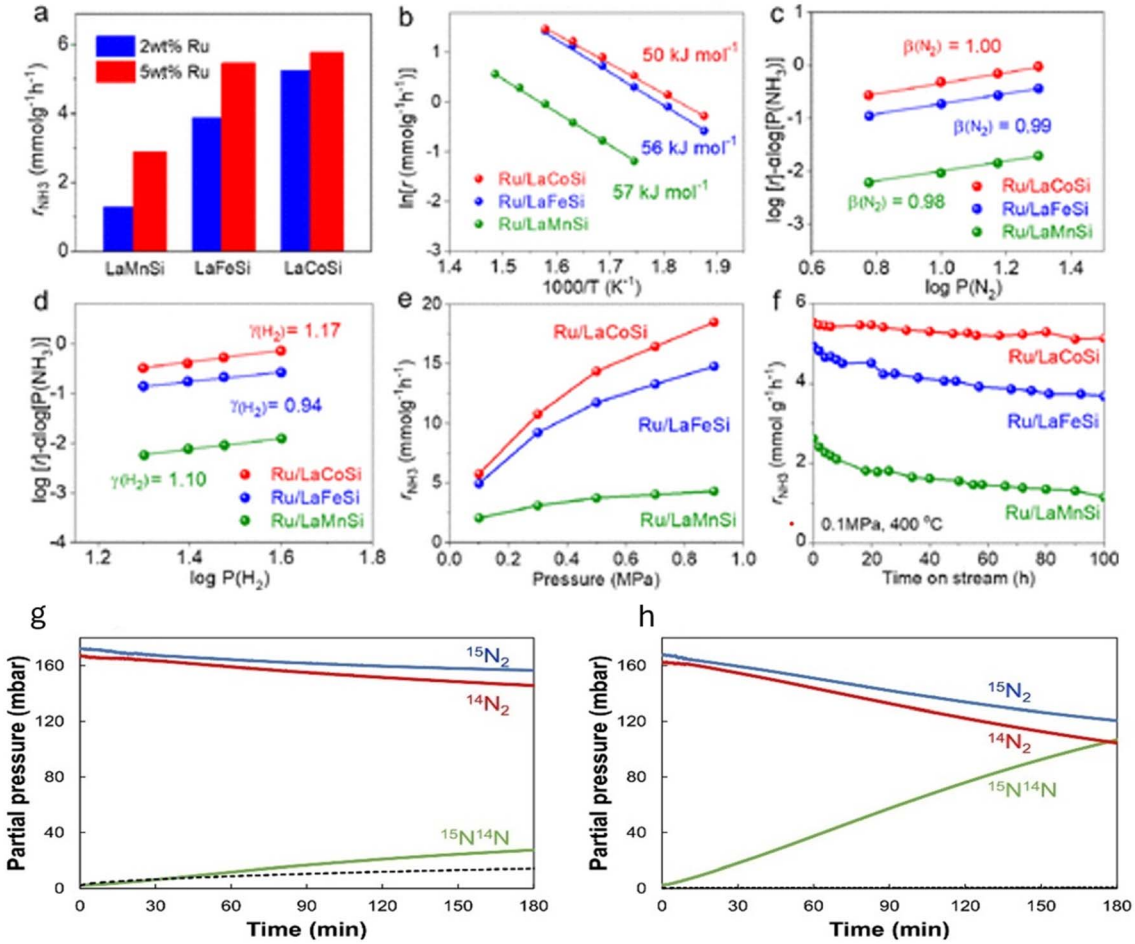

Fig. 14 (a) Catalytic activity of Ru/La–TM–Si with varying Ru loadings at 0.1 MPa, 400 °C, and $N_2/H_2 = 15:45$ mL min^{-1}. (b) Arrhenius plots for ammonia synthesis over Ru/La–TM–Si. (c) Reaction orders for N_2 and (d) H_2 calculated using the power law equation at 0.1 MPa. (e) Effect of pressure on ammonia synthesis for 5 wt% Ru/La–TM–Si. (f) Ammonia production over time for Ru/La–TM–Si at 400 °C, 0.1 MPa, with $N_2/H_2 = 15:45$ mL min^{-1}. Each experiment used 0.1 g of catalyst. Adapted with permission from ref. 98. Copyright 2022, the American Chemical Society. (g) Nitrogen isotopic distribution during the homomolecular exchange of $^{15}N_2/^{14}N_2$ at 500 °C for $RuLaScSiH_{1.5}$ and (h) partially dehydrogenated $RuLaScSiH_x$, treated under Ar at 500 °C for 2 hours. The dashed line indicates the change in H_2 partial pressure ($m/z = 2$ signal). Adapted with permission from ref. 105. Copyright 2023, Elsevier.

phase. Importantly, it was speculated that the formation/desorption of NH_x species could be the rate-limiting step.

In a follow-up work, Croisé *et al.* investigated LaScSi and CeTiGe using DFT calculations and $^{15}N/^{14}N$ homomolecular exchange experiments to establish a correlation between the electride-type material characteristics, partial hydrogenation of the structure and the efficiency for dissociative nitrogen activation (Fig. 14g and h).[105] It was found that Ru/LaScSi was relatively more active, owing to their electride-like properties, which were substantially increased when the catalyst was partially hydrogenated, and subsequently, led to a greater activity in a nitrogen equilibration reaction. Although no electride-like properties are present in the Ru/CeTiGe catalyst, this article unveils that the catalyst follows the associative mechanism to produce ammonia.

While the high efficiency of intermetallic catalysts might seem promising, they often rely on rare-earth metals, which are expensive and limited in supply, making them economically unfeasible for large-scale use. Additionally, under high-temperature and high-pressure conditions, these catalysts may suffer from sintering or phase changes, leading to reduced performance. The synthesis of intermetallic is also complex, requiring precise control of composition and processing conditions. To overcome these challenges, research should focus on finding cost-effective alternatives to rare-earth metals, improving catalyst stability under harsh conditions, and exploring advanced synthesis methods to enhance their performance and scalability for industrial ammonia synthesis.

3.4 Electride-based catalysts

Electrides are crystals in which cavity-confined electrons act as anions, and were first prepared by J. L. Dye in 1983 using crown ethers.[106,107] Generally, these electrons are trapped in an anion vacancy site, known as F-center (a point defect). The high electron concentration in the F-center makes electrides very active. These trapped electrons play a pivotal role in catalysis by

Table 6 Electride-based catalysts

S. no.	Catalyst	Temp. (°C)	Pressure (MPa)	Rate (mmol g^{-1} h^{-1})	Activation energy (kJ mol^{-1})	Metal%	WHSV	N_2 order	H_2 order	NH_3 order	Surface area (m^2 g^{-1})	Turnover frequency (TOF) (s^{-1})	Catalyst synthesis method	Ref.
1	$Ru/BaAl_2O_{4-x}H_y$	340	0.9	13.304	65.7	2	36 000	0.72	1.02	−1	—	5.7×10^{-2}	Solid state reaction method; hydrogenation method	108
2	$Ru/BaAl_2O_4$	340	0.9	—	—	2	36 000	1.29	0.30	−0.66	—	—	Solid state reaction method	108
3	LaRuSi	400	0.1	Activity/surface area = 1433 μmol m^{-2} h^{-1}	42	—	—	—	—	—	1.2	—	Arc melting method	109
4	CaRuSi	400	0.1	35 μmol m^{-2} h^{-1}	—	—	—	—	—	—	1.5	—	Solid-state reaction method	109
5	$Ru/C_{12}A_7{:}O^{2-}$	400	0.1	—	—	1.60	30 cm^3 min^{-1}	—	—	—	—	0.015	Modified Pechini method	110
6	$Ru/C_{12}A_7{:}e^-$	400	0.1	1.5	72	2	30 cm^3 min^{-1}	0.7	0.3	—	—	0.087	Aluminothermic reduction method	110
7	Ru/BaO_xN_y e^-_z ($x = 0.5$)	400	0.1	2.050	62	1.8	36 000	—	—	—	0.7	0.292	Solid-state reaction method	76

donating electrons to transition metals. The transition metals, in turn, can back-donate these electrons to the nitrogen molecules, facilitating the activation of N_2. This electron transfer mechanism significantly enhances the catalytic activity of electrides, making them highly efficient for N_2 activation in ammonia synthesis. As a result, such materials with unique electronic structures and composed of oxides (such as CaO, and Al_2O_3) offer a low work function, compared to alkali metals. Moreover, electrides are chemically inert and thermally stable. Consequently, this material finds huge application in ammonia synthesis under mild conditions because these surface electrons can readily be transferred to the transition metals *via* an energetically favorable step. The performances of various electride-based catalysts and their corresponding synthesis methods are shown in Table 6.

Electride-based catalysts for ammonia synthesis enhance the activation of nitrogen sites by providing strong sites characterized by highly active electron donation important for the cleavage of the N≡N bond. The method of preparation of these catalysts emphasizes the optimization of their electronic properties.

$BaAl_2O_{4-x}H_y$ and BaO_xN_y[108] were synthesized by a solid-state reaction method to obtain the desired phase purity and to carry out high-temperature processing for controlled composition. The high temperature in this method induces diffusion-driven chemical reactions between solid reactants, leading to phase formation. γ-Al_2O_3 was made to react with BaH_2 with the addition of $BaCO_3$ under H_2 flow. The purpose of addition of $BaCO_3$ was to increase the purity of $BaAl_2O_{4-x}H_y$. BaH_2 was synthesized by the reaction of metallic Ba and H_2 at a temperature of 450 °C for a period of 20 h. Then it was mixed with γ-Al_2O_3 and $BaCO_3$ in an agate mortar in an argon environment. This was followed by annealing in a hydrogen atmosphere at a temperature of 800 °C for 20 h to get the support in final form. $Al(OH)_3$ and $BaCO_3$ underwent solid-state reaction to form $BaAl_2O_4$. They were mixed thoroughly in an agate mortar followed by calcination at a temperature of 1000 °C for 20 h in air. For loading Ru on the support, chemical vapour deposition method was used. For Co loading, $Co_2(CO)_8$ along with the support was ground in an agate mortar in an Argon environment followed by heating in a quartz tube at 200 °C for 2 h in a mixture of N_2 and H_2 gases. Finally, the mixture was thermally treated at 500 °C for 1.5 h to obtain the cobalt-loaded catalyst.

The modified Pechini method was used for the synthesis of $C_{12}A_7{:}O^{2-}$.[110] The modified Pechini method is based on the sol–gel and polymeric precursor approach. Metal ions are chelated using citric acid and EDTA to form a stable complex, which ensures uniform mixing at the molecular level. Upon heating, polymerization occurs, creating a gel that prevents phase separation. Subsequent calcination decomposes organics, leading to controlled crystallization of the desired oxide phase with high purity and homogeneity. Calcium and aluminium nitrates were dissolved in EDTA and citric acid solution with an EDTA/citric acid/metal ion ratio of 1.5/1.5/1. This was followed by the addition of ammonium hydroxide in the slurry till a clear solution was formed. Water was evaporated off this solution to obtain a claybank gel which was placed in an oven and dried at

a temperature of 150 °C for 48 h period to yield charcoal-like powder. Mayenite in its pure form ($C_{12}A_7$) was obtained by calcination of this powder at a temperature of 1200 °C for 10 h. $C_{12}A_7$:e^- electride was obtained by an aluminothermic method.

Aluminum acts as a strong reductant and thus donates electrons to reduce CaO and Al_2O_3, resulting in the formation of metallic aluminum oxide by-products. During this process, oxygen atoms are extracted from the lattice which creates anionic vacancies that trap free electrons, stabilizing them within the $C_{12}A_7$ framework. This results in the formation of an electride, where these trapped electrons act as anions, giving the material its unique electronic properties. In this method, CaO, Al_2O_3, and Al powders were mixed in an agate mortar followed by calcination in a tubular furnace at a temperature of 1200 °C for 8 h in an argon atmosphere. Ru was loaded onto these supports by the chemical vapour deposition method to obtain the catalyst in its final form.

Arc-melting was primarily used to synthesize LaRuSi[109] and CaRuSi electrides, promoting uniformity *via* repeated melting and annealing. LaRuSi was synthesized by arc melting La, Ru, and Si (1 : 1 : 1) under an Ar atmosphere, with repeated melting for homogeneity. The ingot was annealed for two weeks and then ground under an Ar atmosphere for use as a catalyst.

CaRuSi was prepared *via* a solid-state route. The RuSi precursor was first synthesized by arc melting, then mixed with Ca ingots (5% excess) and sealed in a Ta crucible inside an Ar-filled quartz tube. Heat treatment was carried out at 850 °C for 10 h, followed by 800 °C for 2 days to obtain the pure phase.

In 2012, Kitano *et al.* reported the activity of a stable electride, $C_{12}A_7$:e^-, synthesized by a solid-state reaction that efficiently donates electrons to the Ru catalyst. Ru/$C_{12}A_7$:e^- displayed substantially superior activity than that of Ru–Cs/MgO and Ru–Ba/AC.[111] For instance, the reported turnover frequency (TOF) for Ru/$C_{12}A_7$:e^- at 1.0 MPa was 0.98 s^{-1}, which is significantly higher than those of Ru–Ba/AC and Ru–Cs/MgO

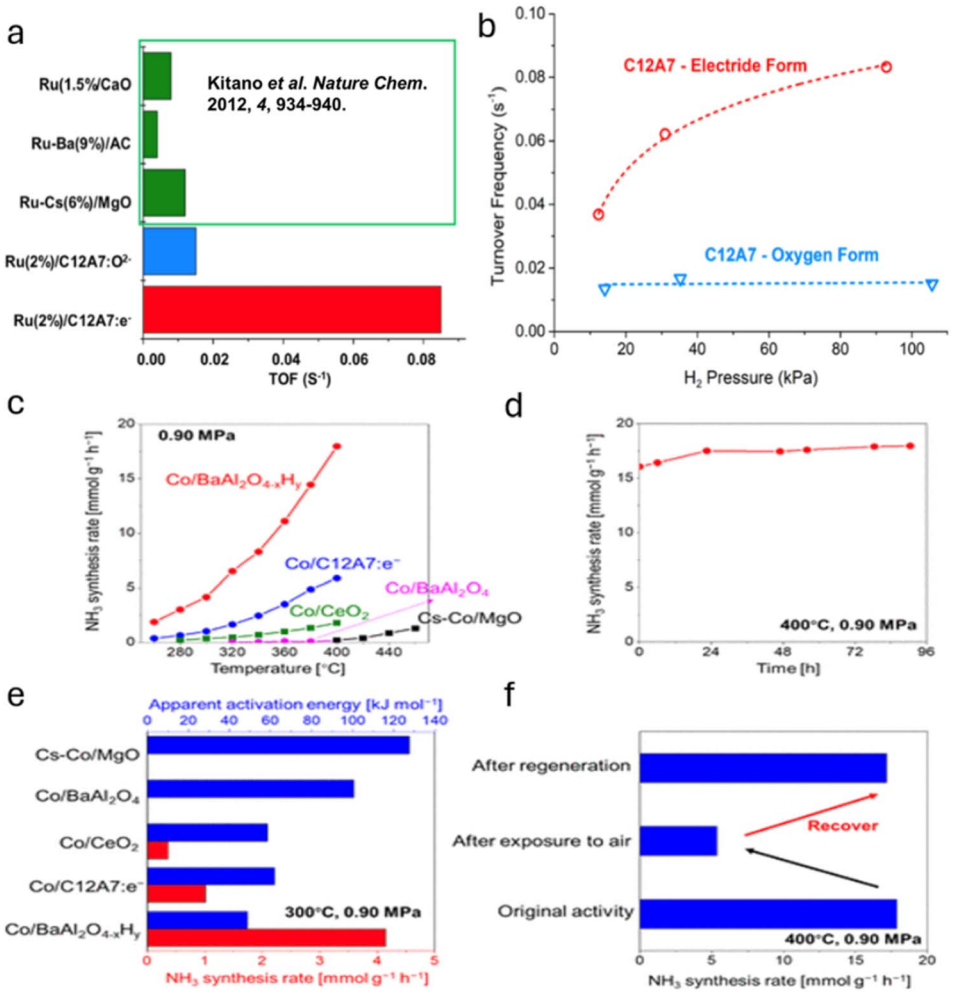

Fig. 15 (a) Comparative turnover frequency (TOF) of ammonia synthesis at 400 °C in 0.1 MPa (3/1 = H_2/N_2). (b) Variation of TOF with hydrogen pressure over the electride and oxygen forms of Ru/$C_{12}A_7$ catalysts. Adapted with permission from ref. 110. Copyright 2020, the American Chemical Society. (c) Performance of the Co/$BaAl_2O_{4-x}H_y$ catalyst for ammonia synthesis, and comparison of different Co-based catalysts at different temperatures under 0.90 MPa pressure. (d) Stability analysis of Co (4.7 wt%)/$BaAl_2O_{4-x}H_y$ at 400 °C and 0.90 MPa over time. (e) Ammonia synthesis rates and activation energies for various Co catalysts at 300 °C and 0.90 MPa. (f) Illustration of Co/$BaAl_2O_{4-x}H_y$'s activity changes after exposure to air and improvement after treatment at 600 °C in H_2 flow for 6 hours. All tests were performed at a flow rate of 36 000 mL g^{-1} h^{-1}. Adapted with permission from ref. 108. Copyright 2023, the American Chemical Society.

(0.05–0.28 s^{-1}), respectively, at elevated pressures (2.0–6.3 MPa).[111–114] Such results also demonstrate that the catalytic activity is limited for conventional oxide-supported Ru catalysts, because the dissociative adsorption of hydrogen on Ru hinders the cleavage of nitrogen molecules at elevated pressures. To get an insight into the mechanistic details, isotopic FT-IR spectra using $^{14}N_2/^{15}N_2$ were recorded. The article concludes that electrons trapped in $C_{12}A_7$:e^- transferred to Ru metal, which considerably lowered the work function of Ru by increasing the Fermi level. Consequently, back donation from Ru with excess electron density to the π*-antibonding orbital of nitrogen increased, which weakened the N≡N bond of adsorbed nitrogen molecules. The surface adsorbed dissociated hydrogen molecules spilled over to $C_{12}A_7$:e^- and were incorporated into the cages as H^- ions, and prevented hydrogen poisoning of the Ru surface. Further, the activated nitrogen species combine with H^- ions (inside the $C_{12}A_7$ nanocages) to form ammonia.

Within the literature, it is established that electron-rich supports with defects consisting of electrons lower the work function and remarkably enhance the catalytic ammonia synthesis. However, the mechanism of such promotional effect and the exact reason for the suppression of hydrogen poisoning in the presence of electride-supported Ru catalysts were unclear. To address this issue, Kammert *et al.* examined the hydride species in the $C_{12}A_7$:e^- electride during ammonia production using techniques such as neutron diffraction and inelastic neutron scattering.[110] With a Ru loading of 2 wt%, the ammonia synthesis rate was 1.5 mmol g^{-1} h^{-1} at 360 °C and the apparent activation energy was 72 kJ mol^{-1}. The comparative TOF values of previously published reports and different forms of $C_{12}A_7$ are illustrated in Fig. 15a and b.

The orders of the reaction with respect to N_2 and H_2 were 0.7 and 0.3, respectively. Further, this study found that the confined hydrides are stable and not readily exchanged in the $C_{12}A_7$:e^- framework, contrary to the previous reports. However, these hydride species could exchange with the surface species which limits their kinetic role in the production and mechanism of ammonia production. Therefore, this study concludes that hydrogen species adsorbed over the Ru surface predominantly contribute to ammonia synthesis. Importantly, the coverage of reactive intermediates and nature of adsorbates on the Ru surface could be the reason that hydrogen poisoning was suppressed during ammonia production by the electride-supported Ru.

Jiang *et al.* reported that $BaAl_2O_{4-x}H_y$, a novel oxyhydride electride with a tridymite-like structure, significantly enhances ammonia synthesis over Co catalysts, achieving 500 mmol g_{Co}^{-1} h^{-1} at 340 °C and 0.90 MPa with a low activation energy of 49.6 kJ mol^{-1}.[108] Its structure contains interstitial cage sites that host anionic electrons, with low work functions (1.7–2.6 eV) that strongly donate electrons to Co, thus accelerating N_2 reduction into ammonia using lattice H^- ions. The stability of $BaAl_2O_{4-x}H_y$ and its resistance to oxidation give it robust reusability, making it superior to traditional hydride-based catalysts. Fig. 15c–f show performance of the Co/$BaAl_2O_{4-x}H_y$ catalyst for ammonia synthesis and compare different Co-based catalysts at different temperatures under 0.90 MPa pressure.

In an interesting article by Hattori *et al.*, a novel approach to produce ammonia at low temperatures (50 °C) using a stable electron-donating catalyst, CaFH, was reported.[25] This work

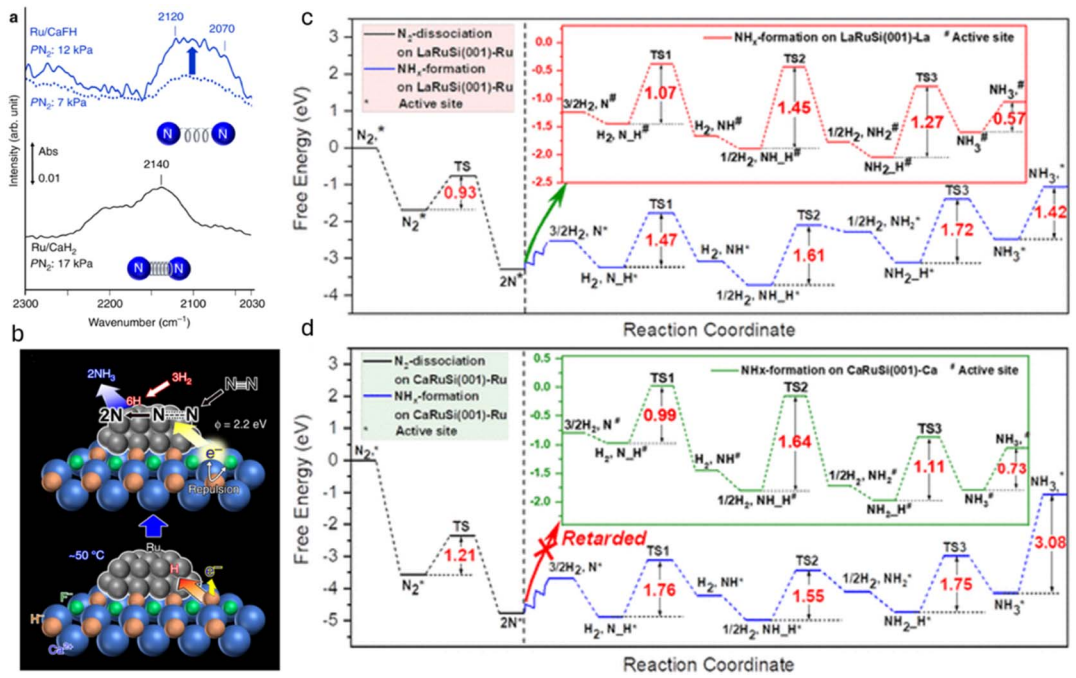

Fig. 16 (a) FT-IR spectra for nitrogen adsorption on Ru/CaFH and Ru/CaH_2 after ammonia generation at 340 °C and subsequent cooling to 20 °C. (b) Plausible reaction mechanism. Adapted with permission from ref. 25. Copyright 2020, Springer Nature. (c) Energy profiles for ammonia synthesis calculated for LaRuSi and (d) CaRuSi surfaces. Adapted with permission from ref. 109. Copyright 2022, the American Chemical Society.

Table 7 Oxide-based catalysts

S. no.	Catalyst	Temp. (°C)	Pressure (MPa)	Rate (mmol g^{-1} h^{-1})	Activation energy (kJ mol^{-1})	Metal%	WHSV	N_2 order	H_2 order	NH_3 order	Surface area (m^2 g^{-1})	Turnover frequency (TOF)	Catalyst synthesis method	Ref.
1	Ru/La_2O_3	400	1	32.14	118	5% Ru	24 000	1.00	−0.46	−0.57	61.1	—	Deposition–precipitation method	115
2	$Co/MgO–Nd_2O_3$ (Mg/Nd molar ratio – 2 : 1)	400	6.3	23.4	58.9	10% Co	140 000	—	—	—	22.9	3.9×10^2	Co-precipitation method	116
3	$Co/MgO–Nd_2O_3$ (Mg/Nd molar ratio – 4 : 1)	400	6.3	29.9	55.3	10% Co	140 000	—	—	—	29.3	3.8×10^2	Co-precipitation method	116
4	$Co/MgO–Nd_2O_3$ (Mg/Nd molar ratio – 7 : 1)	400	6.3	33.2	53.9	10% Co	140 000	—	—	—	37.8	3.6×10^2	Co-precipitation method	116
5	$Co/MgO–Nd_2O_3$ (Mg/Nd molar ratio – 10 : 1)	400	6.3	39.3	53.7	10% Co	140 000	—	—	—	49.5	3.5×10^2	Co-precipitation method	116
6	$Co/MgO–Nd_2O_3$ (Mg/Nd molar ratio – 12 : 1)	400	6.3	35.5	54.6	10% Co	140 000	—	—	—	46.9	3.6×10^2	Co-precipitation method	116
7	Ru/Al_2O_3	400	1	1.432	82	3% Ru	24 000	1.0	−0.1	−1.1	169	2.6×10^{-3}	Co-precipitation method	117
8	$Ce–Ru/Al_2O_3$ (1 : 1 molar ratio of Ce/Ru)	400	1	14.352	75	3% Ru, 4.1% Ce	24 000	1.0	0.8	−0.2	169	0.029	Co-precipitation method	117
9	Ru/CeO_2 (cycle)	200	0.1	0.65	60	5% Ru	36 000	—	—	—	—	—	Impregnation method	118
10	Ru/CeO_2 (steady state)	200	0.1	0.12	60	5% Ru	36 000	—	—	—	—	—	Impregnation method	118
11	Ru/CeO_2 (cycle)	300	0.1	1.87	60	5% Ru	36 000	—	—	—	—	—	Impregnation method	118
12	Ru/CeO_2 (steady state)	300	0.1	2.23	60	5% Ru	36 000	—	—	—	—	—	Impregnation method	118
13	Ru/CeO_2-w	400	1	22.62	51.5	3% Ru	36 000	0.96	1.01	−0.75	38	21.8×10^{-3}	Precipitation method	119
14	Ru/CeO_2-e	400	1	4.582	58.3	3% Ru	36 000	0.80	0.43	−0.66	49	4.4×10^{-3}	Precipitation method	119
15	Ru/MgO + BaO/MgO	400	1	1.25	93.4	2.5% Ru, 2.5% Ba	80 000	0.92	−0.40	−0.32	223	—	Hydrothermal synthesis method	120
16	Ba–Ru/MgO-20	400	1	24.72	83.9	4.8% Ru, 4.9% Ba	80 000	0.86	0.35	−0.78	191	—	Hydrothermal impregnation-reduction method	120
17	Ba–Ru/MgO-10	400	1	28.2	75.2	4.7% Ru, 4.8% Ba	80 000	0.86	0.43	−0.75	189	—	Hydrothermal impregnation–reduction method	120
18	Ba–Ru/MgO-2	400	1	38.4	69.7	4.8% Ru, 4.8% Ba	80 000	0.86	0.52	−0.82	195	—	Hydrothermal impregnation–reduction method	120
19	Ba–Ru/MgO–2H	400	1	45.36	64.3	4.8% Ru, 4.8% Ba	80 000	0.84	0.59	−0.78	185	—	Hydrothermal impregnation–reduction method	120
20	$Co(10)/Nd_2O_3$	470	6.3	59.41	—	9.9% Co, 77.2% Nd	—	—	—	—	27.3	0.085	Deposition–precipitation method	121
21	$Co(19)/Nd_2O_3$	470	6.3	81.76	—	19.4% Co, 65.6% Nd	—	—	—	—	32.0	0.130	Deposition–precipitation method	121
22	$Co(31)/Nd_2O_3$	470	6.3	74.70	—	30.8% Co, 59.6% Nd	—	—	—	—	36.5	0.115	Deposition–precipitation method	121

Table 7 (*Contd.*)

S. no.	Catalyst	Temp. (°C)	Pressure (MPa)	Rate (mmol g^{-1} h^{-1})	Activation energy (kJ mol^{-1})	Metal%	WHSV	N_2 order	H_2 order	NH_3 order	Surface area (m^2 g^{-1})	Turnover frequency (TOF)	Catalyst synthesis method	Ref.
23	Co(39)/Nd_2O_3	470	6.3	83.52	—	38.6% Co, 46.8% Nd	—	—	—	—	39.6	0.110	Deposition–precipitation method	121
24	Co(50)/Nd_2O_3	470	6.3	107.06	—	49.6% Co, 39.5% Nd	—	—	—	—	41.8	0.135	Deposition–precipitation method	121
25	Ru/MgO–CeO_2 Ce/Mg = 1	400	0.1	3000 ppm	41	3% Ru	—	1.21	0.36	−0.65	64.44	—	Co-precipitation method	122
26	Ru/CeO_2	400	0.1	2850 ppm	38	3% Ru	—	1.14	0.55	−0.67	102.77	—	Precipitation method	122
27	Ru/MgO	450	0.1	1480 ppm	115	1% Ru	—	1.35	−1.41	−0.37	25	—	Precipitation method	123
28	Ce/Mg = 0.01	450	0.1	1890 ppm	78	1% Ru	—	1.07	−0.91	−0.08	58	—	Impregnation–precipitation method	123
29	Ce/Mg = 0.03	400	0.1	1942 ppm	60	1% Ru	—	0.74	−0.37	−0.08	108	—	Impregnation–precipitation method	123
30	Ce/Mg = 0.05	400	0.1	2192 ppm	53	1% Ru	—	0.81	−0.34	−0.17	102	—	Impregnation–precipitation method	123
31	Ce/Mg = 0.1	400	0.1	2492 ppm	44	1% Ru	—	0.84	0.19	−0.35	116	—	Impregnation–precipitation method	123
32	Ce/Mg = 0.3	400	0.1	2458 ppm	44	1% Ru	—	0.89	0.15	−0.23	116	—	Impregnation–precipitation method	123
33	Ce/Mg = 0.5	450	0.1	1848 ppm	62	1% Ru	—	0.64	−0.08	−0.73	102	—	Impregnation–precipitation method	123
34	Ru/CeO_2	400	0.1	2014 ppm	58	1% Ru	—	0.96	0.01	−0.35	95	—	Precipitation method	123
35	3 Ru/Y_2O_3-m	400	1	2.5	108	3% Ru	24 000	—	—	—	44.9	5×10^{-3}	Hydrothermal and milling method	124
36	3 Ru/Y_2O_3-p	400	1	9	99	3% Ru	24 000	—	—	—	44.8	0.014	Hydrothermal and milling method	124
37	5 Ru/Y_2O_3-m	400	1	4.378	104	5% Ru	24 000	1.1	−1.3	−0.7	45.8	5×10^{-3}	Hydrothermal and milling method	124
38	5 Ru/Y_2O_3-p	400	1	21.12	97	5% Ru	24 000	1.1	−0.9	−0.5	47.6	0.019	Hydrothermal and milling method	124
39	Ru/LCO	400	1	10.8	—	5% Ru	54 000	—	—	—	53	—	Co-precipitation method	125
40	Ru/4Ba/LCO	400	1	23.8	—	5% Ru, 4% Ba	54 000	—	—	—	38	—	Co-precipitation–impregnation method	125
41	Ru/4Cs/LCO	400	1	27.1	—	5% Ru, 4% Cs	54 000	—	—	—	11	—	Co-precipitation–impregnation method	125
42	Ru/4K/LCO	400	1	35.9	—	5% Ru, 4% K	54 000	—	—	—	17	—	Co-precipitation–impregnation method	125
43	Ru/4Li/LCO	400	1	6.6	—	5% Ru, 4% Li	54 000	—	—	—	6	—	Co-precipitation–impregnation method	125
44	Ru/Sm_2O_3	400	1	13.596	—	5% Ru	24 000	1.08	−0.72	−0.92	54.0	—	Hydrothermal, deposition–precipitation method	126

Table 7 (*Contd.*)

S. no.	Catalyst	Temp. (°C)	Pressure (MPa)	Rate (mmol g^{-1} h^{-1})	Activation energy (kJ mol^{-1})	Metal%	WHSV	N_2 order	H_2 order	NH_3 order	Surface area (m^2 g^{-1})	Turnover frequency (TOF)	Catalyst synthesis method	Ref.
45	Ru/Sm_2O_3 (activated)	400	1	32.214	—	5% Ru	24 000	1.08	−0.72	−0.92	54.0	—	Hydrothermal, deposition–precipitation method	126
46	Ru/CeO_2	400	1	4	—	2.1% Ru	36 000	0.81	−0.57	−1.29	71	3.9×10^{-3}	Hydrothermal method	96
47	Ru/CeO_2 + Ru/TiO_2	400	1	4.120	—	—	36 000	—	—	—	—	3.9×10^{-3}	Hydrothermal method	96
48	$Ru/Cs^+(0.35)/CeO_2$	350	0.1	4.62	—	2% Ru	36 000	0.6	0.2	−0.8	23.4	34.5×10^{-3}	Impregnation method	127
49	$Cs^+(0.35)/Ru/CeO_2$	350	0.1	2.11	—	2% Ru	36 000	0.8	−0.3	−0.9	—	20.9×10^{-3}	Impregnation method	127
50	Cs/Ru/MgO	350	0.1	1.01	—	2% Ru	36 000	0.7	−0.7	0	—	—	Impregnation method	127
51	$Ru/Cs^+(0.35)/CeO_2$	350	0.1	2.69	—	1% Ru	36 000	—	—	—	—	15.4×10^{-3}	Impregnation method	127
52	$Ru/Cs^+(0.35)/CeO_2$	350	0.1	4.27	—	5% Ru	36 000	—	—	—	—	46.2×10^{-3}	Impregnation method	127
53	$Ru/Cs^+(0.2)/CeO_2$	350	0.1	0.96	—	2% Ru	36 000	—	—	—	65.5	7.1×10^{-3}	Impregnation method	127
54	Ru/CeO_2	350	0.1	0.31	—	2% Ru	36 000	—	—	—	112.3	0.69×10^{-3}	Impregnation method	127
55	$Ru/Cs^+(0.6)/CeO_2$	350	0.1	0.94	—	2% Ru	36 000	—	—	—	3.7	22.4×10^{-3}	Impregnation method	127
56	Mo/CeO_2	400	1	0.438	60	Mo : Ce mass ratio = 0.35	36 000	0.68	0.14	−0.7	8		Co-precipitation method	128
57	Co/La_2O_3	350	1	2.8	—	20% Co	72 000	0.97	0.32	−0.51	25.8	0.051	Precipitation–impregnation method	129
58	$Co/Ba/La_2O_3$ 500	350	1	2.4	73.1	20% Co	72 000	—	—	—	37.5	0.019	Precipitation–impregnation method	129
59	$Co/Ba/La_2O_3$ 700	350	1	19.3	45.7	20% Co	72 000	0.85	0.43	−0.17	24.9	0.223	Precipitation–impregnation method	129
60	$Co/Ba/La_2O_3$ 800	350	1	17.1	—	20% Co	72 000	—	—	—	10.1	0.304	Precipitation–impregnation method	129
61	$1.4Ru/CeO_2$	400	1	3.8[a]	72	1.4% Ru	72 000	0.62	0.27	−0.39	92	2.028[a]	Solvothermal method	130
62	$2.8Ru/CeO_2$	400	1	10.4	64	2.8% Ru	72 000	0.58	0.33	−0.47	103	2.78[a]	Solvothermal method	130
63	$5.3Ru/CeO_2$	400	1	5[a]	87	5.3% Ru	72 000	1.30	−0.35	−0.64	64	0.56[a]	Solvothermal method	130
64	Ru/ZrO_2	400	1	5.44	125 ± 4	1.92% Ru	60 000	0.69	−0.58	−0.73	29	8×10^{-3}	Precipitation-milling method	65
65	$Ru(2)/Sm_2O_3$	400	1	13.7[a]	106.3	2% Ru	24 000	—	—	—	41.0	0.0247	Hydrothermal, ion-adsorption method	131
66	$Ru(3)/Sm_2O_3$	400	1	17.5[a]	109.9	3% Ru	24 000	—	—	—	49.6	0.0221	Hydrothermal, ion-adsorption method	131
67	$Ru(4)/Sm_2O_3$	400	1	22.570	104.8	4% Ru	24 000	—	—	—	54.3	0.0229	Hydrothermal, ion-adsorption method	131
68	$Ru(5)/Sm_2O_3$	400	1	23.040	105.1	5% Ru	24 000	—	—	—	56.2	0.0135	Hydrothermal, ion-adsorption method	131
69	Ru/Pr_2O_3	400	1	—	—	—	—	1.11	0.02	−0.55	24	0.24	Precipitation–impregnation method	132
70	Ru/CeO_2	400	1	—	—	—	—	0.85	0	−0.24	34	0.09	Precipitation–impregnation method	132
71	Ru/La_2O_3	400	1	—	—	—	—	1.10	−0.03	−0.57	22	0.24	Precipitation–impregnation method	132
72	Ru/Nd_2O_3	400	1	—	—	—	—	1.25	−0.29	−0.61	22	0.09	Precipitation–impregnation method	132
73	Ru/Sm_2O_3	400	1	—	—	—	—	1.11	−0.11	−0.47	17	0.08	Precipitation–impregnation method	132

Table 7 (*Contd.*)

S. no.	Catalyst	Temp. (°C)	Pressure (MPa)	Rate (mmol g^{-1} h^{-1})	Activation energy (kJ mol^{-1})	Metal%	WHSV	N_2 order	H_2 order	NH_3 order	Surface area (m^2 g^{-1})	Turnover frequency (TOF)	Catalyst synthesis method	Ref.
74	Ru/Gd_2O_3	400	1	—	—	—	—	1.12	0	−0.23	12	0.05	Precipitation–impregnation method	132
75	Ru/Yb_2O_3	400	1	—	—	—	—	—	—	—	4	—	Precipitation–impregnation method	132
76	Ru/Ho_2O_3	400	1	—	—	—	—	—	—	—	3	—	Precipitation–impregnation method	132
77	Ru/Er_2O_3	400	1	—	—	—	—	—	—	—	4	—	Precipitation–impregnation method	132
78	Ru/Tb_2O_3	400	1	—	—	—	—	—	—	—	3	—	Precipitation–impregnation method	132
79	Cs–Co/MgO	300	1	0.48	—	3.20% Co	60 000	—	—	—		0.24×10^{-3}	Impregnation method	68
80	Co(10)/Mg–La	400	6.3	16.0	62	10% Co	140 000	—	—	—	25	0.025	Co-precipitation, impregnation method	133
81	Co(20)/Mg–La	400	6.3	24.2	58	20% Co	140 000	—	—	—	25	0.023	Co-precipitation, impregnation method	133
82	Co(30)/Mg–La	400	6.3	31.8	57	30% Co	140 000	—	—	—	30	0.025	Co-precipitation, impregnation method	133
83	Co(40)/Mg–La	400	6.3	40.3	59	40% Co	140 000	—	—	—	33	0.025	Co-precipitation, impregnation method	133
84	Co(50)/Mg–La	400	6.3	38.2	60	50% Co	140 000	—	—	—	33	0.021	Co-precipitation, impregnation method	133
85	Ru/CeO_2	400	1	16.867	75	2.7% Ru	36 000	0.48	0.66		56	16.2×10^{-3}	Calcination–impregnation method	134
86	Mo/CeO_2	400	1	0.438	60	Mo : Ce mass ratio = 0.35	36 000	0.68	0.14	−0.7	8	—	Co-precipitation/impregnation/physical mixing	128
87	Ru/CeO_2–H	400	1	4.064	60	1% Ru	36 000	1.0	−0.53	−0.72	86	0.058	Hydrothermal, reduction in hydrogen	135
88	Ru/CeO_2–C250H	400	1	8.033	72	1% Ru	36 000	1.2	0.3	−0.75	82	0.123	Hydrothermal, reduction, CO treatment	135
89	Ru/CeO_2–C500H	400	1	9.244	67	1% Ru	36 000	1.3	0.36	−0.79	81	0.143	Hydrothermal, reduction, CO treatment	135
90	Ru/BTO	400	0.1	1.506	69.4	2% Ru	36 000	1.38	−0.47	−0.27	—	5.3×10^{-3}	Hydrothermal method	136
91	Ru/CaBTO600	400	0.1	4.944	72.7	2.2% Ru	36 000	1.07	0.33	−0.32	—	0.0231	Hydrothermal, thermal modification with CaH_2	136

[a] Exact rate of ammonia production is not given in the source paper; listed values are closest approximates obtained from the plot in the source paper.

Table 8 Catalysts with perovskite structures

S. no.	Catalyst	Temp. (°C)	Pressure (MPa)	Rate (mmol g^{-1} h^{-1})	Activation energy (kJ mol^{-1})	Metal%	WHSV	N_2 order	H_2 order	NH_3 order	Surface area (m^2 g^{-1})	Turnover frequency (TOF)	Catalyst synthesis method	Ref.
1	CoCe-0.05	400	5	2.35	196		18 000	—	—	—	18.4 ± 0.06	—	Co-precipitation method	137
2	5Ba/CoCe-0.01	400	5	2.94	99	5% Ba	18 000	—	—	—	3.05 ± 0.10	—	Co-precipitation–impregnation method	137
3	5Ba/CoCe-0.05	400	5	14.94	57	5% Ba	18 000	—	—	—	7.61 ± 0.13	—	Co-precipitation–impregnation method	137
4	5Ba/CoCe-0.20	400	5	5.29	113	5% Ba	18 000	—	—	—	13.9 ± 0.20	—	Co-precipitation–impregnation method	137
5	5Ba/CoCe-0.50	400	5	3.94	103	5% Ba	18 000	—	—	—	15.3 ± 0.23	—	Co-precipitation–impregnation method	137
6	Ru/BNO	400	0.1	—	—	—	36 000	1.01	−0.27	−0.62	18	—	Hydrothermal, physical grinding method	138
7	Ru/0.20CaBNO	400	0.1	4.012	—	4% Ru	36 000	0.89	1.12	−0.54	12	6.4×10^{-3}	Hydrothermal, physical grinding method	138
8	3Cs–Ru/0.20CaBNO	400	0.1	5.369	—	4% Ru	36 000	0.79	1.24	−0.89	9	9.8×10^{-3}	Hydrothermal, physical grinding method	138
9	$Ru_{1.1}/BaCeO_3$	400	1	19.4	72	0.44% Ru	60 000	0.72	0.13	−0.77	4.5	0.124	Sol–gel method	139
10	$Ru_{1.5}/BaCeO_3$	400	1	17.2	93	0.42% Ru	60 000	—	—	—	4.9	0.115	Sol–gel method	139
11	$Ru_{2.0}/BaCeO_3$	400	1	5.5	112	0.44% Ru	60 000	—	—	—	3.6	0.036	Sol–gel method	139
12	$Ru_{3.0}/BaCeO_3$	400	1	3.4	127	0.46% Ru	60 000	1.07	−1.20	−2.60	4.0	0.021	Sol–gel method	139
13	$Ru/BaCe_{0.9}Y_{0.1}O_{3-\delta}$ (Ru is exsolved)	450	0.1	3.68	160	0.95% Ru	360 000	—	—	—	3.08	0.19962	Glycine nitrate process (GNP)	140
14	$Ru/BaCe_{0.9}Y_{0.1}O_{3-\delta}$ (Ru is impregnated)	450	0.1	0.45	5.28	0.95% Ru	144 000	—	—	—	3.33	3.5×10^{-3}	Glycine nitrate process (GNP)	140

used appropriate amounts of CaF_2 and CaH_2 and heated to 550 °C under argon flow for 20 h, resulting in a solid solution of cubic CaFH catalyst. $Ru(acac)_3$, a precursor, was heated under hydrogen flow at high temperature to synthesize a Ru/CaFH catalyst with a loading of 12 wt% Ru. The as-prepared Ru/CaFH catalyst produced ammonia at rates of 50, 75, 120, and 190 μmol g^{-1} h^{-1} at 50, 75, 100, and 125 °C, respectively, with an extremely small activation energy of 20 kJ mol^{-1}, calculated in the range of 50–150 °C. The FTIR spectra for N_2 adsorption over this catalyst is shown in Fig. 16a. At room temperature, stretching bands of adsorbed nitrogen on Ru/CaH_2 at 2100–2250 cm^{-1} were observed, which are lower than that of nitrogen gas (2744 cm^{-1}). This result implies that the electron donation from the catalyst to the π*-antibonding orbitals of adsorbed nitrogen *via* Ru d-orbitals facilitates the dissociation of nitrogen bond. Comparing Ru/CaH_2, a large shift in the wavenumber was observed for Ru/CaFH, which could lead to high activity even at room temperature. In the end, the findings from H_2-TPD and DFT experiments further help to corroborate that nitrogen molecules were readily dissociated into N adatoms, which combine with H from CaFH to generate ammonia at room temperature. This mechanism is illustrated in Fig. 16b. Herein, the resulting CaFH acts as a surface electride with a lower work function value ($\phi = 2.2$ eV) than that of CaH_2 ($\phi = 2.7$ eV).

In another work, Gong *et al.* demonstrated that the LaRuSi electride enhances NH_3 synthesis by disrupting scaling relations through two key mechanisms: it achieves low N_2 activation energy on a Ru-terminated surface without overly strong nitrogen adsorption, and the La site facilitates NH_x formation, further lowering reaction barriers.[109] Energy profiles of NH_3 synthesis on LaRuSi and CaRuSi surfaces are shown in Fig. 16c and d, respectively. The activation energies (E_a) for NH, NH_2, and NH_3 formation on LaRuSi are 1.07, 1.45, and 1.27 eV, respectively—significantly lower than on LaRuSi(001)–Ru. NH_3 desorption from LaRuSi(001)–La requires only 0.57 eV, breaking traditional Ru catalyst scaling relations, with NH_2 formation as the rate-determining step (RDS). For CaRuSi, NH_x formation steps are more favorable on Ca-terminated surfaces compared to Ru-terminated, with NH_3 desorbing more easily from CaRuSi(001)–Ca. The NH_2 formation step is the RDS for NH_3 synthesis on both LaRuSi and CaRuSi.

Despite their remarkable activity, electride catalysts face several challenges. One of the primary concerns is the limited activity with certain transition metals, such as ruthenium, which restricts their scalability and cost-effectiveness. The reliance on specific metals for optimal performance makes these catalysts less versatile in industrial applications. Additionally, maintaining the stability of electrides under reaction conditions can be challenging due to the high reactivity of the trapped electrons, which may degrade over time, especially under harsh reaction environments. The high sensitivity of electrides to moisture and oxygen can also further decrease their performance. To address these challenges, future research should focus on identifying alternative transition metals that can work effectively with electrides to expand their applicability. Strategies to stabilize the electron density in electrides, such as doping with stabilizing elements or optimizing the crystal structure, could enhance their

longevity and resistance to degradation. Furthermore, the development of electride systems with greater stability in the presence of moisture and oxygen would increase their practical feasibility for industrial-scale ammonia synthesis.

3.5 Oxide-based catalysts

Another class of catalysts which hold the potential for ammonia synthesis under mild conditions are the oxide-based catalysts. Mixed metal oxides or perovskite-structure-based oxide catalysts have also demonstrated significant activity for ammonia synthesis (see Tables 7 and 8). Oxide catalysts are widely recognized for their basic nature, high stability, and strong metal–support interactions, which play a critical role in enhancing the catalytic performance for ammonia synthesis. Oxygen vacancies intrinsic to oxide supports act as active sites for N_2 activation by facilitating the adsorption and dissociation of nitrogen molecules. The strong metal–support interactions not only stabilize the active metal species but also enhance electron transfer between the support and the metal, further improving catalytic activity. In the case of mixed oxides, the synergistic interplay between multiple metal components leads to an enriched concentration of oxygen vacancies, amplifying the catalyst's activity. As is known, the enhanced electron donation properties and active site availability facilitate the activation of nitrogen, and also, the hydrogenation process. Therefore, oxide-based catalysts are of particular interest for ammonia synthesis under mild conditions.

Oxide-supported catalysts based on stabilization and tunability of active sites favor effective nitrogen activation in ammonia synthesis. Generally, these catalysts are transition metal oxides (for example, CeO_2 and TiO_2) or perovskite-type oxides, and their improvement of catalytic performance occurs through the modification of metal–support interactions and electronic properties. Various synthesis strategies were employed to modify the properties of oxide-based catalysts.

The precipitation method allowed the regulation of nucleation during the synthesis of $La(OH)_3$,[115] which was followed by hydrothermal treatment to enhance crystallinity followed by a deposition–precipitation method for uniform dispersion of Ru within La_2O_3. During precipitation, $La(OH)_3$ nuclei form as KOH increases the pH, which leads to the controlled growth of hydroxide particles. Hydrothermal treatment enhances crystallinity, while deposition–precipitation ensures uniform Ru

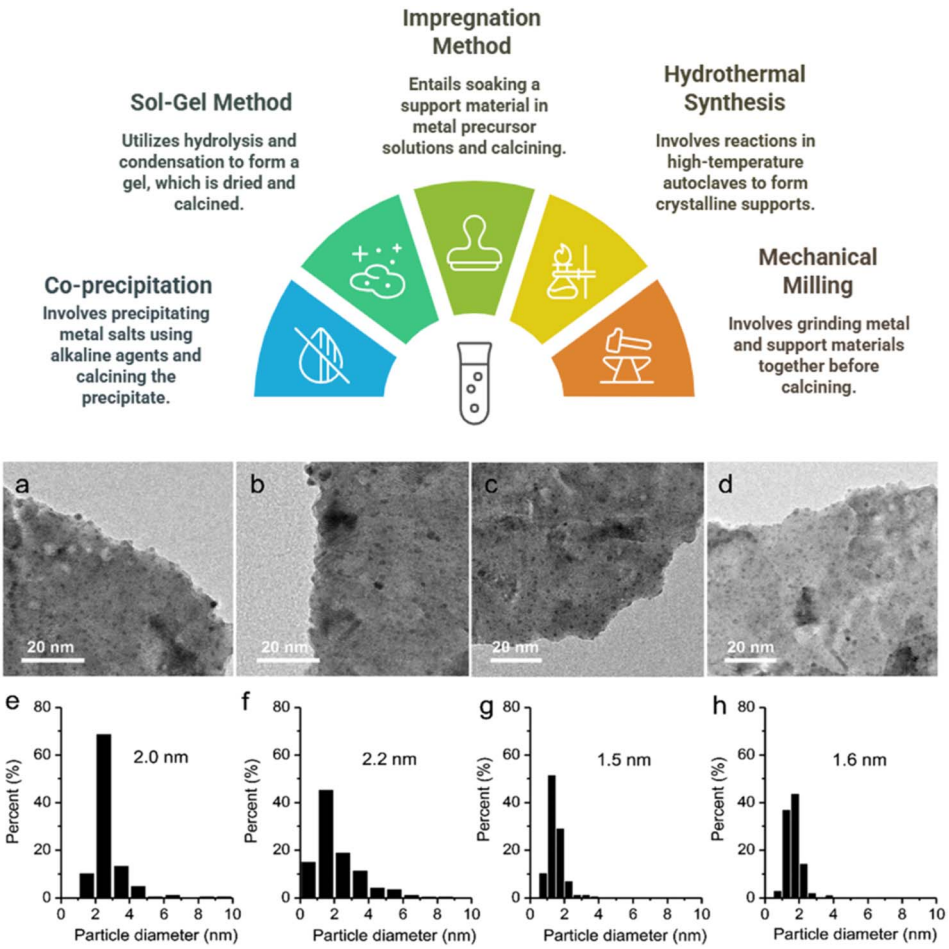

Fig. 17 Various synthesis strategies for oxide-based catalysts. TEM images along with Ru particle size distributions for 3% Ru/Y_2O_3-m (a and e), 5% Ru/Y_2O_3-m (b and f), 3% Ru/Y_2O_3-p (c and g), and 5% Ru/Y_2O_3-p (d and h) synthesized *via* a combination of hydrothermal, milling and reduction methods. Adapted with permission from ref. 124. Copyright 2023, the Royal Society of Chemistry.

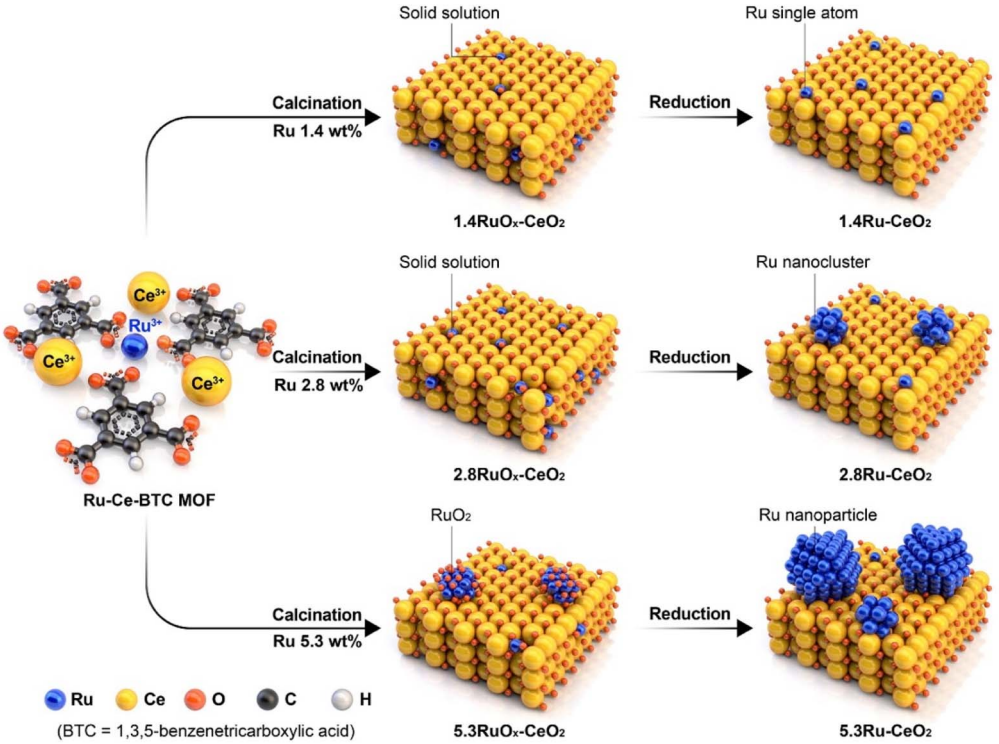

Fig. 18 Method of synthesis of Ru–CeO_2 catalysts. Here Ru–Ce–BTC shows the raw form, which is followed by calcination to form RuO_x–CeO_2 and then Ru–CeO_2 *via* the reduction method. Adapted with permission from ref. 130. Copyright 2022, Elsevier.

dispersion by controlled nucleation and growth of Ru species on La_2O_3 using urea as a precipitating agent. Lanthanum nitrate was dissolved in DI water to which 20% KOH was added till the pH became 14 and a white precipitate was formed. The mixture was continuously stirred for 30 minutes and then transferred to a Teflon-lined stainless-steel autoclave in which the mixture was made to undergo hydrothermal treatment at a temperature of 180 °C for 12 h. Finally, the mixture was washed several times with DI water to remove any remaining ions and then dried at a temperature of 80 °C for 12 h. Ru was loaded on this support by a deposition–precipitation method. $La(OH)_3$ was added to an aqueous solution of $RuNO(NO_3)_3$ followed by addition of urea in a Ru-to-urea molar ratio of 1/200. The mixture was then thermally treated at 80 °C for 8 h and then aged at ambient temperature for a period of 12 h. This was followed by filtration and washing with DI water and finally drying at 80 °C for 6 h.

A combination of milling method and reduction were used for Y_2O_3-based catalysts,[124] while calcination under controlled conditions gave stability and phase formation in different supports such as La_2O_3 and CeO. The Y_2O_3 support was synthesized hydrothermally. RuO_2 NPs were prepared by adding a $RuCl_3$ precursor to a KOH solution under constant stirring, followed by filtration, washing, and drying at a temperature of 80 °C for a period of 8 h. Ru/Y_2O_3-m were prepared by milling RuO_2 and Y_2O_3 in a mortar for 10 min and then reducing at 400 °C for 2 h under 75% H_2/N_2. Fig. 17 shows the TEM images along with Ru particle size distributions for 3% Ru/Y_2O_3-m (a and e), 5% Ru/Y_2O_3-m (b and f), 3% Ru/Y_2O_3-p (c and g), and 5% Ru/Y_2O_3-p (d and h) catalysts, synthesized using the above method.

The co-precipitation method enabled the formation of homogeneous MgO–Nd_2O_3 (ref. 116) supports, allowing fine tuning of the Mg/Nd ratio, followed by wet impregnation for efficient loading of Co. Magnesium and neodymium nitrates were dissolved in water at 30 °C, followed by dropwise addition of K_2CO_3 and KOH under stirring until the pH became 11. The precipitate was aged at 65 °C for 18 h, washed, dried (120 °C, 18 h), and calcined (450 °C, 18 h).

Co (10 wt%) was loaded on these supports *via* wet impregnation using cobalt nitrate, followed by drying (120 °C, 18 h) and calcination (500 °C, 18 h). Similarly, benchmark Co/MgO and Co/Nd_2O_3 catalysts were also prepared. Before catalytic testing, all samples were reduced in H_2 at 550 °C to ensure complete Co precursor reduction.

CeO_2 (ref. 119) was synthesized using the precipitation method with ethanol (CeO_2-e) and water (CeO_2-w) as solvents. For CeO_2-e synthesis, cerium nitrate was dissolved in ethanol, followed by the dropwise addition of 28 wt% ammonia solution and dilution with ethanol. The mixture was stirred for 2 h, then the precipitate was filtered, washed with ethanol, dried at 60 °C overnight, and finally calcined at 500 °C for 2 h. CeO_2-w was similarly prepared, using water as the solvent instead of ethanol. Ru was then incorporated onto these supports using the usual wetness impregnation method with ruthenium nitrosyl nitrate as the precursor.

In the synthesis of Ru/MgO,[120] a hydrothermal method facilitated the development of hexagonal nanoplates having

better porosity and dispersion, while Ba impregnation changed Ru/MgO interfaces, favouring the optimization of catalytic sites. $RuCl_3$ and NaOH mixed with MgO in water and thermally treated at 160 °C. This resulted in the formation of Ru-modified $Mg(OH)_2$ with a hexagonal nanoplate morphology, which transformed into mesoporous MgO after calcination at 500 °C. Ru^{4+} was atomically dispersed on MgO, and subsequent H_2 reduction at a temperature of 500 °C formed Ru particles. Ba–Ru/MgO catalysts (Ba/Ru molar ratio = 0.75) were prepared by impregnating Ru/MgO with Ba $(NO_3)_2$, followed by H_2 treatment at 500 °C. Ru catalyzed $Ba(NO_3)_2$ decomposition at a lower temperature (225 °C), forming BaO–Ru interfaces. To control BaO–Ru interactions, the temperature ramp was varied (2–20 °C min^{-1}), with the slowest ramp (2 °C min^{-1}) in humid H_2 producing "Ba–Ru/MgO–2H." A physical mixture of Ru/MgO and BaO/MgO was also prepared as a control sample.

The solvothermal method was used to prepare Ru–CeO_2 (ref. 130) composites, conducive to high Ru dispersion. Here, the Ru–Ce–BTC MOF forms through coordination between cerium, Ru, and BTC in DMF, creating a porous structure. Calcination converts the MOF into RuO_x–CeO_2, and subsequent hydrogen reduction at 450 °C generates highly dispersed Ru–CeO_2 catalysts with controlled Ru loading. The Ru–Ce–BTC MOF was synthesized by stirring cerium nitrate, $Ru(acac)_3$, and benzene-1,3,5-tricarboxylate (BTC) in DMF at 130 °C for 20 h. This was followed by washing the solid, drying at 80 °C, and calcination at a temperature of 450 °C for 3 h in air to obtain RuO_x–CeO_2. Finally, the solids were reduced at 450 °C under 10% H_2/N_2 to yield Ru–CeO_2 catalysts with Ru contents of 1.4–5.3 wt%. For comparison, the Ce–BTC MOF was synthesized without Ru, followed by calcination to obtain CeO_2. An impregnated Ru/CeO_2 catalyst was prepared by adding $Ru(acac)_3$ in ethanol to CeO_2, drying at 100 °C, calcining at 450 °C, and reducing under 10% H_2/N_2. Fig. 18 shows the schematic of this preparation method.

The hydrothermal method was also used for the development of nanostructured supports such as Y_2O_3 and Sm_2O_3,[131] and thereafter, deposition and reduction to obtain the final catalysts. Fig. 19 illustrates this synthesis method in detail. $Sm(OH)_3$ was prepared by dissolving samarium nitrate in DI water followed by adjusting the pH to ~13 with 20 wt% KOH and stirring for 15 min. The mixture was then hydrothermally treated at 180 °C for 12 h, filtered, washed, and dried at 80 °C. Finally, Sm_2O_3 was obtained by calcining $Sm(OH)_3$ at 500 °C for 2 h. Ru/Sm_2O_3 catalysts (2–5 wt% Ru) were synthesized *via* an ion adsorption method by dispersing $Sm(OH)_3$ support in

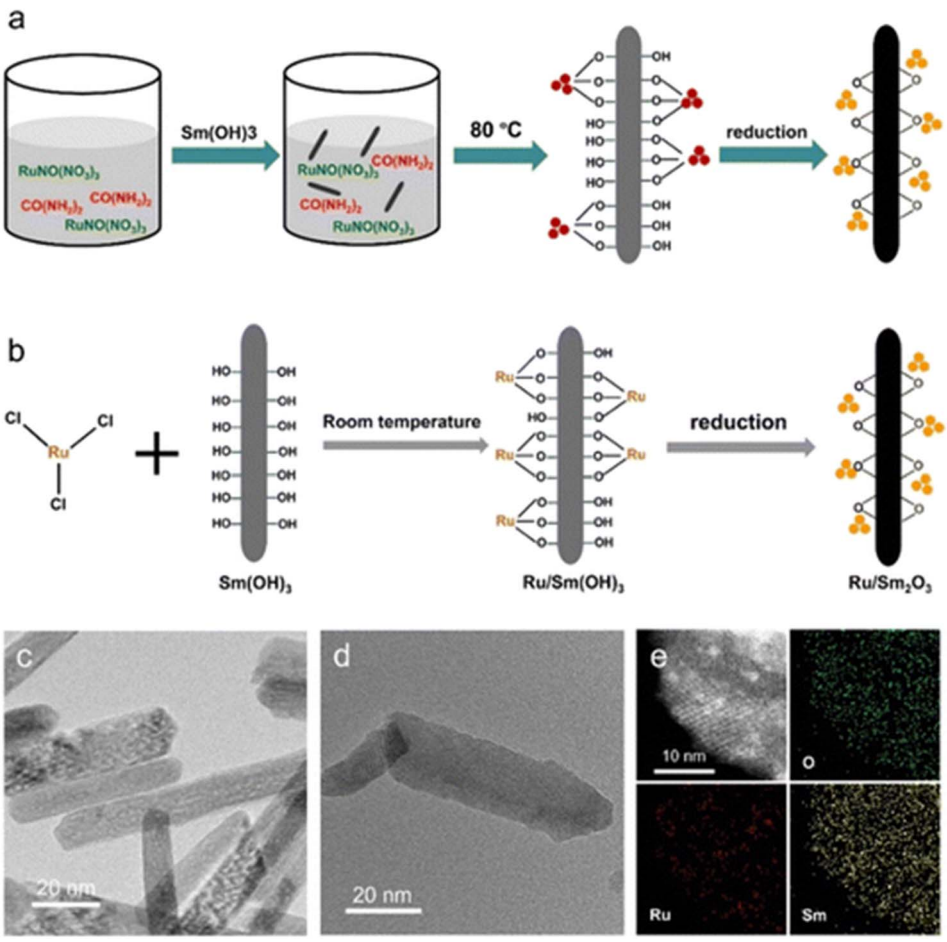

Fig. 19 (a) Schematic of the synthesis method of Ru(cluster)/Sm_2O_3. (b) Green ion adsorption method for the synthesis of Ru/Sm_2O_3 catalyst. (c) TEM image of the prepared $Sm(OH)_3$ support. (d) TEM image of 4% Ru/Sm_2O_3 catalyst. (e) HAADF-STEM image of 4% Ru/Sm_2O_3 and EDX elemental mappings for O, Ru and Sm. Adapted with permission from ref. 131. Copyright 2022, the Royal Society of Chemistry.

water, adding a $RuCl_3$ precursor solution, and stirring for 6 h. The precipitate was filtered, washed, dried at 80 °C, and reduced in 75% H_2/N_2 at 400 °C for 2 h. Ru/$Sm(OH)_3$ reduced at 400 °C and 1.0 MPa for a period of 1 h was termed the "reduced catalyst," and another sample reduced for 12 h was termed the "activated catalyst." As a reference, 4% Ru NPs/Sm_2O_3 was prepared by an impregnation method, dried at 80 °C, calcined at 550 °C in Ar for 2 h, and reduced at 400 °C in 75% H_2/N_2 to obtain the final catalyst.

The repetitive deposition–precipitation method allowed for the fine loading of Co onto Nd_2O_3 (ref. 121) through multiple cycles for enhanced metal–support interaction.

Nd_2O_3 powder was calcined at 800 °C for 16 h to remove hydroxides and carbonates. Co catalysts were prepared *via* recurrent deposition–precipitation. $CoCO_3$ was precipitated using K_2CO_3 from cobalt nitrate, on an Nd_2O_3 suspension at a temperature of 85 °C at a rotation speed of 500 rpm, until the pH became 9, and then aged for 1 h. The precipitate was filtered, washed till the pH turned 7 and then dried at 120 °C for 24 h. Finally, it was calcined at 500 °C for a period of 5 h. Higher Co loadings were achieved by sequential deposition–calcination cycles. The final catalysts (Co(*X*)/Nd_2O_3) were tabletted, crushed (0.2–0.63 mm), and reduced *in situ* before use.

Precipitation and coprecipitation methods are important for the precise control of the composition of CoCe-m perovskite catalysts,[137] which guarantees uniform active site distribution, increasing the catalytic efficiency. For Ba incorporation, the impregnation method ensures good loading on the Co catalyst and enhances thermal stability and dispersion of the active components, which is vital for high-performance reactions. The sol–gel method used for the synthesis of $BaCeO_3$ (ref. 139) serves to promote phase purity and homogeneity, which are needed for stability and activity of this compound in high-temperature reactions. The modified alkaline ethylene glycol reduction method for making Ru nanoparticles allows for size precision control helpful in maximizing surface area and active sites from the perspective of catalytic activity in hydrogenation and calcination reactions. Finally, the glycine nitrate process (GNP)[140] for Ru-doped BCY enhances the exsolution and stability of catalysts under reducing conditions, making it potential for difficult catalytic processes such as fuel cells and ammonia synthesis. All these synthesis methods are optimizing the performance of individual catalysts, as well as ensuring their robustness and stability across multiple industrial applications worldwide.

Recently, Sato *et al.* have published a comprehensive review for the catalytic role of basic oxide-Ru interface for generating ammonia under mild conditions.[141] Within the literature, cobalt-based catalysts are generally employed with the support materials to increase the catalytic activity. Hence, several supports such as activated carbon,[142,143] cerium oxide,[144] magnesium oxide,[145] or mixed magnesium–lanthanum oxides[146,147] are frequently used. Moreover, it is found that catalyst supports such as electrides, hydrides, and rare earth metal nitrides rapidly lose their activity with time, primarily because of the tendency to agglomerate the active metal species.

In this regard, Ronduda *et al.* reported a detailed study consisting of cobalt catalysts supported on mixed MgO–Ln_2O_3 (Ln = La, Nd, and Eu), and studied the effect of metallic cobalt loading for the activity towards ammonia synthesis.[116,148] Mixing magnesium oxide with lanthanide oxide provides the possibility to reduce the price, and exploit the advantages of both oxides. This series of works showed that tailoring the support composition by selecting lanthanide elements differing in electronegativity values remarkably alter active phase dispersion, access of active sites for hydrogen and density of basic sites on the surface. Consequently, this results in a better activity than the other studied catalysts. For instance, a series of Co/MgO–Nd_2O_3 catalysts with varying molar ratios of Mg/Nd (2, 4, 7, 10, and 12) resulted in a gradual change in the adsorption as well as textural and structural properties.[116] The variation in the catalytic activity of Co/MgO–Nd_2O_3 was observed due to the difference in adsorption properties. Mg/Nd was reported to have the maximum number of basic sites on the surface and exhibited the highest Co dispersion, which resulted in the best distribution of Co particles. All this led to enhanced catalytic activity of the Co/10MgO–Nd_2O_3 catalyst over other conventional catalysts. As the binary composite support consisting of MgO and Nd_2O_3 was used, the resulting catalyst demonstrated a greater activity than a single-composite support in aspects of catalyst activity, stability and cost of synthesis. Ammonia synthesis activity of Co/Mg–Nd catalysts with varying Mg/Nd ratios and comparison with different catalysts are shown in Fig. 20a–c. Moreover, the activity was closely related to the molar ratio of Mg/Nd, and exhibited a rate of 23.4 mmol g^{-1} h^{-1}, which increased to 39.3 mmol g^{-1} h^{-1} when Co/10Mg–Nd was employed. This also led to a significant decrease in the activation energy from 58.9 kJ mol^{-1} (Co/2Mg–Nd) to 53.7 kJ mol^{-1} (Co/10Mg–Nd).

It was thus concluded that different surface adsorption properties, which were tuned by the change in the molar ratio of Mg/Nd, were responsible for the enhanced catalytic activity of the Co/Mg–Nd catalyst. The nitrogen dissociation rate was increased due to the large number of basic sites and greater concentration of oxygen species with electron donating properties. Increased number of basic sites could facilitate strong interaction between magnesium and neodymium oxides.

In another work of Ronduda *et al.*, authors investigated the threshold value for cobalt loading, which could provide high catalytic activity and maximize the utilization of active cobalt surface sites for participating in the ammonia synthesis reaction.[133] This study is important for the development of cost-effective and efficient catalysts. Specifically, the authors studied the effect of metal loading on the catalytic activity of Co catalysts supported on MgO–La_2O_3 oxides (prepared by the wetness impregnation method) for the synthesis of ammonia. A relationship was developed between the amount of Co loading and the rate of ammonia synthesis. The rate reached a maximum at 40 wt% Co deposition. It was noted that changing the Co loading amount does not show any significant change in the surface-specific activity (TOF). The study also shows that ammonia synthesis rate for the given catalyst does not depend on the structural characteristics or size of Co NPs but is a strong function of Co loading amount. At 400 °C and

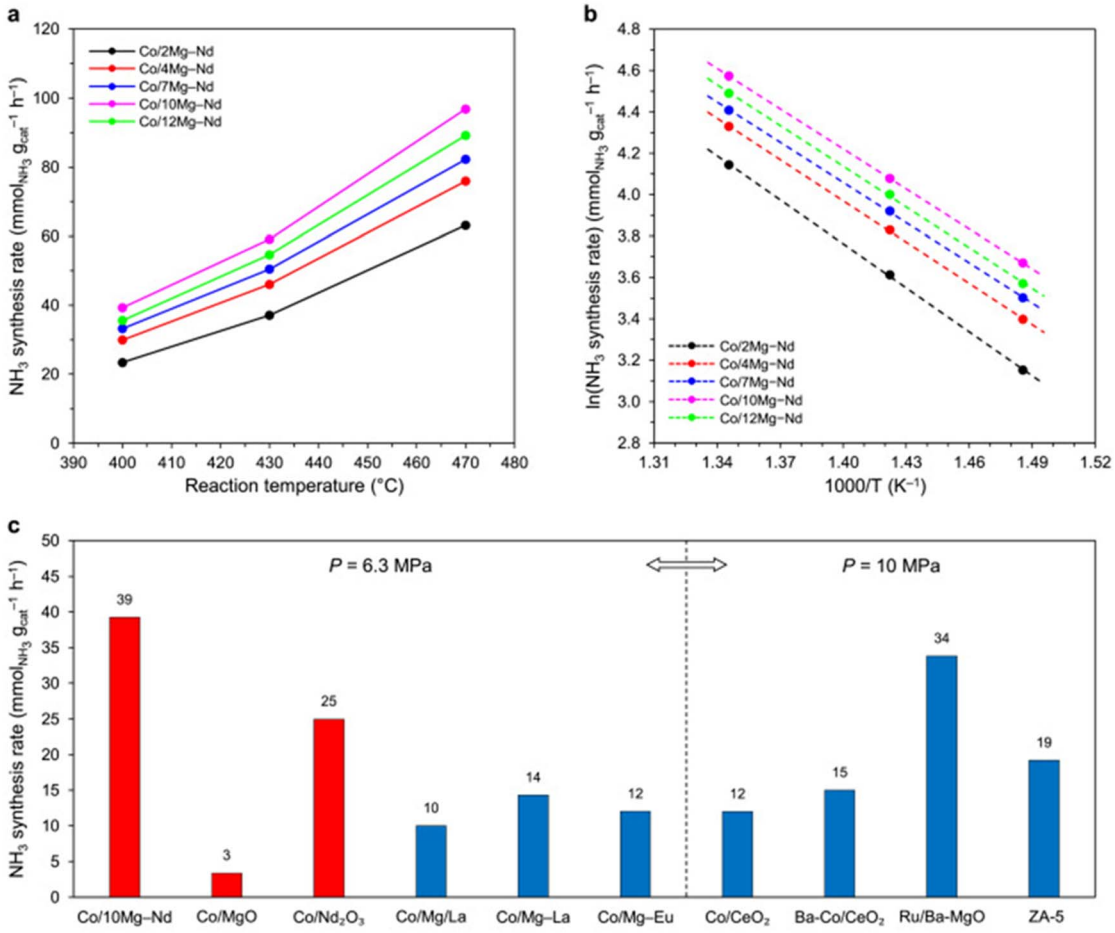

Fig. 20 Ammonia synthesis activity of Co/Mg–Nd catalysts with varying Mg/Nd ratios. (a) NH_3 synthesis rates as a function of temperature at 6.3 MPa. (b) Arrhenius plots under the same pressure. (c) Comparison of the NH_3 synthesis rates at 400 °C across different catalysts, including Co/10Mg–Nd, Co/MgO, and Co/Nd_2O_3. Adapted with permission from ref. 116. Copyright 2022, Elsevier.

6.3 MPa, the ammonia synthesis rate of Co (10)/Mg–La was 15.7 $mmol_{NH_3}\ g_{cat}^{-1}\ h^{-1}$, which was increased to 40.3 $mmol_{NH_3}\ g_{cat}^{-1}\ h^{-1}$ for Co(50)/Mg–La. However, a further increase in the Co loading from 40 to 50 wt% led to a slight decrease in the rates, owing to the decrease in the number of basic sites. Moreover, the rates were increased by only 20%, when the pressure was increased from 6.3 to 9.0 MPa. Importantly, the catalysts were thermally stable and showed high resistance towards sintering and thus, a negligible decrease in the activity was noticed even after overheating at 600 °C for 75 h. The findings clearly demonstrate that the ammonia synthesis rate was dependent on the amount of Co loading.

Next, researchers have co-incorporated Ba and Ce by a coprecipitation method to prepare (Ba/CoCe) and examine their activity.[137] The striking observation was that the $BaCeO_3$ perovskite boosts the ammonia synthesis kinetics. Moreover, the *in situ* DRIFTS analysis (shown in Fig. 21a) revealed that the reaction at the Co–$BaCeO_3$ interface follows the associative pathway, confirmed by the formation of hydrazine intermediate ($-N_2H_4$) and subsequent homolytic dissociation, which generates ammonia under mild conditions. In particular, the catalytic activity of Co, CoCe-m, *n*Ba/Co, and *n*Ba/CoCe-m catalysts were evaluated at a temperature of 400 °C and a pressure of 5.0 MPa. The catalytic performance was compared in terms of weight time yield (WTY, $g_{NH_3}\ g_{cat}^{-1}\ h^{-1}$) of NH_3 over catalysts. The pure Co catalyst exhibited very low activity, but doping Co with Ce up to 0.05 M ratio led to an increase in activity irrespective of the change in Ba content (0, 2, and 5 wt%). A further increase in the Ce amount had negative effects, which suggest a volcano trend in the catalytic activity curve. WTY_{NH_3} ($g_{NH_3}\ g_{cat}^{-1}\ h^{-1}$) for 5Ba/CoCe-0.05, Ba-5 wt% Ru/CB, Ba-2.5 wt% Ru/CB, and Co@Ba/MgO were 0.254, 1.359, 0.458 and 0.040, respectively. Upon optimizing the content of Ba, it was found that 5Ba/CoCe-0.05 shows the highest activity (WTY = 0.254 $g_{NH_3}\ g_{cat}^{-1}\ h^{-1}$) among all the catalysts. It was seen that the co-incorporation of a small quantity of Ba and Ce on Co can increase the activity of the Co catalyst to a maximum of 92-folds, comparing pristine Co. To determine the size of reactor and also the process variables, the volume-normalized catalytic activity was determined. To judge how effective the Ba/CoCe catalyst is, a comparison between its space time yield of NH_3 (STY_{NH_3}, $g_{NH_3}\ cm_{cat}^{-3}\ h^{-1}$) was made with other benchmark catalysts. Then 5 Ba/CoCe-0.05 exhibited much higher STY_{NH_3}

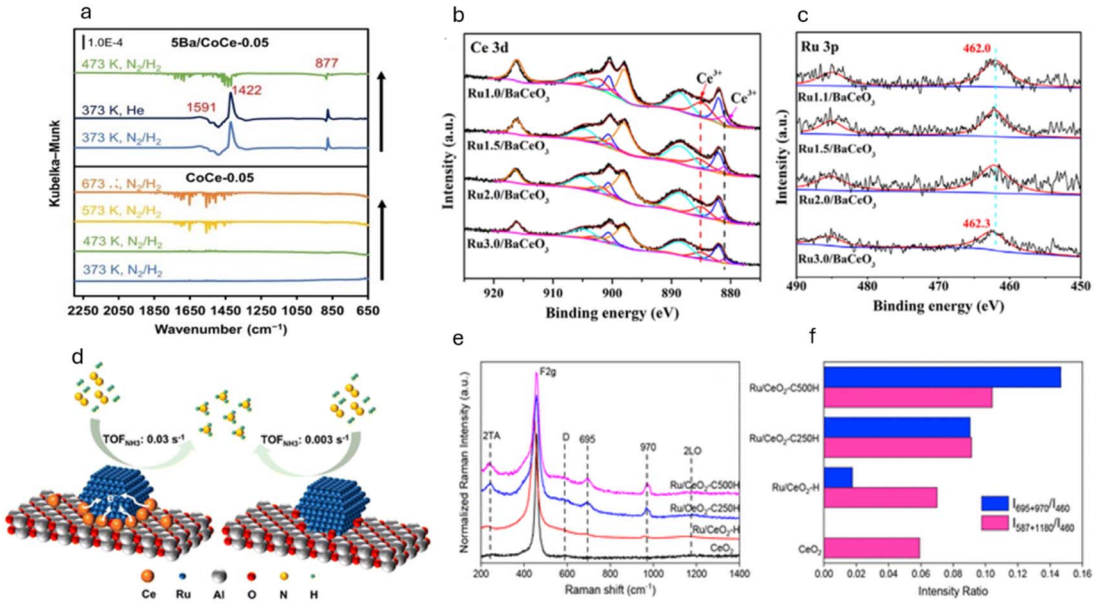

Fig. 21 (a) *In situ* DRIFT spectra for ammonia synthesis over CoCe-0.05 and 5Ba/CoCe-0.05 catalysts examined at 373–673 K (100–400 °C) and 0.1 MPa. Adapted with permission from ref. 137. Copyright 2023, Elsevier. (b) Ce 3d XPS spectra and (c) Ru 3p XPS spectra of the $Ru_x/BaCeO_3$ catalyst. Adapted with permission from ref. 139. Copyright 2021, Elsevier. (d) Schematic of the ammonia formation over Ce–Ru/Al_2O_3 and Ru/Al_2O_3 catalysts. Adapted with permission from ref. 117. Copyright 2023, the Royal Society of Chemistry. (e) Raman spectra of different samples. (f) $I_{695+970}/I_{460}$ and $I_{587+1180}/I_{460}$ intensity ratios. Adapted with permission from ref. 135, Copyright 2021, the American Chemical Society.

(0.309 g_{NH_3} cm_{cat}^{-3} h^{-1}) when compared to the Ba-promoted Co catalyst (Co@Ba/MgO, $STY_{NH_3} = 0.024$ g_{NH_3} cm_{cat}^{-3} h^{-1}).

On evaluation of activation energies for different catalysts, it was found that the activation energy for Co was 141 kJ mol^{-1} and those for 5Ba/Co and CoCe-0.05 were 157 and 196 kJ mol^{-1}, respectively. The high value of activation energy is in contrast to the fact that they exhibited a higher catalytic activity than that of pure Co. It was thus concluded that singly doped Ba or Ce do not show any reduction in activation energy barrier for the synthesis of ammonia. An apparent activation energy of 57 kJ mol^{-1} for 5Ba/CoCe-0.05 is the least among all the examined catalysts. These studies show that the presence of Ba and Ce tunes the active sites in such a way that the rate-determining step shifts towards a more kinetically favourable step.

The reason behind high activity of $Co/BaCeO_{3-x}N_yH_z$ was the progression of the reaction *via* the Mars-van Krevelen (MvK) mechanism, while the high activation barrier in the case of Co/$BaCeO_3$ was due to reaction progression *via* the Langmuir–Hinshelwood mechanism. *In situ* DRIFTS studies were performed to get an insight into the reaction mechanism and the obtained spectra can be found in Fig. 21a.

As Fig. 21a depicts, the 5Ba/CoCe-0.05 catalyst demonstrated peaks at 1591 cm^{-1} (deformation of $-NH_2$), 1422 cm^{-1} (wagging of $-NH_2$) and 877 cm^{-1} (rocking of $-N_2H_4$).[149–151] Hence, the observation of $-N_2H_4$ proved that the reaction proceeds *via* associative mechanism. When the gas flow was switched to He, peaks with similar intensities were observed, which indicates the presence of strongly chemisorbed species. At 200 °C, the peak intensity diminished, indicating the rapid desorption rate, which is also confirmed from TPD MS studies. From the results of *in situ* DRIFTS, it was observed that ammonia synthesis at the Co–$BaCeO_3$ interface is mediated by the generation of hydrazine, which dissociated thereafter (*i.e.* associative mechanism).

In another work, Zhou studied the ammonia synthesis ability of $Ru_x/BaCeO_3$ catalysts with Ru sizes of 1.1–3.0 nm. It was found that reducing the Ru size significantly boosts NH_3 synthesis.[139] $Ru1.1/BaCeO_3$ achieved 19.4 mmol g_{cat}^{-1} h^{-1} at 400 °C and 1 MPa, 5.7 times the rate of $Ru_{3.0}/BaCeO_3$, outperforming many Ru-based catalysts. Smaller Ru particles enhance Ce^{3+} and oxygen vacancy formation in $BaCeO_3$, facilitating electron transfer to Ru and improving N_2 dissociation. Additionally, smaller Ru size promotes hydrogen spillover to $BaCeO_3$, reducing hydrogen poisoning and enhancing catalytic efficiency. The Ce 3d XPS spectra of $Ru_x/BaCeO_3$ ($x = 1.1$–3.0) catalysts reveal ten characteristic peaks (Fig. 21b and c). Ce^{3+} species are identified at 881.1 and 884.8 eV, while six other peaks correspond to Ce^{4+}. The Ce^{3+} proportions (30%, 24%, 17%, and 14%) correlate with the increasing x values. The formation of Ce^{3+} creates oxygen vacancies (O_v) in $BaCeO_3$, with concentrations estimated at 5.0%, 4.0%, 2.8%, and 2.3%. These Ce^{3+} and O_v species act as electron donors, altering the Ru valence. The Ru 3p XPS spectra show positively charged Ru at higher x values (462.3 eV for $Ru_{3.0}$) and metallic Ru at lower x values (462.0 eV for $Ru_{1.1}$). Ru L-edge NEXAFS confirms changes in Ru's electronic structure due to Ce^{3+} and O_v presence.

Previous works illustrated that the interfacial synergy between metal nanoparticles and the metal oxide significantly influence the catalytic performance of Ru-based catalysts. Hence, the major issue is to precisely construct the interface structure at the nanoscale of the promoter-decorated Ru nanoparticles. This challenge was addressed by Feng *et al.*, who

prepared the Ce–Ru/Al_2O_3 catalyst using a co-precipitation method, and the catalyst consists of Ru nanoparticles supported on γ-Al_2O_3 with sub-nanometer ceria (CeO_2) species.[117] A ten-fold increase in the catalytic activity was noticed when compared to Ru/Al_2O_3 at a temperature of 400 °C and 1.0 MPa. The reason behind this was explained to be the aggregation of sub-nanometre CeO_2 species on the Ru nanoparticles, leading to efficient electron transfer from CeO_2 to Ru NPs. The presence of CeO_2 species shows multiple positive effects as it diminishes hydrogen poisoning, facilitates N_2 adsorption and supports hydrogenation of dissociated N* atoms.

In the same work of Feng *et al.*, it was observed that Ru/Al_2O_3 showed very low activity for ammonia synthesis at 350 °C.[117] Even on increasing the temperature to 400 °C, it exhibited a rate of only about 1.435 mmol g_{cat}^{-1} h^{-1}. However, when the Ru NPs were decorated with CeO_2 species, a dramatic increase in its catalytic activity was observed under identical reaction conditions. As the content of CeO_2 increased in the Ce–Ru $(x:1)/Al_2O_3$ catalysts, the ammonia synthesis rate of Ce–Ru$(0.125:1)/Al_2O_3$, Ce–Ru$(0.25:1)/Al_2O_3$, Ce–Ru$(0.5:1)/Al_2O_3$ and Ce–Ru$(1:1)/Al_2O_3$ catalysts enhanced to 3.123, 7.925, 14.040 and 14.350 mmol g_{cat}^{-1} h^{-1} at 400 °C, respectively. The synthesis rate of 14.350 mmol g_{cat}^{-1} h^{-1} was obtained for Ce–Ru$(1:1)/Al_2O_3$ at a temperature of 400 °C, which is about ten-times higher than that of Ru/Al_2O_3. Comparing the activation energies for Ru/Al_2O_3 and Ce–Ru$(1:1)/Al_2O_3$ catalysts, it was observed that they exhibited similar activation energies of 82 kJ mol^{-1} and 75 kJ mol^{-1}, respectively, which could be because of a similar mechanism pathway for both the catalysts. Additionally, turnover frequencies (TOF) were calculated based on the metal dispersion values from CO chemisorption results. The Ce–Ru $(1:1)/Al_2O_3$ catalyst exhibited much greater values of TOF than the Ru/Al_2O_3 sample, which is attributed to the outstanding intrinsic activity of the Ce–Ru $(1:1)/Al_2O_3$ catalyst. Fig. 21d illustrates a plausible mechanism for ammonia synthesis over Ce–Ru/Al_2O_3 and Ru/Al_2O_3 catalysts. In the Ru/Al_2O_3catalyst, the Ru nanoparticles are entirely covered by the dissociated H* atoms, leading to poor access of the nitrogen molecules to the active Ru nanoparticles and subsequent interaction with nitrogen molecules. On the other hand, in Ce–Ru/Al_2O_3, the strong interaction between sub-nanometer Ce species and Ru nanoparticles can facilitate nitrogen adsorption and hydrogen activation. Therefore, abundant Ce species on Ru nanoparticles can promote ammonia synthesis *via* the efficient formation of NH_x ($x = 1$, 2 and 3) species from dissociated H* and N* adatoms on Ru–CeO_2 interfaces.

In another work, Lin discovered that in Ru/CeO_2 catalysts, strong metal–support interactions (SMSI) reduce the availability of metallic sites, hindering the performance for reactions requiring such sites.[135] However, CO activation of Ru/CeO_2 enhances the reduction and exposure of Ru species, increases Ce^{3+} concentration, and creates oxygen vacancies (O_v), leading to electron-rich $Ru^{\delta-}$ species and $Ru^{\delta-}$–O_v–Ce^{3+} sites. This CO-activated Ru/CeO_2 catalyst demonstrates high activity in ammonia synthesis and effectively minimizes hydrogen poisoning. H_2-TPR, DRIFTS, XPS, and Raman analysis (Fig. 21e and f) indicate that the CO activation of Ru/CeO_2 notably increases the reducibility and exposure of Ru species, enhancing Ce^{3+}, oxygen vacancies, and $Ru^{\delta-}$–O_v–Ce^{3+} concentrations.

Since electrides and metallic hydrides are unstable in air, alternative materials could provide solution for the industrial-scale production of ammonia. In a recent work of Zhao *et al.*, Ru catalysts were supported on perovskites of varying valence transition metals (*e.g.*, Nb and Ta).[138] In prior works, the respective authors synthesized Ru/$Sr_2Nb_2O_6$,[152] Ru/$Sr_2Ta_2O_7$ (ref. 153) and Ru/$Ba_5Ta_4O_{15}$ (ref. 154) and reported their excellent catalytic activity for ammonia synthesis. These valence transition metals can be reduced to generate oxygen vacancies (V_O), and the electrons confined in these V_O can be easily donated to Ru and further accelerate the dissociation of surface nitrogen molecules. Additionally, the V_O can accept the hydrogen atoms from Ru (*via* spillover mechanism) to avoid hydrogen poisoning of the Ru atoms. To generate more V_O in $Ba_5Ta_4O_{15}$, Zhao *et al.* pretreated the support with CaH_2 in different atmospheres and exploited its anionic defects for the synthesis of ammonia.[138] Importantly, the electron paramagnetic resonance (EPR) spectra was acquired to confirm the formation of anionic defects ($H_O^{\bullet}$ and $V_O^{\bullet}$) in CaH_2-reduced BNO supports (Fig. 22). It was seen that supporting Ru on 0.20CaBNO600 results in a decrease in the EPR signal of oxygen vacancies, which could be due to the partial transfer of electrons in oxygen vacancies to Ru NPs. This was also attributed to the formation of H atoms on Ru particles spilled over the support and reactions with the electrons trapped in oxygen vacancies, which result in the conversion of oxygen vacancies to H^- ($H_O^{\bullet}$). The oxygen vacancies with trapped electrons are represented as ($V_O^{\bullet}$). The addition of Cs promoter led to an increase of all the EPR signals. Importantly, the electron paramagnetic resonance (EPR) spectra was acquired to confirm the formation of anionic defects ($H_O^{\bullet}$ and $V_O^{\bullet}$) in CaH_2-reduced BNO supports (Fig. 22).

On optimizing the Ru loading, it was found that Ru/0.20CaBNO500 shows an ammonia synthesis rate of 2.6 mmol g^{-1} h^{-1}, which was the best among all the tested catalysts. 0.20CaBNO600 support was then reduced at 600 °C for a period of 12 h under argon flow and the best activity achieved was 4.0 mmol g^{-1} h^{-1} at 400 °C and 0.10 MPa. For further enhancement, Cs promoter was added to Ru/0.20CaBNO600. It was observed that 3Cs–Ru/0.20CaBNO600, which was activated at a temperature of 400 °C for 3 h in syngas, exhibited an optimum activity of 5.3 mmol g^{-1} h^{-1}. The same catalyst was tested for a period of 72 h and a 10% loss of activity was observed after a period of 40 h, which can be due to the loss of specific surface area of the support. Hence, Cs-addition helped to form the anionic defects in the support under the reaction conditions.

Of several oxides, MgO is an interesting material mainly because of its basicity, which increases high electron density in supported metal particles. Moreover, MgO is inexpensive and thermally stable. In particular, the MgO(111) facets have high electrostatic polarity compared to other facets of MgO, which helps to suppress hydrogen poisoning of Ru particles by capturing H^+. Often, the Ru/BaO/MgO composite has been employed for ammonia synthesis under mild conditions[155–158]

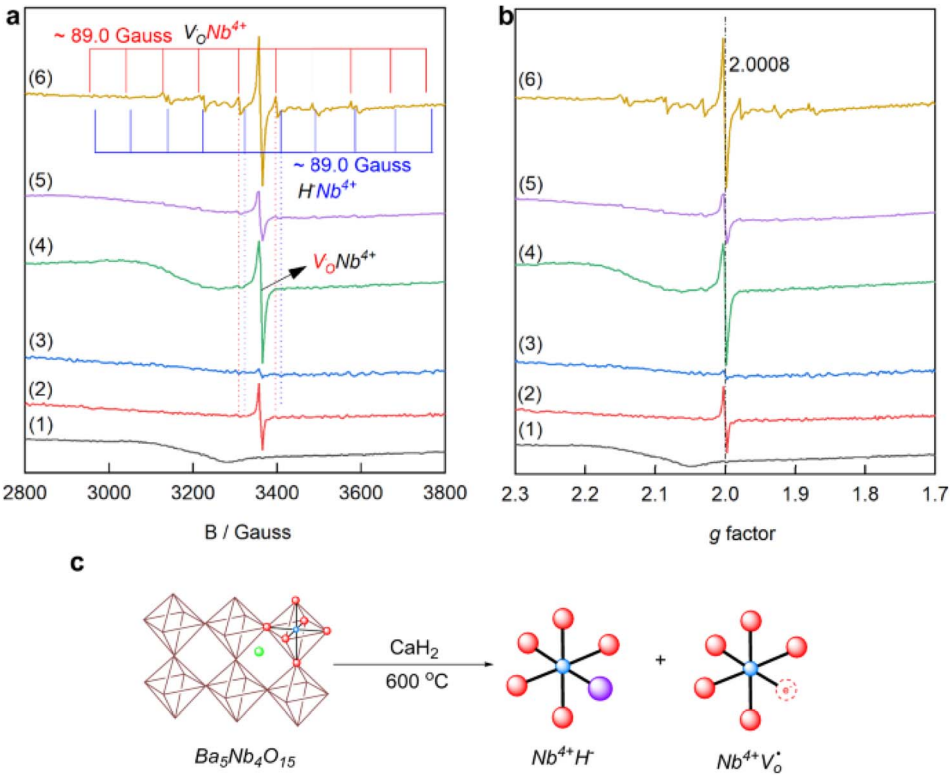

Fig. 22 EPR spectra ((a) magnetic field (b) g-factor) of (1) pristine BNO ($Ba_5Nb_4O_{15}$), (2) BNO, (3) Ru/BNO, (4) 0.20CaBNO600, (5) Ru/0.20CaBNO600, and (6) 3Cs–Ru/0.20CaBNO600. All samples other than pristine BNO have been reduced under H_2 for 3 h at 400 °C prior to collecting the EPR spectra. (c) Schematic model demonstrating the generation of two types of distorted octahedra (NbO_6) connected to H- or oxygen vacancy. Adapted with permission from ref. 138. Copyright 2023, Springer Nature.

and the Ru–BaO interfacial area is primarily tailored to increase the activity.[159] This interface promotes the splitting of H atoms into H^+/e^- pairs; where BaO holds H^+ (as it has strong basic characteristics and is non-reducible) and Ru holds e^-. Expectedly, increased electron density on Ru facilitates the adsorption of nitrogen on the surface and also inhibits hydrogen poisoning. For instance, Y. Baik *et al.* synthesized a series of Ba–Ru/MgO catalysts, with ~2.3 nm Ru particle size and configured the BaO–Ru interfacial structures to obtain a synthesis rate of 945 mmol g^{-1} h^{-1} under mild conditions (400 °C and 1.0 MPa).[159] Moreover, identical phenomena were also noticed for a Cs-promoted Ru/MgO catalyst; however, Cs_xO_y–Ru interfaces were less efficient in storing H^+/e^- pairs than the BaO–Ru interfaces.

Recently, Lee *et al.* have investigated the role of MgO as a support for Ru–BaO in the synthesis of ammonia.[160] A comparative study using pristine MgO and MgO–Al_2O_3 mixed oxide ($MgAlO_x$) with varying MgO contents was performed. The study revealed that MgO imparts strong basicity to BaO, which acts as an electronic promoter to Ru. In specific, the authors first prepared MgO*n*, where *n* is the MgO/(MgO + Al_2O_3) wt% in the precursor (n = 5, 30, 70, and 100) and next, wet-impregnation method was used to include Ba, and Ru to synthesize Ru–Ba/MgO*n* catalysts. The weight-time-yield (WTY) of ammonia over the different catalysts, along with various other kinetic parameters, is given in Fig. 23.

A clear correlation between the catalytic activity and the MgO content of the Ru–Ba/MgO*n* catalysts was noticed (Ru–Ba/MgO5 < Ru–Ba/MgO30 < Ru–Ba/MgO70 < Ru–Ba/MgO100), indicating the superior role of MgO. Notably, the Ru–Ba/MgO100 catalyst disclosed a TOF that is two orders of magnitude higher than that of Ba-free catalysts. Additionally, the apparent activation energy decreased from 154 kJ mol^{-1} to 42 kJ mol^{-1} with the increasing content of MgO in the catalysts. Importantly, a low activation energy of 42 kJ mol^{-1} unveils the high potential of Ru–Ba/MgO100 for low-temperature applications. However, the reaction order for ammonia was a huge negative value (−0.55) for Ru–Ba/MgO100, implying a strong interaction between ammonia and the catalyst surface. Additionally, this work includes diffusion limitation studies, which disclose that the Ru–Ba/MgO catalyst can have a pellet radius of few mm, and the pore size has negligible effects on the diffusion limitation. Such results are critical for the rational catalyst design.

Other oxides such as Al_2O_3,[161–163] MgO,[164,165] $MgAl_2O_4$,[166] Pr_2O_3,[167] La_2O_3,[168] CeO_2,[135] $La_{0.5}Ce_{0.5}O_{1.75}$,[169] Ru/$La_{0.5}Pr_{0.5}O_{1.75}$,[170] and barium hexa-aluminate[171,172] were employed as supports for Ru-based catalysts. The role of oxide supports is not only to disperse the Ru nanoparticles but also to provide stability. Moreover, these supports strengthen the interface phenomena through metal–support interactions and this contributes to increase the catalytic performance of Ru nanoparticles on oxide supports. Yttrium oxide (Y_2O_3) is one

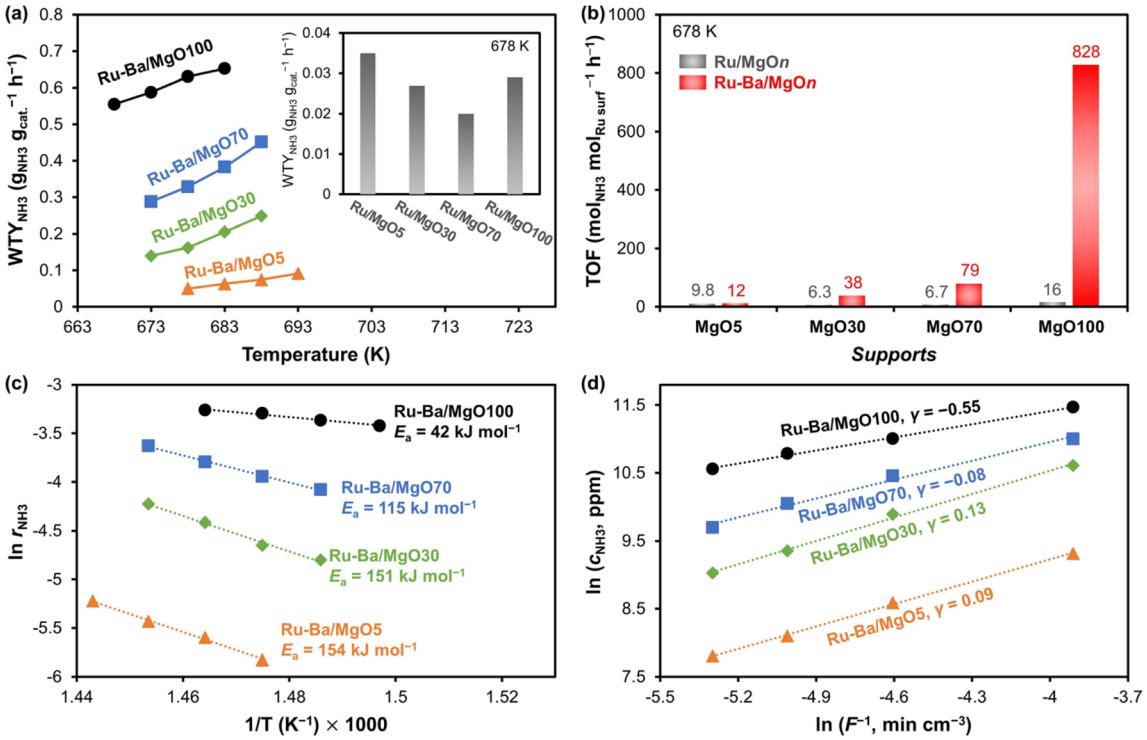

Fig. 23 (a) Temperature-dependence ammonia synthesis rates over different catalysts. (b) TOF at 405 °C for Ru/MgO*n* and Ru–Ba/MgO*n* catalysts. (c) Arrhenius plot for activation energy determination. (d) Reaction order analysis for ammonia over Ru–Ba/MgO*n* catalysts. Adapted with permission from ref. 160. Copyright 2024, Elsevier.

such material, which offers unique properties such as high chemical stability, high melting point, and low volatility. Feng *et al.* prepared Y_2O_3-supported Ru *via* a milling method (referred to as Ru/Y_2O_3-m) or precipitation method (denoted as Ru/Y_2O_3-p), and subsequently, reduced these samples at 400 °C for 2 h in a 75% H_2/N_2 stream.[124] The activity tests were evaluated at 1.0 MPa. Under this condition, the given catalyst was heated to a temperature of 400 °C at a ramp rate of 5 °C min^{-1} under a flow of 75% H_2/N_2 mixture and made to dwell at 400 °C until the activity reached a steady-state. Notably, the bare Y_2O_3 support exhibited negligible activity for ammonia synthesis, whereas Ru/Y_2O_3-m and Ru/Y_2O_3-p samples exhibited much higher activity under the same conditions; 5% Ru/Y_2O_3-p catalyst exhibited ammonia synthesis rate of 21.120 mmol g_{cat}^{-1} h^{-1} at a temperature of 400 °C with a WHSV of 24 000 mL g_{cat}^{-1} min^{-1}, which was greater than both references, *i.e.*, 5% Ru/γ-Al_2O_3-p (6.5 mmol g_{cat}^{-1} h^{-1}) and Ru/Y_2O_3-m (4.378 mmol g_{cat}^{-1} h^{-1}). Keeping the same conditions, the activity of the 5% Ru/Y_2O_3-p (18.456 mmol g_{cat}^{-1} h^{-1}) catalyst was close to those of many conventionally used catalysts such as Ba–Ru/AC, Cs–Ru/MgO and Ru/CeO_2, proving its superior catalytic performance.

Of note, the structures of active sites in different Ru/Y_2O_3-m and Ru/Y_2O_3-p catalysts were identical, as confirmed by their identical activation energies. For estimating the intrinsic activity of different catalysts, their TOFs were compared. The 5% Ru/Y_2O_3-p showed a TOF of 0.019 s^{-1} which is greater than that of 3% Ru/Y_2O_3-m (0.005 s^{-1}) and 5% Ru/Y_2O_3-m (0.005 s^{-1}) samples, at 400 °C. It should be noted that the TOF of 5% Ru/Y_2O_3-p (0.011 s^{-1}) at a temperature of 350 °C was 7.9 and 8.5 times greater, as compared to that of the 3% Ru/Y_2O_3-m (0.0014 s^{-1}) and 5% Ru/Y_2O_3-m (0.0013 s^{-1}) catalysts, respectively. Such increased values of TOFs were further examined to get an insight into the mechanistic details. It was thus concluded that the modulated electronic structures enhanced the activity of Ru nanoparticles in Ru/Y_2O_3-p, owing to the facilitated dissociation process of nitrogen and hydrogen molecules. Moreover, the metal support interaction in Ru/Y_2O_3-p catalysts can regulate the electronic structures of Ru nanoparticles, which then facilitates activation and dissociation to form ammonia.

Previous reports suggest that the adsorption ability of hydrogen can be tailored by the spatial arrangements of Ti species for Ru/CeO_2 catalysts, and thus, the as-prepared catalysts can demonstrate a superior catalytic activity.[173] In this regard, Li *et al.* further investigated the effect of Ti-species on CeO_2-supported Ru catalysts to engineer an efficient ammonia synthesis catalyst.[96] Fig. 24a and b illustrate the enhancement of hydrogen desorption on the Ru/CeO_2 catalyst before and after the introduction of Ti species.

In this work, a solid solution of Ti and CeO_2 ($CeTiO_{2-x}$) was synthesized and characterized by XRD and Raman spectroscopy. The detailed study found that the solid-solution was conductive for higher dispersion of Ru particles (validated by Raman and UV-vis results) and hydrogen adsorption. CO-TPR and ^{1}H NMR indicates that Ti in Ru/CeO_2 decreased the number of the active oxygen species, and therefore, the catalysts

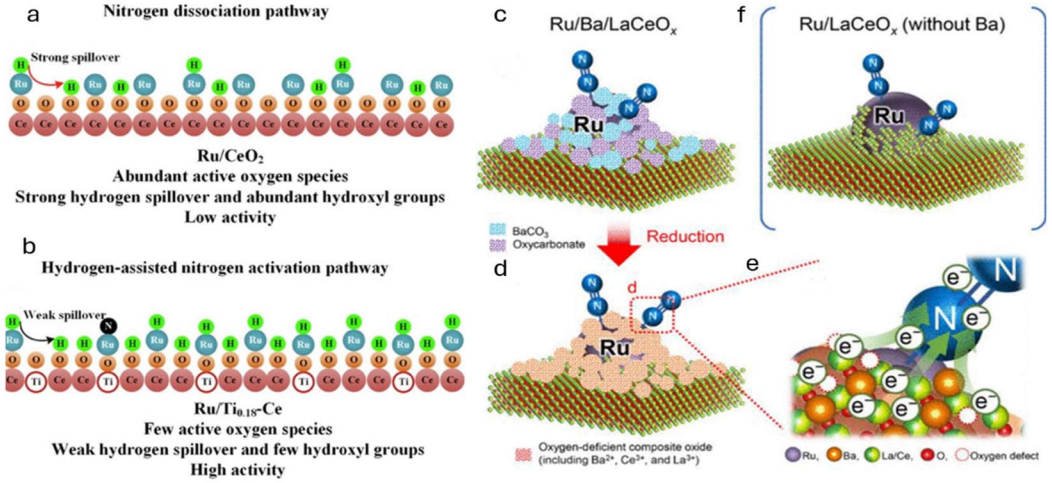

Fig. 24 (a) Schematic of the influence of Ti species on ceria-supported Ru catalysts Ru/CeO_2 and (b) $Ru/Ti_{0.18}$–Ce. Adapted with permission from ref. 96. Copyright 2022, Elsevier. (c) Illustration of the surface morphology of $Ru/Ba/LaCeO_x$_500red, (d) $Ru/Ba/LaCeO_x$_700red, (e) nitrogen activation steps on $Ru/Ba/LaCeO_x$_700red, and (f) $Ru/LaCeO_x$_650red. Adapted with permission from ref. 174. Copyright 2020, the American Chemical Society.

led to an increase in the hydrogen species desorbed at low temperatures, which facilitates nitrogen dissociation and alleviates hydrogen poisoning. This study illustrates that the ammonia synthesis rates of Ru catalysts follow a volcanic trend with the increase in titanium butoxide volume. Comparing Ru/CeO_2 and Ru/TiO_2, the formation of $CeTiO_{2-x}$ solid was essential to increase the activity of $Ru/Ti_{0.18}$–Ce (18.9 mmol g^{-1} h^{-1}). Moreover, in the absence of heat and mass transfer effects, the nitrogen reaction order was below 1.0 and the hydrogen reaction order was 0.47, confirming the role of Ti in increasing the nitrogen dissociation, and suppressing hydrogen poisoning, and thereby, enhancing the ammonia synthesis rates. As shown in Fig. 24b, $CeTiO_{2-x}$ controls the amount of active oxygen species, which could be used for hydrogen spillover. Below 300 °C, the desorption of hydrogen species from the Ru sites of $Ru/Ti_{0.18}$–Ce was higher because of the Ti species and this resulted in the hydrogen-assisted nitrogen activation pathway instead of direct dissociation. Therefore, $Ru/Ti_{0.18}$–Ce was found to be an efficient ammonia synthesis catalyst.

In an interesting work of Sato *et al.*, $Ru/Ba/LaCeO_x$, pre-reduced at 700 °C, demonstrated an activity of 52.3 mmol g^{-1} h^{-1} at 350 °C, and 1.0 MPa.[174] The TOF at this temperature was more than 8 times that of the Cs^+/Ru/MgO catalyst. Moreover, hydrogen poisoning, a typical drawback of oxide-supported Ru catalyst, was efficiently suppressed by the $Ru/Ba/LaCeO_x$ catalyst. The characterization results revealed that Ru particles were surrounded by low-crystalline, oxygen-deficient nanofraction including Ba^{2+}, Ce^{3+}, and La^{3+}. A pictorial representation of the same can be found in Fig. 24c–f for better understanding.

To study the effect of Ba^{2+}, a comparison of the physicochemical properties of $Ru/Ba/LaCeO_x$_700red with those of $Ru/LaCeO_x$_650red was performed. Comparing the later catalyst, the former had a smaller specific surface area and larger Ru particles. The TOF for $Ru/Ba/LaCeO_x$_700red (0.248 s^{-1}) was about five-times that for $Ru/LaCeO_x$_650red (0.049 s^{-1}). It was therefore concluded that addition of Ba^{2+} had a positive effect on the TOF and synthesis rate of ammonia. Moreover, the effect of catalyst pre-reduction temperature on the ammonia generation rate of $Ru/Ba/LaCeO_x$ was explored. With the increase in pre-reduction temperature, the ammonia synthesis rate was also found to considerably increase. However, beyond 800 °C, this rate was decreased. Herein, the catalysts' structure was obtained by using the alkaline earth compounds and rare earth oxides which contain redox-active atoms. This compound showed greater electron-donating capacity owing to the strong basicity of the incorporated cations, removal of carbonate, and formation of oxygen deficient sites that remarkably avoided the electron withdrawing O^{2-} anions from the Ru-nanofraction interface. These electrons were then efficiently donated to antibonding orbitals of nitrogen molecules *via* Ru, which next cleaved the strong nitrogen triple bond and promoted the ammonia synthesis.

In a similar study by Sato *et al.*, Co nanoparticles were encapsulated with BaO, which increased the activity of Co, and in particular, Co@BaO/MgO-700red displayed a superior rate of ammonia synthesis.[175] For instance, a rate of 24.6 mmol g^{-1} h^{-1} and TOF (0.246 s^{-1}) of the catalyst were observed at 350 °C and 1.0 MPa. This result was about 80 and 250 times greater, respectively, than those of the non-doped pristine catalyst. With increase in pressure to 3.0 MPa, the rate was enhanced to 48.4mmol g^{-1} h^{-1}, which was significantly higher than that of active Ru-based catalysts. Based on the experimental findings, the underlying mechanism was proposed. The details suggest that the adsorption of nitrogen on Co atoms at the catalyst surface weakened the strong bond of nitrogen molecules by the electron donation from Ba^{2+} of BaO *via* adjacent Co atoms. Such steps accelerate the breaking of the triple bond and enhance the rates.

A major limitation of oxide and mixed-oxide-based catalysts is the requirement for high temperatures to activate N_2, which

can limit their energy efficiency. Additionally, maintaining the stability of oxygen vacancies under prolonged reaction conditions can be challenging, as vacancy annihilation may reduce catalytic activity over time. Furthermore, sintering of active metals, despite strong metal–support interactions, can still occur under harsh conditions, leading to deactivation. To address these challenges, future research should focus on developing oxide and mixed oxide catalysts with improved low-temperature activity by fine-tuning the oxygen vacancy concentration and electronic properties. Advanced synthesis techniques should be employed to achieve uniform metal dispersion and robust metal–support interfaces. Exploring novel oxide systems and doping strategies can also help enhance stability, reduce sintering, and maintain high activity over prolonged operation.

4. Observation for catalyst development

Next, a detailed analysis for potential industrial catalysts reveals that the catalysts should meet set criteria such as product selectivity (>70%), product concentration (>3 wt%), catalyst activity (0.1–10 $tonne_{product}$ per $m_{reactor}^3$ per h), and catalyst consumption (0.1–10 kg_{cat} per $tonne_{product}$).[176,177] Of these, criteria such as catalyst activity and their consumption are of great interest. Considering a catalyst density of 1 tonne per m^3 for a catalytic fixed bed reactor, the threshold activity of the catalyst should be greater than 6 mmol g^{-1} h^{-1}. Interestingly, most of the newer-generation catalysts demonstrate higher rates. However, it should be noted that no more than 1 kg of catalyst should be consumed to generate 1 tonne of ammonia, and therefore, such criteria can only be met if the catalyst remains stable on stream for at least 6 months. To the best of our knowledge, such stability reports for the catalyst are missing, and hence, nothing conclusive can be stated on their potential as an industrial catalyst. Additionally, some of these catalysts such as electride-supported and amide catalysts are prone to deterioration under moisture and could also agglomerate, which adversely affects the catalytic activity.

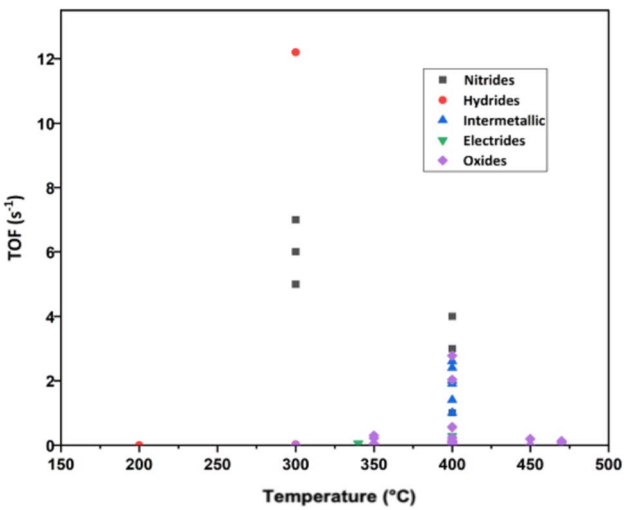

Fig. 25 Scatter plot showing the TOF of the thermal catalyst as a function of temperature for ammonia synthesis. Here, the maximum pressure considered is 0.9 MPa.

Fig. 25 summarizes the TOF of different classes of thermal catalysts. The TOF value describes the number of catalytic cycles per active site and time. It is determined under conditions for true kinetic control. The variation in TOF also indicates the structure sensitivity of ammonia synthesis. Fig. 25 shows that the TOFs reported with hydrides such as BaH_2–BaO/Fe/CaH_2 catalysts are significantly greater (12.2 s^{-1}) than those of the other reports. Moreover, the ammonia synthesis rates are 5.5 mmol g^{-1} h^{-1}, under 0.9 MPa and 300 °C. Under such mild reaction conditions, BaH_2–BaO/Fe/CaH_2 has positive orders for N_2 and H_2, possibly indicating relatively high efficiencies at lower temperatures.[26,84] Similarly, other nitrides such as Ca_3CrN_3H catalysts also exhibit higher TOF values.[44] In the same line, some of the Ru-supported *R*ScSi silicides (*R* = La, Ce, Pr, Nd, Sm, and Gd) exhibit TOF > 2.0, which was attributed to the easy dissociation of the nitrogen molecules with possible N-species storage by the *R*ScSi support and hydrogen in NH_3 comes from the gas-phase H_2 and not particularly from the hydride phase.[99]

Moreover, under other conditions with less efficient catalysts, the TOF values are one or even three orders of magnitude less than 1.0 and the corresponding order of NH_3 is often negative. Notably, any enhancement in efficiency can be possible by altering the synthesis procedures to improve the density, dispersion, and accessibility of active sites in these catalytic materials. In contrast, other catalysts such as oxides and intermetallics displayed mediocre to high efficiency at 400 °C. However, at elevated temperatures (>400 °C), the efficiencies of oxide catalysts are significantly lower. Interestingly, under such conditions, a considerable value of TOF (>2.0 s^{-1}) has been reported, which appreciates the development in the strategies to facilitate nitrogen dissociation and readily enable adsorption–desorption of hydrogen molecules. It should be emphasized that scalable synthesis methods for catalysts are vital to maximize and retain the contact between the catalyst and co-catalyst/support for prolonged lifetime in pursuit of more efficient catalysts. Hence, focus should be driven to explore porous, high surface area catalyst supports and synthesis strategies to enhance the metal–support interactions that would render a substantial increase in the catalytic efficiency. Therefore, the proliferation of small-scale mild-conditions ammonia synthesis facilities at a localized site can be possible only after the detailed techno-economic analysis of the developed catalysts and their performance as well.

5. Non-thermal plasma (NTP)-assisted ammonia synthesis

5.1 Introduction

With the advent of new technologies in the field of ammonia synthesis, synthesis *via* NTP has gained significant attention. Mild conditions with low-cost input as well as low energy

consumption make non-thermal plasma an attractive route for the production of ammonia. Well known as the "fourth state of matter", plasma is an ionized gas which possesses electrical neutrality. In NTP, the temperature of the gas is nearly equal to the room temperature while that of the electrons reaches values as high as 10 000–100 000 K (1–10 eV), unlike thermal plasma in which the gas and electron temperatures are identical. In the case of NTP, input energy is transferred to the electrons selectively. These electrons collide with the molecules of the reacting gases to produce new species (excited state atoms, reactive radicals, ozone, *etc.*). These species can assist the dissociation of molecules and can thus initiate physical and chemical reactions under mild conditions. Thus, NTP holds potential to be an effective technique for ammonia synthesis.

Direct production (without the use of catalyst) of ammonia using NTP is possible as it dissociates the reactants, N_2 and H_2, which sequentially combined to produce ammonia. On employing a catalyst, the effect of interaction of the active species produced during the dissociation with the catalyst can lead to promotion of ammonia synthesis. In case of NTP, the initial step for ammonia synthesis is the dissociation and ionization of nitrogen and hydrogen. Followed by this is the generation of radicals due to collision of the elements present in the plasma region.[178] It should be noted that the dissociation of N_2 is the rate-determining step here. The NH radicals formed in the process act as precursors for ammonia synthesis. The electron-as well as vibration-excited reactions along with the radicals absorbed on the surface play an important role in the NTP-assisted ammonia synthesis. The reactions occurring in the gas phase along with the those in the surface adsorption phase are as follows:[178]

$$e + N_2 \rightarrow e + 2N \quad (17)$$

$$N + H_2(v) \rightarrow H + NH \quad (18)$$

$$N + surf \rightarrow N(s) \quad (19)$$

$$H + surf \rightarrow H(s) \quad (20)$$

$$NH + H(s) \rightarrow NH_2(s) \quad (21)$$

$$NH_2(s) + H(s) \rightarrow NH_3 \quad (22)$$

Here, 'surf' denotes the adsorption surface of the catalyst, 's' shows the species adsorbed on the catalyst surface and 'v' shows the molecule excited due to vibration. The synergy between species adsorbed in the gas phase and that in the gas phase can be represented by the following equations:

$$NH + H(s) \rightarrow NH_2(s) \quad (23)$$

$$NH_2(s) + H(s) \rightarrow NH_3 \quad (24)$$

The reactions occurring in the gas phase are the source of excited state molecules which then lead to surface adsorption reactions for the formation of NH_3 (or NO_x). The N, H and NH_x radicals generated in the process stay on the catalyst surface. While in the gas phase, N_2 dissociates on electron excitation and forms atomic nitrogen, which then reacts with the hydrogen molecules excited by vibration to generate NH radicals. These NH radicals react with H atoms present in the gas phase or those on the surface of the catalyst to produce ammonia.

NTP can also be used for pre-treatment of the catalyst used for ammonia synthesis. Plasma can be used to generate doping and defects on the surface of the material keeping the nanostructures unaffected. These defects can be created by generating nitrogen and oxygen vacancies, by etching of the catalyst or by modification of the substrate.

5.2 Types of plasma discharge

Within NTP, there are various types of discharges that have been employed to facilitate the ammonia synthesis reaction, namely:

(i) Glow discharge
(ii) Gliding arc discharge
(iii) Microwave discharge
(iv) Radiofrequency discharge
(v) Dielectric barrier discharge (DBD)

Each one of the above-mentioned discharges calls for a unique reactor setup with many innovative changes having been made over the past few decades. The history and development of catalysts for the aforementioned types of discharges have been discussed in detail in a recent review article.[179] However, the most commonly used reactor in the recent times, not just for ammonia synthesis but also for most of the NTP-assisted catalytic reactions, is the DBD reactor which we will discuss about in the subsequent section.

5.3 Dielectric barrier discharge

A dielectric barrier discharge (DBD) is the most widely used type of plasma discharge with most of the recent studies on plasma assisted ammonia synthesis being conducted in a DBD reactor. It was first used by Siemens in 1857 for ozone generation and had long been known as ozone production discharge. It is also called a silent discharge because it is inaudible.

In a DBD, electric discharge is generated between two electrodes separated by at least one layer of an insulating dielectric barrier, upon application of a high AC voltage. One of the electrodes could also be covered in the insulating dielectric material so as to achieve this separation. The purpose of the dielectric is to limit the current and prevent rapid or excessive discharge, resulting in a discharge that is arc-free, preventing the heating of the gas.[180] A few common materials that are used as dielectrics are glass, quartz, ceramics and polymers such as polycarbonate (PC) and polytetrafluoroethylene (PTFE).[181] Discharges are produced when the electric field around the electrodes is high enough, but they get accumulated on the dielectric material that is separating the electrodes. The accumulation of charge carriers on the dielectric generates an electric field that opposes the electric field induced by the external AC voltage. Hence, the discharge is observed as many small plasma filaments of duration in the order of

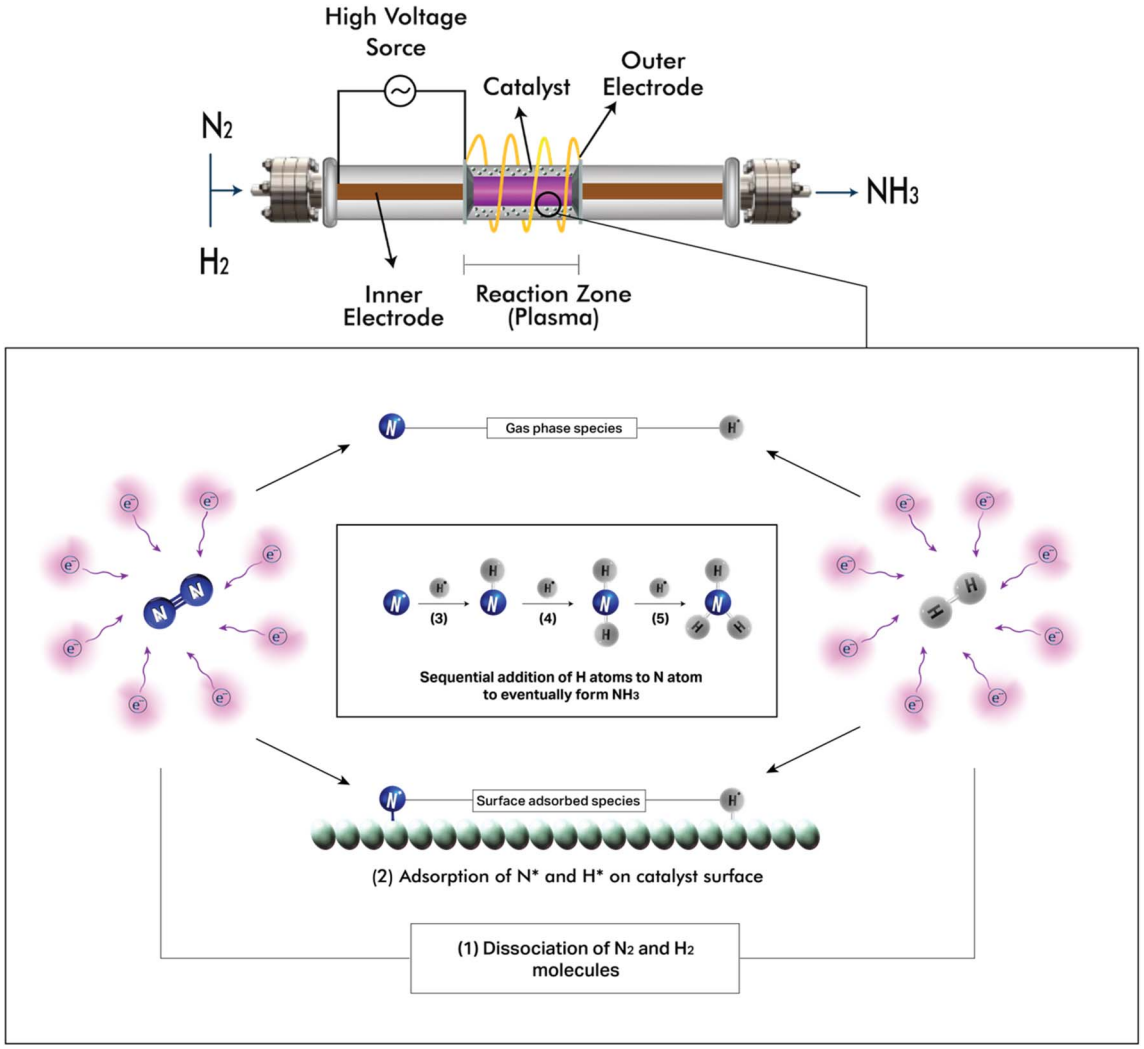

Fig. 26 Schematic of a DBD reactor and the underlying mechanism for ammonia synthesis using NTP.

nanoseconds.[182,183] Most of the chemical reactions associated with a plasma discharge occur in these filaments or "micro-discharges".[180] The schematic of a DBD reactor for ammonia synthesis and the corresponding reaction mechanism are shown in Fig. 26.

While a lot of geometric modifications of DBD have been done, they can broadly be classified as volume DBD (VDBD) and surface DBD (SDBD).[182] In a VDBD, discharge occurs in the space between the dielectric and the grounded electrode, *i.e.* the gap between the electrodes is not entirely filled with the dielectric material. In the case of SDBD, the gap between the electrodes is filled with the dielectric, the discharge is limited to the surface of the dielectric and is generally dense as compared to VDBD. DBD is useful for the treatment of temperature sensitive materials since the temperature of the gas and ions is near ambient.[183] An arc discharge is hard to control and may also damage the electrode. DBD, however, can easily be operated at atmospheric pressure, has the potential to be scaled up to industrial scale and also offers a lot of versatility with regard to its configuration, enabling us to tailor the design to suit our needs.[184] In 1969, Eremin *et al.* published the first article on the use of DBD for ammonia synthesis.[185] Since then, a number of studies have been conducted in this domain, a few of which have been talked about in the subsequent section.

Below is the updated table adapted from the review paper of Gharahshiran *et al.*,[47] which outlines the major breakthroughs in catalytic ammonia synthesis using a DBD reactor:

Various routes of catalyst synthesis were used to achieve the optimization of metal dispersion, stability, and catalytic efficiency. γ-Al_2O_3,[186] MCM-41,[187] and Ru/L-MgO[188] were synthesized using an incipient wetness impregnation technique, in which the metal precursor salts were deposited onto supports for precise control of metal loading and uniform metal distribution.

Synthesis of SBA-15 (ref. 189) by a sol–gel-assisted synthetic method provided control over the pore structure and a high surface area. Non-porous silica (NP-SiO_2) and fumed silica (EH-5) were used as comparative supports. The sol–gel method involves hydrolysis and condensation of a silica precursor in the presence of a templating agent under acidic or basic conditions.

Table 9 Catalysts used for NTP-assisted ammonia synthesis using a DBD reactor (adapted from the review paper of Gharahshiran *et al.*)[47]

S. no.	Catalyst	Plasma conditions	H_2/N_2 ratio	Total flow rate (mL min^{-1})	Ammonia yield (%)	Ammonia energy efficiency (g-NH_3 kW^{-1} h^{-1})	Energy consumption (MJ mol^{-1})	Catalyst synthesis method	Ref.
1	Al_2O_3	18.3 kHz, 0.42 kV, 1 W	0.5	22.5 (20 vol% He)	0.03	N/A	N/A	Incipient impregnation method	186
2	Al_2O_3	50 kHz, 6 kV	1	100	1.2	N/A	N/A	Conventional impregnation method	195
3	γ-Al_2O_3	21 kHz, 46.7 W	3	400	0.54	1.05	N/A	—	196
4	MgO	21 kHz, 46.7 W	3	400	0.48	0.94	N/A	—	196
5	Alkaline γ-Al_2O_3	24.25 W	3	100	N/A	6.58	9.3	—	194
6	SBA-15	20–23 kHz, 8.6 kV, 15 W	3	25	N/A	4.6	N/A	Sol–gel method	189
7	Zeolite 5A	7.5 kV, 13.3 W	1	25	N/A	15.5	3.95	—	197
8	PZT	3 kV	1	38.3	2.8	0.9	136	—	198
9	PZT	5.5 kV	3	11.5	0.5	0.75	81.6	—	199
10	ZIF-8	20–23 kHz, 8.6 kV, 15 W	3	25	N/A	1.9	N/A	—	189
11	Cu wool	5 kV	1	100	3.5	3.3	18.5	Electroless plating method	200
12	Au wool	128.7 W	1	100	N/A	0.58	N/A	—	201
13	CoLa/Al_2O_3	23.5 kHz, 51 W	1	100	0.9	N/A	77	Wet impregnation method	202
14	Rh/γ-Al_2O_3	8 kV, 24 W	0.5	100	1.43	0.94	65	Wet impregnation method	203
15	Ru/alumina membrane	4.5 kV, 127 W	3	40	4.36	0.37	163.9	—	204
16	Ru/alumina membrane	4.5 kV, 127 W	3	30	4.62	0.4	154.7	—	190
17	Ru/alumina	7.5 kV	3	1000	0.05	1.9	32.2	—	—
18	Ru/L-MgO	9.2 kHz, 60 W	0.5	300	4	1.29	N/A	Incipient impregnation method	188
19	Ru/activated carbon	13.3 W	3	100	N/A	0.72	85	Ultrasonic-enhanced impregnation method	205
20	Cs–Ru/MgO	6 kV	3	4000	2.41	2.3	26.6	Impregnation method	206
21	Ru–Mg/alumina	5.4 kV	4	2000	2.55	35.7	1.7	Impregnation method	207
22	Ru/Si-MCM-41 with Cs, K, Ba as promoters	5 kV	1	N/A	N/A	1.7	3.6	Liquid impregnation method	208
23	Ni/Al_2O_3	12 kV, 25.1 W	2	56	N/A	0.56	N/A	Incipient impregnation method	209
24	Ni/Al_2O_3	10 W	2	100	2	0.89	68.9	—	210
25	Ni/MCM-41	9.2 kHz, 9.7 kV, 40 W	3	40	5.3	1.2	N/A	Impregnation method	187
26	Ni/LaOF	7.87 kHz, 13 W	3	25	N/A	2.7	N/A	Hydrothermal method	191
27	Co–Ni/Al_2O_3	30.81 W	1	200	N/A	0.83	N/A	Incipient impregnation method	211
28	Ni–Mg0.02/SBA-15	9.5 kV	1	20	N/A	1.05	N/A	Doping and incipient impregnation method	192
29	Ni/SiO_2	13.75 kV, 13.79 W	1	50	0.49	8.08	N/A	Incipient wetness impregnation	212

The process begins with the formation of a colloidal sol, where silica nanoparticles are dispersed in a liquid. As the reaction proceeds, these nanoparticles undergo condensation, forming a gel-like network. The template is removed by controlled drying and calcination, resulting in a porous silica structure such as SBA-15, which has a high surface area and tunable pore sizes.

The anodization and impregnation method was used to design Ru/alumina tubular membrane catalysts[190] that had enhanced porosity and sufficiently high gas permeability. In this method, an aluminum substrate undergoes electrochemical oxidation (anodization) in an acidic electrolyte, resulting in the formation of a porous alumina (Al_2O_3) layer with well-defined nanochannels. This enhances the surface area and porosity. The porous alumina is then impregnated with a ruthenium (Ru) precursor solution, allowing Ru to be uniformly distributed within the pores. Subsequent drying, calcination, and reduction steps convert the precursor into active Ru nanoparticles, resulting in a Ru/alumina tubular membrane catalyst with improved gas permeability and catalytic performance.

In another work, Ni/MCM-41 (ref. 187) catalysts were synthesized by an impregnation method, which allowed the adjustment of Ni on the surface thus affecting surface accessibility and stability. Ni was loaded on MCM-41 and SiO_2 supports using a variety of deposition methods. MCM-41 was prepared by a sol–gel process with CTAC, TEOS, and NH_3 H_2O, and calcined at a temperature of 550 °C. After that Ni was deposited at three different locations: within the mesopores (Ni/MCM-in), outside the framework (Ni/MCM-out), and integrated in the framework (Ni/MCM-both). Ni/MCM-in was prepared by impregnating preformed MCM-41 with a solution of $Ni(NO_3)_2$. All these catalysts were calcined at 550 °C and reduced in Ar/H_2 at 750 °C before use for plasma-catalytic ammonia synthesis.

Hydrothermal synthesis was used for the production of Ni/LaOF[191] catalysts with high crystallinity and uniform morphology. LaOF was synthesized by dissolving $LaCl_3 \cdot 7H_2O$, urea, and NH_4F in DI water, stirring for 30 min, and heating in an autoclave at 180 °C for 12 h. The resulting white powder was washed, dried at 60 °C, and calcined at 800 °C under argon flow.

SBA-15 modified by MgO was synthesized *via in situ* doping[192] and impregnation with Ni-loaded variants to enhance Ni–MgO interactions and catalytic performance. *In situ* doping involved dissolving the P123 polymer and magnesium acetate in HCl, adding tetraethyl orthosilicate (TEOS), stirring overnight, and hydrothermally treating at 100 °C for 24 h, followed by washing, drying, and calcination at 550 °C. SBA-15 was also modified with MgO using the impregnation method. Ni–Mg/SBA-15 catalysts (5 wt% Ni) were then prepared by impregnating Mg/SBA-15 with $Ni(NO_3)_2$, followed by drying and calcination at 550 °C for 6 h.

As can be observed in Table 9, γ-Al_2O_3 has been explored as a support for catalysts in NTP-assisted ammonia synthesis in several studies. Notably, Wang *et al.* were among the first to compare different transition metals supported on alumina for their catalytic activity in NTP-assisted ammonia synthesis. Ni/Al_2O_3 gave the best synthesis rate of 390 μmol g^{-1} h^{-1} and a yield of 0.77%, and Fe barely added to the activity of alumina alone, with Cu giving an intermediate activity. The low activity of Fe was attributed to the fact that it had stronger adsorption of N_2 species, which increased the barrier for hydrogenation, thereby resulting in a lower rate of ammonia synthesis. The lower metal–N bond strength in case of Ni resulted in an increased ammonia yield, as a weaker M–N bond strength indicates a lower rate of ammonia dissociation.[193] Zhu *et al.* investigated the effect of pH on the activity of γ-Al_2O_3 pellets in a packed bed dielectric barrier discharge reactor and found that ammonia synthesis followed the order of alkaline γ-Al_2O_3 > neutral γ-Al_2O_3 > acidic γ-Al_2O_3 > blank tube.[194]

Iwamoto *et al.* compared the catalytic activities of Ni, Fe and Ru supported on alumina, and also tested alumina alone. Conventional wetness impregnation was used to prepare the metal loaded catalysts. Surprisingly, it was found that alumina by itself gave a better ammonia yield as compared to alumina loaded with Fe and Ru, indicating that these metals decreased the activity of alumina. Ni/γ-Al_2O_3 had the best catalytic activity with an ammonia yield of 6.3% at an applied voltage of 6.0 kV, a residence time of reactant gases of 0.12 min, and $P_{H_2}/P_{N_2} = 1$. It was found that NiO and $NiAl_2O_4$ were generated on Al_2O_3, and the NiO species readily reduced to Ni in the plasma reaction, which served as active sites.[195] Winter *et al.* studied the catalytic surface reactions on the γ-Al_2O_3-supported Ni and Fe, and found that the gas phase ammonia production varied as Al_2O_3 < Fe < Ni. The higher activity of Ni was attributed to the fact that it had a higher concentration of adsorbed species. It was also found that Ni favoured the adsorption of NH_x while Fe favoured the adsorption of N_2H_y.[186] Patil *et al.* also tested various catalysts supported on alumina, and found that 2% Rh/Al_2O_3 was the most efficient among noble metals and 10% Ni/Al_2O_3 was the most efficient among transition metals.[203]

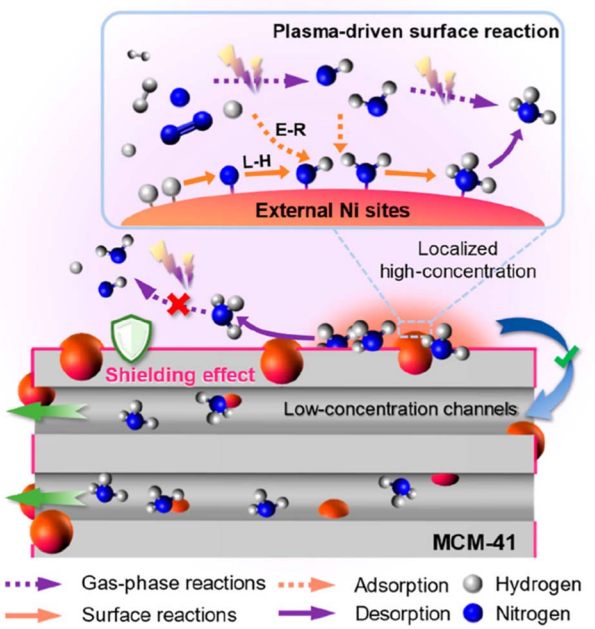

Fig. 27 Schematic of the "shielding" mechanism of MCM-41 and the reactions involved. Adapted from the work of Wang *et al.*,[187] licensed under CC BY 4.0 (https://creativecommons.org/licenses/by/4.0/).

Despite obtaining a better rate with noble metals, Ni has gained limelight due to its lower cost. A number of studies for plasma-catalytic ammonia synthesis hence used Ni-based catalysts. Gorky *et al.* studied the effect of the size of Ni nanoparticles on the catalytic activity. Silica was chosen as the support over alumina due to its inert nature, so that the actual effect of size of NPs could be studied without having to worry about the interaction with the support. Two sets of catalysts were prepared, one using wetness impregnation and the other using surface organometallic grafting (SOG). The SOG catalyst showed a higher rate, with the smallest size of nanoparticles giving the highest rate of ammonia production.[212] One of the major challenges in NTP-assisted ammonia synthesis is the plasma-assisted decomposition of the desorbed ammonia. Shah *et al.* used zeolite 5A as a support based on the hypothesis that its surface negative charge might enhance nitrogen dissociation. Using such inert porous packing improved the ammonia formation rate due to the *in situ* adsorption of ammonia by the packing. Zeolite 5A also promoted the formation of micro discharges and changed the reactor's voltage–current characteristics, which further helped in improving the ammonia yield.[197]

Although the use of such catalysts improved the ammonia synthesis rate, reverse reaction, *i.e.* ammonia decomposition remains a challenge. To address this issue, Wang *et al.* proposed a mesoporous MCM-41 support with a controlled deposition of nickel nanoparticles, with the aim of developing a "shielding protection" catalyst.[187] Ni was deposited on the external surface of MCM-41 to expose the catalyst surface to plasma-activated reactant gases which enhanced the plasma-catalytic interactions and improved the ammonia production rate. An illustration of the proposed mechanism can be found in Fig. 27.

After the addition of hydrogen to the nitrogen atom, the resulting NH_3 molecule desorbed from the surface of Ni catalyst and diffused from the external surface of MCM-41 (where there is a relatively high concentration of ammonia) to its mesopores (low-concentration channels). Due to the absence of plasma in these mesopore channels, the reverse reaction, *i.e.* decomposition of NH_3, was inhibited, resulting in a higher ammonia yield. Moreover, the Ni NPs dispersed over the external surface of MCM-41 provided good accessibility and enhanced the activation of N_2 molecules, resulting in an exceptional NH_3 yield of >5%.

Ru is an excellent thermal catalyst for ammonia synthesis, and therefore, it has also been widely studied for NTP-assisted ammonia synthesis. Cheaper Ni based catalysts have come into the picture recently, but Ru has been a material of interest in this regard even before. The work by Kim *et al.* is one of the earliest ones to report a Ru-based catalyst supported on alumina. They have reported a Mg-promoted Ru/γ-Al_2O_3 catalyst and performed the experiment under N_2-rich conditions, perhaps due to the fact the Ru faces the issue of hydrogen poisoning. The presence of RuO_2 was found to be beneficial for ammonia formation, but it was getting reduced by H radicals, due to which base metals were introduced as promoters to protect RuO_2 from rapid reduction.[207] Peng *et al.* reported Cs promoted Ru supported on activated carbon, again in a nitrogen-rich environment, confirming that a N_2-rich environment is more suitable for ammonia synthesis using Ru-based catalysts due to the relative difficulty in nitrogen dissociation.[206] Xie *et al.* studied the effect of various parameters on the rate of ammonia formation using a Ru/L-MgO catalyst. They found that the ammonia yield increased with the increase in the total gas flow rate, discharge power and discharge temperature.[188] Hu *et al.* also conducted a study on the catalytic activity of a series of metals supported on activated carbon. They found that the order of NH_3 concentration is as follows: Ru/AC > Co/AC > Fe/AC > Ni/AC. This finding was contrary to the high activity of Ni as compared to Fe and Co, when alumina support was used. The enhancement in rate was attributed to the basicity of the metal/AC catalysts that occurred as a result of the incorporation of the active metal onto the activated carbon support.[205]

Recently, our group has investigated the use of transition metal-loaded boron-doped graphitic carbon nitride (BCN) for NTP-assisted ammonia synthesis under near ambient conditions. The empty orbitals in the boron atom aid in the activation of the inert nitrogen molecule, while the surface vacancies in graphitic carbon nitride attract electrons of surrounding carbon atoms, forming electron-deficient sites which further enhance N_2 activation. The strong acidic sites in BCN impede the desorption of ammonia gas which is basic in nature, hence Fe and Co were loaded onto BCN to weaken these acidic sites. Among the tested catalysts, Co–BCN demonstrated the highest ammonia synthesis rate of 2.48 mmol g^{-1} h^{-1}, corresponding to an energy efficiency of 2.09 g-NH_3 kW h^{-1}, which was around 2.89 times higher than that of plasma alone. It was also found that the ammonia formation reaction occurred *via* a dual mechanism involving both Langmuir–Hinshelwood (L–H) and Mars van Krevelen (MvK) pathways. The existence of MvK mechanism was confirmed by subjecting the Co–BCN catalyst to pure N_2 and H_2 flows and passing the effluent gas in a solution of Nessler's reagent. No colour change was detected under pure N_2; however, under pure H_2 the solution formed a dark-brown precipitate, indicating that the lattice nitrogen atom in BCN underwent hydrogenation to form ammonia.[213]

Non-thermal plasma-assisted ammonia synthesis therefore represents a promising alternative to traditional methods, primarily due to its ability to produce ammonia under ambient temperature and atmospheric pressure. Unlike conventional thermal catalysis, which typically requires high temperatures (around 400–500 °C) and pressures (15–30 MPa) to activate nitrogen molecules, plasma-assisted synthesis operates under non-equilibrium reaction conditions. This allows for the activation of nitrogen N_2 at much lower temperatures, where the energy input is directed towards exciting electrons, ions, and radicals, creating a highly reactive environment that facilitates N_2 dissociation. Consequently, plasma-assisted ammonia synthesis can achieve higher ammonia yields compared to thermal catalysis, making it a potentially more energy-efficient method for ammonia production, especially if scaled up. The non-equilibrium nature of the plasma also allows for a broader range of reaction pathways that can enhance nitrogen activation, offering flexibility in optimizing ammonia synthesis. The

plasma state provides a high density of reactive species such as electrons, ions, and excited molecules, which are highly effective in overcoming the strong triple bond of nitrogen, making the process more efficient in terms of both energy and reactant utilization.

However, despite these advantages, non-thermal plasma-assisted ammonia synthesis faces several challenges that need to be addressed before it can be commercially viable. A primary concern is the high-power consumption associated with generating and maintaining the plasma. The energy required to sustain the plasma can significantly increase operational costs, particularly when scaling up the process for industrial-scale ammonia production. Additionally, the design of plasma reactors capable of continuously producing ammonia remains a significant hurdle. Current reactor designs, while effective at the laboratory scale, may not be optimized for continuous operation, limiting the potential for sustained, large-scale ammonia synthesis. Furthermore, the plasma reactor must ensure a homogeneous distribution of plasma across the reaction zone to maintain high reaction rates, which can be difficult to achieve with current designs.

To overcome these challenges, further research is required to improve the energy efficiency of plasma generation, such as optimizing power supply systems and plasma reactor configurations. Additionally, the development of new reactor designs that allow for continuous operation while maintaining plasma stability and effective heat management will be crucial for scaling up this technology. Advances in plasma diagnostics and monitoring will also aid in fine-tuning the process conditions to maximize ammonia yield while minimizing power consumption. With these improvements, non-thermal plasma-assisted ammonia synthesis has the potential to revolutionize ammonia production, offering a more sustainable and energy-efficient alternative to traditional Haber–Bosch processes.

6. Electrochemical ammonia synthesis

6.1 Introduction

The compulsion to enhance the energy efficiency of the industrial ammonia production process, and the necessity to make it environmentally compatible by using renewable energy sources and eliminating the use of fossil fuels as H_2 sources, has directed the attention of researchers towards electrochemical ammonia synthesis. Electrochemical ammonia synthesis involves the use of an electrochemical cell consisting of a cathode, an anode and an electrolyte to produce ammonia using a nitrogen source (nitrogen, nitrate or nitric oxide) and a hydrogen source (water). Apart from the carbon neutrality of this method, the modularity of the apparatus involved and the ability to control the reactions by adjusting external parameters (such as applied voltage) particularly distinguish it from the conventional mode of ammonia synthesis.

Lately, the HB process is being integrated with a water electrolyser to reduce the dependence on fossil fuels for sourcing hydrogen. The direct N_2 reduction process using an electrochemical cell has lower capital costs as compared to this combined system. Therefore, due to a lower capital cost (for green ammonia production) and its modular setup, electrochemical ammonia synthesis is conducive to small scale operations, facilitating on-demand, on-site NH_3 production.[214] While Haber's discovery in the early 20th century brought light to ammonia, it was in fact in 1807 that ammonia was first synthesised, electrochemically, by Humphry Davy. Davy is well known in the field of electrolysis due to his discovery of most of the alkali and alkaline earth elements. When he electrolysed distilled water in the presence of air (of which N_2 is a major constituent), he found small traces of ammonia. The same experiment when repeated in vacuum (no nitrogen source) produced only oxygen and hydrogen. Not much was made of this result, until much later in 1922 when Friedrich Fichter and Richard Suter repeated his experiments by electrolysing dilute sulphuric acid using platinum electrodes at a pressure of 200 atm in a nitrogen rich environment. The formation of ammonia was confirmed, however only at a rate of 0.3 mg min^{-1}, hence it was believed that the electrochemical synthesis of ammonia was not going to be economically viable.[215] It was only in the late 20th century, when the increasing awareness about the negative impact of the HB process on our planet led to the exploration of alternative pathways for ammonia synthesis, that the electrochemical method gained limelight. Since then, this field has seen a massive development, with the discovery of various electrocatalysts, electrolytes and improvement in the electrochemical cell design. These efforts have significantly improved the reaction rate and selectivity, making the entire process more scalable and cost-effective.

However, there remain certain challenges that we still need to overcome to fully unlock the potential of electrochemical ammonia synthesis. In this section of the paper, we will briefly discuss different routes for the electrochemical synthesis of ammonia and the catalytic advancements made in this field over the recent years.

6.2 Pathways of electrochemical ammonia synthesis

6.2.1 Nitrogen reduction reaction (NRR). The electrochemical nitrogen reduction reaction (NRR) is perhaps the most widely used electrochemical ammonia synthesis pathway. In this method, the N_2 molecule is typically adsorbed on the surface of an electrocatalyst and reduced to NH_3 at the cathode using the protons obtained from the oxidation of water at the anode (Fig. 28). The reactions involved are as follows:

$$\text{Anode: } 3H_2O \rightarrow 3/2O_2 + 6H^+ + 6e^- \quad (25)$$

$$\text{Cathode: } N_2 + 6H^+ + 6e^- \rightarrow 2NH_3 \quad (26)$$

$$\text{Overall: } N_2 + 3H_2O \rightleftarrows 2NH_3 + 3/2O_2 \quad (27)$$

The first step in the NRR is (i) the diffusion of N_2 molecules from bulk to the interface of the electrode (catalyst) and the electrolyte. (ii) This is followed by the adsorption of N_2 onto the surface of the catalyst, where it is activated and protonated to

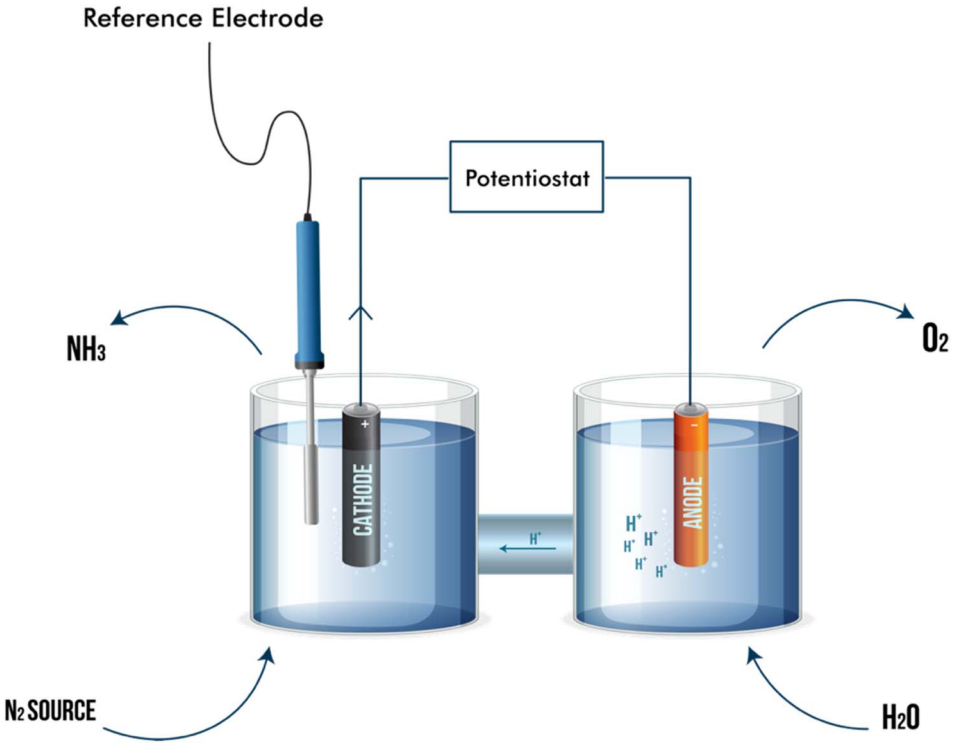

Fig. 28 Schematic of the electrochemical setup for NRR.

yield NH_3. Byproducts such as hydrazine (N_2H_4) and diazene (N_2H_2) are also formed in small amounts; a detailed discussion on this is provided in one of the subsequent sections. (iii) These products desorb from the catalyst surface and diffuse back into the electrolyte.[214,216]

Limitation in any of these steps could disrupt the desired reaction, making it necessary to design a well-suited electrocatalytic system to ensure that all the challenges associated with the above steps could be overcome. The bottleneck of NRR is the highly inert nature of the N_2 molecule. The triple bond of nitrogen exhibits a very high bond energy of roughly 941 kJ mol^{-1}, making it very hard to dissociate. The HOMO (highest occupied molecular orbital) and LUMO (lowest unoccupied molecular orbital) energy gaps of nitrogen are also very high at 10.82 eV.[4] This energy gap represents the lowest energy required for the excitation of electrons in a molecule; therefore, a higher HOMO–LUMO gap would make the compound less reactive. Nitrogen also has a low proton and electron affinity, limiting the proton–electron transfer, which makes hydrogenation very challenging. The non-polarity of nitrogen also adds to its limited solubility in electrolytes.[4]

Another obstacle is the parasitic HER (hydrogen evolution reaction), which competes with NRR and favours the reduction of H^+ over N_2.

$$\text{Hydrogen evolution reaction: } 2H^+ + 2e^- \rightarrow H_2 \qquad (28)$$

Both the HER and the NRR occur at similar potential values; however, the HER has faster kinetics mainly because it requires only $2e^-$ but NRR requires $6e^-$. Moreover, the inert nature of nitrogen molecule makes HER more favourable despite similarity in the thermodynamic potentials of both the reactions. Therefore, the HER consumes protons and electrons, reducing their availability for the NRR, thus resulting in lower ammonia production and faradaic efficiency. Faradaic efficiency (FE) is an important parameter in electrochemistry, which gives an idea about the overall selectivity of an electrochemical process. It is a ratio of the number of electrons consumed by a given electrode to the total amount of charge passed during the process. This gives us the amount of product formed relative to what would have formed if the total charge passed during the electrolysis was utilised for the desired reaction.[217] While a higher FE is a good indicator of reaction selectivity, it cannot be relied upon as the sole indicator of catalyst performance. An increase in the FE does imply that the catalyst has suitable properties to inhibit the HER, but it does not signify a higher ammonia production rate. Hence, the ammonia production rate is separately measured, normalised to the amount of catalyst used or the electrochemical surface area, in order to gain further insights into the catalyst performance.[214]

While eqn (27) gives an overview of the overall reactions, it is also necessary to understand the exact mechanism in which N_2 gets reduced to NH_3 for innovation in catalyst development and enhancing the reaction selectivity. Theoretical investigations have proposed various mechanisms to understand the NRR, among which the most widely accepted are the dissociative, associative, Mars-van Krevelen (MvK) and Li-mediated pathways. The dissociative mechanism involves the cleavage of the N_2 bond which, as discussed earlier, requires a large amount of

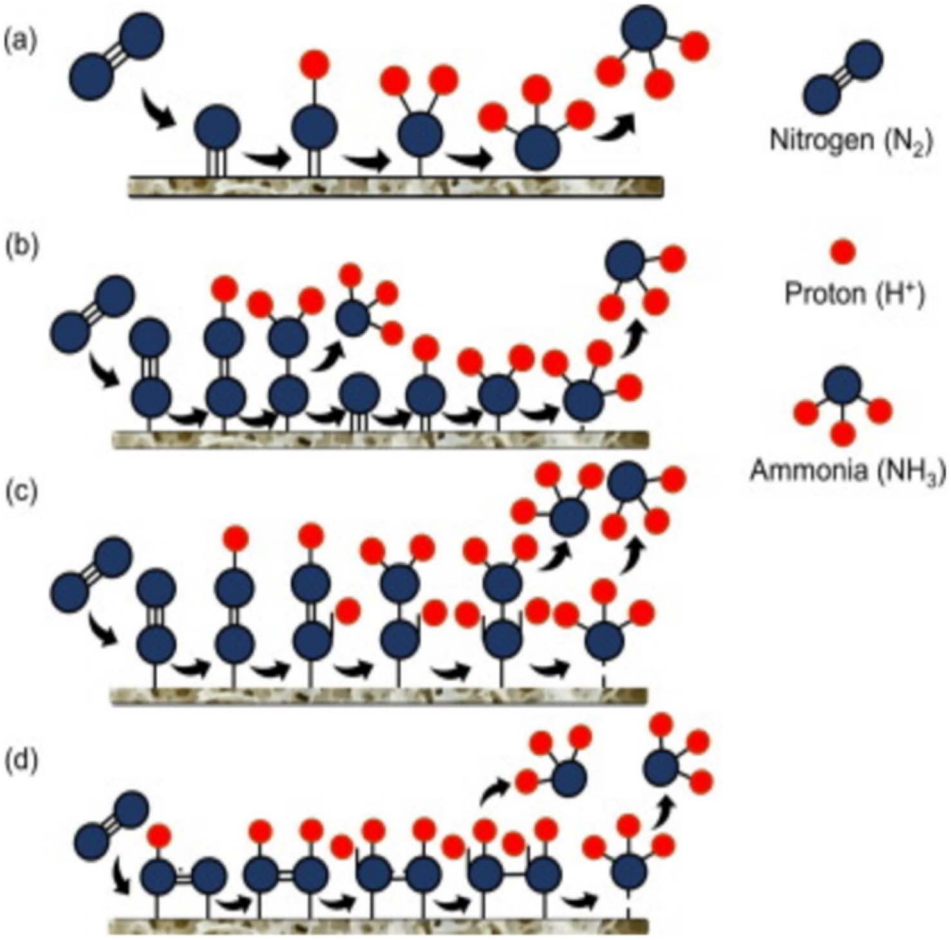

Fig. 29 Illustration of the (a) dissociative mechanism, (b) distal associative mechanism (end-on binding), (c) alternate associative mechanism (end-on binding) and (d) enzymatic associative mechanism (side-on binding). Adapted with permission from ref. 216. Copyright 2024, Elsevier.

energy. Therefore, this mechanism is often associated with processes involving harsh reaction conditions and is most commonly followed in the HB process. After adsorption on the catalyst surface, the N_2 molecule dissociates into two adsorbed N atoms (represented as *N). The *N atoms then undergo sequential hydrogenation, forming *NH, *NH_2 and subsequently NH_3. Since electrochemical ammonia synthesis is seen as a low temperature alternative to the HB process, this mechanism does not fit the purpose of electrochemical NRR as much as the other mechanisms under consideration.

Contrary to the dissociative mechanism, where the N_2 molecule is broken down into *N atoms immediately after adsorption, the associative pathway is characterised by nitrogen bond cleavage during the protonation process. Associative pathway is further categorised into distal, alternating and enzymatic pathways. In distal and alternating pathways, the nitrogen molecule is adsorbed onto the catalyst surface in the end-on mode, where only one N atom directly interacts with the active site, while the other N atom extends away from the catalyst surface. In the enzymatic pathway, the nitrogen molecule is adsorbed in the side-on mode, where both the N atoms interact with the catalyst surface (see Fig. 29).

In the distal associative pathway, hydrogenation first occurs on the nitrogen atom that is away from the catalyst surface. This gives the first NH_3 molecule, which gets desorbed from the catalyst surface, followed by the hydrogenation of the proximal nitrogen atom to give the second NH_3 molecule. After the desorption of the second NH_3 molecule, another N_2 molecule gets adsorbed in the vacant site on the catalyst surface and the same process repeats. In the alternate associative pathway, sequential hydrogenation occurs simultaneously in both the nitrogen atoms, resulting in the formation of two NH_3 molecules at the same time.

The enzymatic pathway is similar to the alternate pathway, except for the way the N_2 molecule is adsorbed onto the catalyst surface (side-on in the case of enzymatic *vs.* end-on in the case of alternate). Fig. 29 provides a good understanding of these mechanisms, along with the orientation of N_2 adsorption on the catalyst surface.

As discussed earlier, while NH_3 is the main product of the NRR, the partial protonation of nitrogen also yields diazene (N_2H_2) and hydrazine (N_2H_4) as byproducts. Diazene is unstable and decomposes to nitrogen and ammonia in the electrolyte, hence it is present in very little quantities.[214] In the case of

hydrazine, its desorption from the catalyst surface is a highly endothermic process, therefore it generally remains attached to the catalyst surface and undergoes further protonation to desorb as ammonia and is only detected in small amounts as hydrazine in the final product.[216]

The formation of these byproducts, however, can be used to predict the mechanism of the NRR. Both hydrazine and diazene can form as intermediates during the associative pathway of nitrogen reduction[218] (Fig. 29b–d). Typically, each nitrogen atom undergoes protonation thrice before desorbing as ammonia; however, it is possible that the N_2 molecule that attaches onto the catalyst surface (*via* associative pathway) undergoes partial protonation only, resulting in the formation of hydrazine or diazene. Thus, while quantification of these byproducts is not generally necessary owing to their low concentration, the detection of these byproducts may provide useful insights on the pathway followed by the catalyst for the NRR.

The Mars-van Krevelen (MvK) mechanism is perhaps one of the most effective NRR mechanisms. In the context of ammonia synthesis, it is applicable when metal nitride catalysts are used. The nitrogen atom present on the surface of the transition metal nitride catalyst acts as a reactant and undergoes reduction to NH_3. When this molecule is desorbed, it creates a nitrogen vacancy on the catalyst surface which is replenished by the feed N_2 gas, after which further NRR occurs on that site. Since the first NH_3 molecule is formed without using N_2 from the feed, it eliminates the necessity to cleave the nitrogen triple bond. The vacant nitrogen site after desorption of this molecule promotes N_2 adsorption and facilitates nitrogen reduction.[216] The schematic representation of MvK mechanism can be found in Fig. 30a.

It is worth noting that the doping of metal nitrides with heteroatoms results in improvement of eNRR activity and ammonia production. Li and co-workers found out that Fe-doped MoN_2 remarkably increased the NRR performance. The Fe atom doping weakened the metal–N bond, which helped in the activation of N_2 and NH_3 production, while the high spin state of Fe also contributed to the improvement of eNRR performance.[221] The sub layer diffusion of N onto the surface also plays a crucial role in the continuous NRR (Fig. 30f). DFT calculations revealed that the diffusion energy barrier decreased by doping Fe within the sublayer (Fes@Mn4N) from 1.12 to 0.56 eV, and there is no significant change in doping on the surface (Fet@Mn4N) (1.12 to 1.09 eV) (Fig. 30g). This is because Fe forms weaker bonds compared to Mn with N, resulting in low diffusion energy barrier.

Based on the success of oxygen evolution on cation-vacancy oxide catalysts, cation vacancy-engineered TMN electrocatalysts may lead to advances in NRR. Yang's group developed a nitrogen-doped carbon-supported MoN electrocatalyst (MV-MoN@NC).[220] They reported that varying the density of Mo

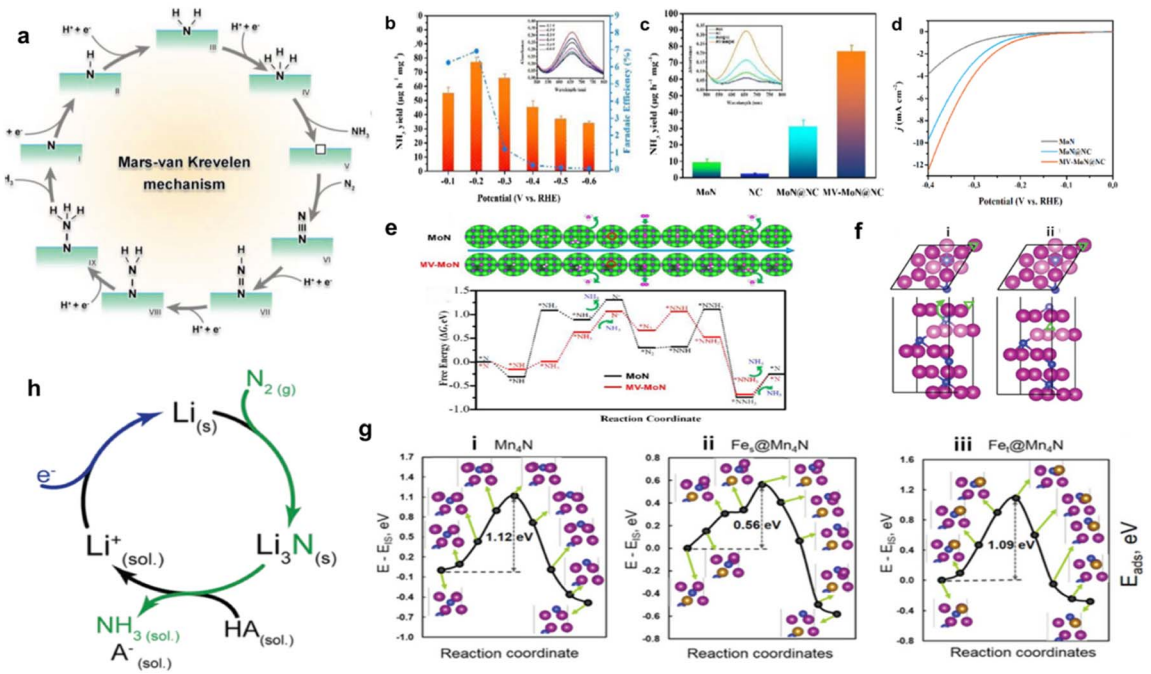

Fig. 30 (a) Schematic of the Mars van Krevelen mechanism for NRR. Adapted with permission from ref. 219. Copyright 2023, John Wiley and Sons. (b) Variation of NH_3 yield rates and faradaic efficiency (blue dashed line) with the potential for MV-MoN@NC. (c) Ammonia yield at −0.2 V *vs.* RHE for different catalysts used in the study. (d) Polarization curves for MoN, MoN@NC and MV-MoN@NC. (e) Gibbs free energy evolved for nitrogen reduction reactions at different reaction coordinates for MoN and MV-MoN. Adapted with permission from ref. 220. Copyright 2020, Elsevier. (f) Sublayer lattice nitrogen diffusion during (i) initial stage and (ii) final stage (downward green triangle: surface N vacancy; upward green triangle: sublayer N vacancy; magenta: Mn atoms; blue: N atoms). (g) Potential energy surfaces for the diffusion of nitrogen onto the surface from the sublayer (magenta: Mn; gold: Fe; green: Ni; blue: N). Adapted with permission from ref. 221. Copyright 2018, American Chemical Society. (h) Schematic representation of the mechanism of lithium-mediated ammonia synthesis. Adapted from the work of Krishnamurthy *et al.*,[222] licensed under CC-BY-NC-ND 4.0 (https://creativecommons.org/licenses/by-nc-nd/4.0/)/cropped from original.

vacancies resulted in the improvement of NRR performance. It is observed from Fig. 30d that MV-MoN@NC results in a higher current density than that of MoN@NC, which confirms that Mo vacancies contribute to the improvement of NRR performance. Moreover, when compared with the non-defect samples such as MoN, NC, and MoN@NC, it is observed that MV-MoN@NC showed a higher NH_3 yield (Fig. 30b and c). The effect of Mo vacancies has been studied by DFT calculations, and it was seen that MV-MoN@NC decreases the barrier height for the potential-determining step from 1.40 to 0.61 eV (Fig. 30e).

Lithium-mediated ammonia synthesis is an indirect method for the electrochemical synthesis of ammonia. Lithium has a large negative potential of −3.05 *vs.* SHE, which makes it a strong reducing agent. A solution of lithium salt is electrolysed to produce Li^+ ions, which get deposited as Li on the cathode. Typically, polar aprotic solvents are used to dissolve Li salts because aqueous electrolytes suffer from the competing HER and the evolution of oxygen at the cathode also causes high overpotentials due to slow reaction kinetics, impeding the NRR.[214] The highly reducing Li reacts with N_2 gas to form Li_3N, which then reacts with a proton source (such as alcohols) present in the electrolyte to form NH_3 and Li^+ (which can be cycled back to establish a continuous process).[222] The schematic representation of this process can be found in Fig. 30h. The following reactions are involved in Li-mediated ammonia synthesis:

$$3Li^+ + 3e^- \rightarrow 3Li \quad (29)$$

$$3Li + \tfrac{1}{2}N_2 \rightarrow Li_3N \quad (30)$$

$$Li_3N + 3H^+ \rightarrow NH_3 + Li^+ \quad (31)$$

6.2.2 Nitrate reduction reaction (NtrRR). Nitrate is the third most abundant freely available nitrogen source after atmospheric N_2 and organic nitrogen.[223] Nitrate ions are more reactive and get reduced more easily, resulting in lower energy consumption and operational costs as compared to NRR. Nitrates are mainly used in fertilisers due to their high solubility and biodegradability. They are also used for manufacturing explosives, as food preservatives and to manufacture drugs and medicines. Their presence in most of the essential industrial processes and human activities results in nitrate-contaminated wastewater, which poses a threat to aquatic ecosystems and human health. Therefore, electrochemical reduction of nitrates present in wastewater is a promising method to convert wastewater into a valuable resource, thus benefitting the environment.

The electrochemical nitrate reduction reaction can occur in two mechanisms:[224]

(i) The indirect pathway – the indirect nitrate reduction process occurs at a higher nitrate concentration (>1 M) in a highly acidic medium. In this process, nitrate itself does not engage in electron transfer, rather it is the electroactive intermediates such as NO_2^* and NO^+ that participate in an autocatalytic cycle.

(ii) The direct pathway – most of the studies are carried out at lower nitrate concentrations (<1 M) following the direct nitrate reduction process, which is further divided into two pathways: electron-mediated reduction and active adsorbed hydrogen reduction.

During electron-mediated reduction, N_2 and NH_3 are the main products while NO_2, NO, N_2O and NO_2^- are formed as intermediates. The first step is the adsorption of nitrate on the electrode surface, followed by its reduction to nitrite (NO_2^-), which is the rate-determining step. The intermediate NO_2^- is highly reactive and forms NO, which has an important role in determining the product distribution. It can either undergo further reduction to give NH_4^+ as the end product or it can desorb from the electrode surface to form aqueous NO. NO_{aq} forms a weakly adsorbed dimer, which gives rise to N_2O, which is further reduced to N_2.[225,226]

The following are all the reactions involved:

$$NO_{3(ads)}^- + 2H^+ + 2e^- \rightarrow NO_{2(ads)}^- + H_2O \quad (32)$$

$$NO_{2(ads)}^- + 2H^+ + e^- \rightarrow NO_{(ads)} + H_2O \quad (33)$$

$$NO_{(ads)} + 6H^+ + 5e^- \rightarrow NH_4^+ + H_2O \quad (34)$$

$$NO_{(ads)} \rightarrow NO_{(aq)} \quad (35)$$

$$NO_{(ads)} + NO_{(aq)} + 2H^+ + 2e^- \rightarrow N_2O_{(ads)} + H_2O \quad (36)$$

$$N_2O_{(ads)} + 2H^+ + 2e^- \rightarrow N_2 + H_2O \quad (37)$$

The overall reaction can be written as follows:

$$2NO_3^- + 12H^+ + 10e^- \rightarrow N_2 + 6H_2O,\ E^\circ = 1.17\ \text{V}\ \textit{vs.}\ \text{SHE} \quad (38)$$

$$NO_3^- + 9H^+ + 8e^- \rightarrow NH_3 + 3H_2O,\ E^\circ = -0.12\ \text{V}\ \textit{vs.}\ \text{SHE} \quad (39)$$

During active adsorbed hydrogen reduction, the highly reducing atomic hydrogen is used to reduce the adsorbed NO_3^- and the intermediates (NO_2^- and NO in this case) to form N–H bonds yielding NH_3 as the end product.[225,226] The reactions involved are as follows:

$$NO_{3(ads)}^- + 2H_{(ads)} \rightarrow NO_{2(ads)}^- + H_2O \quad (40)$$

$$NO_{2(ads)}^- + H_{(ads)} \rightarrow NO_{(ads)} + OH^- \quad (41)$$

$$NO_{(ads)} + 2H_{(ads)} \rightarrow N_{(ads)} + H_2O \quad (42)$$

$$N_{(ads)} + H_{(ads)} \rightarrow NH_{(ads)} \quad (43)$$

$$NH_{(ads)} + H_{(ads)} \rightarrow NH_{2(ads)} \quad (44)$$

$$NH_{2(ads)} + H_{(ads)} \rightarrow NH_{3(ads)} \quad (45)$$

Noble metals such as Pd and Pt have a high affinity for hydrogen adsorption and are hence used as catalysts for this reaction.

6.2.3 NO_x reduction reaction. NO_x is a collective representation of the nitrogen oxides NO and NO_2. These are powerful

Table 10 Electrocatalysts for the NRR

S. no.	Working electrode	Counter electrode	Reference electrode	Electrolyte	Applied voltage range (V)	Yield rate ($\mu g\ h^{-1}\ mg_{cat}^{-1}$)	Voltage at maximum yield (V)	Faradaic efficiency (%)	Voltage at maximum faradaic efficiency (V)	Catalyst synthesis method	Ref.
1	$TiO_2/Ti_3C_2T_x$MXene	Graphite rod	Ag/AgCl	0.1 M Na_2SO_4	−0.75 to −1	44.17	−0.95	44.68	−0.75	Hydrothermal oxidation	234
2	np-CuMn	—	—	0.1 M Na_2SO_4	—	28.9 $\mu g\ h^{-1}\ cm^{-2}$	−0.3 *vs.* RHE	9.83	−0.3 *vs.* RHE	Arc melting followed by chemical dissolution	235
3	Mn–TiO_2/CP	Graphite rod	Ag/AgCl electrode	0.1 M Na_2SO_4	−0.45 to −0.65	20.05	−0.5	11.93	−0.5	Normal mixing	236
4	TiO_2/JE-CMTs/CP	Graphite rod	Ag/AgCl/ saturated KCl	0.1 M Na_2SO_4	−0.45 to −0.65	20.03	−0.5	10.76	−0.5	—	237
5	1T‴ MoS_2/CC	Graphite rod	Saturated calomel electrode (SCE)	0.1 M Na_2SO_4	−0.1 to −0.5	9.09	−0.3	13.6	−0.3	Solid state reaction	238
6	C18@CoP/TM	Graphite rod	Ag/AgC	0.1 M Na_2SO_4	−0.1 to −0.5	1.44×10^{-10} mol $s^{-1}\ cm^{-2}$	−0.2 V	14.03	−0.2 V	—	239
7	C18@Fe_3P/CP	Graphite rod	Ag/AgCl	0.1 M Na_2SO_4	−0.45 to −0.25	1.80×10^{-10} mol $s^{-1}\ cm^{-2}$	−0.3 V	11.22	−0.3 V	Phosphidation followed by surface functionalization	240
8	Cu_3P NRs	—	—	0.1 M HCl	−0.1 to −0.5	18.9	−0.2 V	37.8	−0.2 V	Solvothermal synthesis	241
9	CuS-CPSs/CP	Graphite rod	Ag/AgCl	0.1 M HCl	−0.25 to −0.05	18.18	−0.15 V	5.63	−0.15 V	Hydrothermal	242
10	$PdFe_3$	Platinum foil	Ag/AgCl electrode	Saturated KCl electrolyte	−0.1 to −0.25	29.07 $\mu g\ h^{-1}\ mg_{cat}^{-1}$	−0.2 V *vs.* RHE	22.8	−0.2 V *vs.* RHE	Solvothermal followed by thermal reduction	243
11	$ZnCo_2O_4$/MgO/ $BiVO_4$	Platinum	Ag/AgCl electrode	0.1 M KOH	0.8 to 1.2 V	35.54 $\mu mol\ h^{-1}\ g_{cat}^{-1}$	1.0 V *vs.* RHE	30.99	1.0 V *vs.* RHE	Hydrothermal	244
12	$MnCo_2O_4$/MgO/ $BiVO_4$	Platinum	Ag/AgCl electrode	0.1 M KOH	0.8 to 1.2	34.03 $\mu mol\ h^{-1}\ g_{cat}^{-1}$	1.1 V *vs.* RHE	67.46	1.1 V *vs.* RHE	Hydrothermal	244
13	TiB_2 nanosheets	Platinum wire	Ag/AgCl electrode	0.1 M Na_2SO_4 (pH = 10.5)	−0.15 to −0.5	318 $\mu g\ h^{-1}\ cm^{-2}$	−0.2 V *vs.* RHE	57	−0.2 V *vs.* RHE	Surfactant-assisted exfoliation	245
14	ZrO_2 nanofibers	Graphite plate	Ag/AgCl electrode	0.1 M Na_2SO_4 (pH = 7)	−0.5 to −0.9	9.63 $mg\ h^{-1}\ mg_{cat}^{-1}$	−0.7 V *vs.* RHE	12.1	−0.7 V *vs.* RHE	Electrospinning-assisted thermal decomposition	246
15	$PdH_{0.43}$NRs	Graphite rod	Ag/AgCl	0.1 M Na_2SO_4	−0.1 to −0.5	17.53	−0.2 V	23.78	−0.1 V	Hydrothermal followed by solvothermal	247
16	NiPC	Platinum wire	Ag/AgCl	0.1 M HCl	−0.2 to −0.6	85	−0.3 V	25	−0.3 V	Solvothermal	248
17	BiOCl@$Ti_3C_2T_x$/CC	Graphite rod	Ag/AgCl	0.1 M HCL	0 to −0.2	4.06 $\mu mol\ h^{-1}\ cm^{-2}$	−0.1 V	11.9	−0.1 V	Hydrothermal	249
18	Au–Bi_2Te_3 NSs	Carbon rods	Ag/AgCl	0.1 M Na_2SO_4	−0.2 to −0.6	32.73	−0.4 V	20.39	−0.4 V	—	250
19	Fe_2O_3 NR's	Platinum foil	Ag/AgCl	0.1 M Na_2SO_4	−0.3 to −0.6	78.02 $\mu mol\ h^{-1}\ cm^{-2}$	−0.6 V	86.73	−0.4 V	Hydrothermal	251

Table 10 (*Contd.*)

S. no.	Working electrode	Counter electrode	Reference electrode	Electrolyte	Applied voltage range (V)	Yield rate ($\mu g\ h^{-1}\ mg_{cat}^{-1}$)	Voltage at maximum yield (V)	Faradaic efficiency (%)	Voltage at maximum faradaic efficiency (V)	Catalyst synthesis method	Ref.
20	MoS_2	Graphite rod	Ag/AgCl	0.1 M Na_2SO_4	−0.4 to −0.7	8.08×10^{-11} mol s^{-1} cm^{-2}	−0.5 V	1.17	−0.5 V	Hydrothermal	252
21	CuS/C	Graphite rod	$Hg/HgCl_2$	0.1 M KOH saturated with N_2	0 to −0.6	0.9 ± 0.1 μmol h^{-1} cm^{-2}	−0.2 V *vs.* RHE	11 ± 1	−0.2 V *vs.* RHE	Dissolution	253
22	CoPc NTs	Platinum wire	Ag/AgCl	0.1 M HCl N_2, Ar saturated	−0.2 to −0.6	105.52	−0.3 V *vs.* RHE	27.19	−0.3 V *vs.* RHE	—	254
23	MoB_2	Platinum plate	Ag/AgCl	0.1 M Na_2SO_4	−0.2 to −0.7	40.94 ± 0.97	−0.4 V *vs.* RHE	30.84 ± 0.81	−0.3 V *vs.* RHE	—	255
24	CoP/TM	Platinum foil	Ag/AgCl	0.2 M Na_2SO_4	0 to −0.4	47.22 μmol h^{-1} cm^{-2}	−0.2 V *vs.* RHE	88.3	−0.2 V *vs.* RHE	Hydrothermal followed by phosphidation	256
25	$TiO_2/Ti_3C_2T_x$ MXene	Graphite rod	Ag/AgCl	0.1 mol L^{-1} Na_2SO_4	−0.75 to −1	44.17	−0.95	44.68	−0.75	Hydrothermal oxidation	234
26	α-VSe_{2-x}	Graphite rod	Ag/AgCl (saturated KCl)	0.5 M $LiClO_4$	−0.2 to −0.6	65.7	−0.4	16.3	−0.4	Solvothermal	257
27	FeOOH QDs-GS/CP	Graphite rod	Ag/AgCl/ saturated KCl	0.1 M $LiClO_4$	−0.3 to −0.7	27.3	−0.4	14.6	−0.4	Mechanical mixing	258
28	MoS_2/C_3N_4	—	—	0.1 M $LiClO_4$	−0.2 to −0.6	18.5	−0.3	17.8	−0.3	Solvothermal	259
29	W-NO/NC	Graphite rod	Ag/AgCl	0.5 M $LiClO_4$	−0.6 to −0.85	12.62	−0.7 V	8.35	−0.7 V	Solvothermal	260
30	La-doped TiO_2 nanorods (**https://www.sciencedirect.com/topics/chemical-engineering/nanorod**)	Graphite rod	Ag/AgCl electrode	0.1 M $LiClO_4$	−0.65 to −0.85	23.06 μg h^{-1} mg_{cat}^{-1}	−0.7 V *vs.* RHE	14.54	−0.7 V *vs.* RHE	Hydrothermal	185

air pollutants and greenhouse gases emitted from vehicles and fossil fuel plants. They are also the constituent gases of smog and acid rain. In order to inhibit the pollution caused by these gases, selective catalytic reduction is used to convert NO_x into N_2. However, this method consumes valuable chemicals as reductants, pushing researchers to come up with alternative conversion methods. The economic value of ammonia sparked an interest to study the electrocatalytic conversion of NO_x to NH_3. Particularly, NO has been studied lately for its capability to act as a nitrogen source for electrochemical ammonia production.

Long *et al.* made thermodynamic estimations based on DFT calculations, suggesting that the NO reduction reaction (NORR) is more effective than the NRR. They have considered two different routes for the hydrogenation process – a Tafel type route and Heyrovsky type route, in both dissociative and associative pathways. The N* binding energy was chosen as a descriptor for the NORR as the adsorption energies of all the involved intermediates showed good scaling relations with it. Among 10 transition metals, copper was found to be the most optimal in the Heyrovsky mechanism. This finding was experimentally validated by using a Pt foil, Cu foil and Cu foam as electrodes. An electrochemical ammonia synthesis rate of 517.1 $\mu mol\ h^{-1}\ cm^{-2}$ with an FE of 93.5% was achieved at −0.9 V *vs.* RHE over a Cu foam, which also showed a long-term stability for 100 hours run.[227]

Wan *et al.* also performed DFT studies to determine the selectivity and activity of NORR over different catalysts.[50] Their finding was similar to that of Long *et al.*,[227] with Cu being the most active metal for NO reduction to NH_3. The hydrogenation of adsorbed NO species was predicted to be the rate determining step. At a potential of 0–0.3 V *vs.* RHE, the current density was lesser than that at a lower potential due to the limiting accessibility of adsorbed *H species; however, NH_3 was still the major product and Cu had a higher current density than other transition metals under the same conditions. At a higher potential (>0.3 V *vs.* RHE), a low barrier for N coupling with NO resulted in the formation of N_2O. Niu *et al.* screened different transition metals embedded in C_2N (N doped graphene) to come up with an efficient single-atomic catalyst for NO reduction to NH_3.[228] Based on DFT calculations, out of 23 transition metals from Ti to Au, Zr–C_2N was found to be the most promising catalyst for the NORR.

Subsequently, many studies have been conducted across the world to test a wide range of catalysts for the conversion of nitric oxide into ammonia.[229–233]

Based on the choice of electrolyte, we categorised electrochemical catalysts for ammonia synthesis into two groups. Electrolytes containing the nitrate ion (NO_3^-) or nitrate salts correspond to the nitrate reduction pathway and have been grouped into one table (Table 11).

The remaining studies have generally used Na_2SO_4 as an electrolyte as it does not interfere with the electrodes and also improves the conductivity of water, facilitating electrolysis. These studies focus on the nitrogen reduction reaction (Table 10).

The effectiveness of the electrocatalytic NRR relies largely upon adequately electrocatalyzing the activation of the very strong triple bond of nitrogen molecules for reduction to ammonia. Such electrocatalysts, which generally comprise transition metals or metal alloys, seek to promote adsorption and activation of nitrogen while suppressing side reactions. Recent advancements in the synthesis of electrocatalysts are targeted toward upgrading catalytic activity, selectivity, and stability under reaction conditions with an emphasis on nanostructuring, doping, and modification of the electronic properties of catalysts for performance enhancement. HF etching is a method that allows the preparation of $Ti_3C_2T_x$ MXenes[234] by dissolving Ti_3AlC_2 in a 40% HF solution, subsequent treatments with $NaBF_4$, and then heating to 160 °C, so that the TiO_2@$Ti_3C_2T_x$ composites are formed, providing stability and improved catalytic performance toward photocatalysis. The arc melting and selective dealloying methods allow for the preparation of $Cu_{15}Mn_{85}$ (ref. 235) alloys, where upon melting pure Cu and Mn, alloy ribbons are formed and then dealloying in HCl generates porous CuMn alloys, thus allowing fine composition control of the alloy, optimizing for catalytic reactions such as hydrogenation and oxidation. High-temperature treatment and chemical oxidation produce 1T‴ MoS_2 [238] crystals upon heating the $KMoS_2$ precursors at 1000 °C, and chemical oxidation in H_2SO_4 collectively enhances the catalytic activity *via* phase control, increasing the conductivity for hydrogen evolution reactions. 1T is the octahedral phase of MoS_2 , and the 1T′ and 1T‴ phases are formed by distortion of charge density waves of 1T MoS_2. The preparation of Fe_2O_3/CP and Fe_3P/CP[240] involves reactions between $FeCl_3 \cdot 6H_2O$ and carbon paper under high-pressure conditions, yielding highly active catalysts for electrochemical applications, such that uniform depositions of iron oxide and phosphide on carbon paper are achieved for better performances in hydrogen evolution. The solvothermal method is used to synthesize $PdFe_3$@G[243] bimetallic alloys from the solvent-based treatment of metal precursors under high pressures, allowing excellent dispersion and stability of the active phase. The hydrothermal method was used to synthesize $MnCo_2O_4$/MgO/$BiVO_4$ catalysts, which consist of reactions of nitrates with MgO/$BiVO_4$ electrodes in a Teflon autoclave, allowing precise control over the crystal structure.

Various electrocatalysts for the NO_3RR have been designed to enhance the catalytic activity towards ammonia synthesis, and CuTCNQ/CF[261] is produced by keeping copper foam immersed in TCNQ-acetonitrile solvent for surface functionalization, whereas Fe$(TCNQ)_2$/CF employs cationic exchange to form iron-based nanorods on copper foam. Electrodeposition is used for Co-based nanostructures such as $Co(OH)_2$ NAs/CFC, CoP NAs/CFC, and Co NAs/CFC,[262] allowing for the utmost degree of control over size, shape, and dispersion, which is critical for electrocatalytic performance. Metal boron organic polymers (BOPs/Pd)[264] are synthesized by reacting boron clusters with palladium precursors, yielding highly dispersed metal sites that are a prerequisite for catalytic activity. The synthesis of single-atom catalysts (SACs) such as Fe SAC[271] involves pyrolysis of a mixture of iron chloride and organic precursors with SiO_2, which leads to the isolation of iron atoms that show enhanced catalytic activity. $CoTiO_{3-x}$[280] nanofibers were synthesized by an electrospinning method with hydrogen plasma etching,

Table 11 Electrocatalysts for the NO_3RR

S. no.	Working electrode	Counter electrode	Reference electrode	Electrolyte	Applied voltage range (V)	Yield rate (μg h^{-1} mg_{cat}^{-1})	Voltage at maximum yield (V)	Faradaic efficiency (%)	Voltage at maximum faradaic efficiency (V)	Catalyst synthesis method	Ref.
1	$Fe(TCNQ)_2$/CF	Graphite rod	Ag/AgCl	0.2 M $NaNO_3$ + 0.1 M Na_2SO_4	−0.6 to −1.1	11 351.6 μg h^{-1} cm^{-2}	−1.1	85.2	−1.1	Cation exchange	261
2	CoP NAs/CFC	Graphite rod	SCE	1.0 M $NaNO_3$ and 1.0 M NaOH	−0.1 to −0.5	15.44 mol h^{-1} m^{-2}	−0.5 V *vs.* RHE	100	−0.4 V *vs.* RHE	Electrodeposition followed by phosphorization	262
3	Cu@C	Graphite rod	Ag/AgCl	0.1 M KOH + 1 mM NO_3^-	−0.1 to −0.9	469.5 μg h^{-1} cm^{-2}	−0.9 V *vs.* RHE	72.0%	−0.3 V *vs.* RHE	Solvothermal followed by pyrolysis	263
4	BC_2N/Pd	Platinum wire	Hg/HgO	0.1 M KOH + 250 mM KNO_3	−0.3 to −0.7	4325	−0.7 V	97.42	−0.3 V	Annealing	264
5	Amorphous Ru nanoclusters	Platinum disc	Ag/AgCl	5 mM Cs_2CO_3 + 500 ppm NO_3^-	−0.1 to −0.5	145.1	−0.2 V	80.62	−0.2 V	Mechanical mixing	265
6	Pd/Cu_2O octahedra	Platinum foil	$Hg/HgCl_2$	0.5 M K_2SO_4 + 50 ppm NO_3^-	−1.0 to −1.5	925.11	−0.645 V	96.56	−0.645 V	Mechanical mixing	266
7	Pd/Co_3O_4	Platinum foil	$Hg/HgCl_2$	0.5 M K_2SO_4 + 200 mg L^{-1} NO_3^-–N	−1.1 to −1.5	0.204 mmol h^{-1} m^{-2}	−1.3 *vs.* SCE	88.6	−1.3 V *vs.* SCE	Hydrothermal followed by annealing	267
8	CuPd (3 : 1) aerogels	Platinum foil	$Hg/HgCl_2$	0.5 M K_2SO_4 + 50 mg L^{-1} NO_3^-–N	0 to −1.2	784.37	−0.46 *vs.* RHE	90.02	−0.46 V *vs.* RHE	Mixing	268
9	PdBP NAs/NF	Platinum plate	$Hg/HgCl_2$	0.5 M K_2SO_4 + 100 mg L^{-1} NO_3^-–N	−0.46 to −0.86	0.109 mmol h^{-1} cm^{-2}	−0.66 *vs.* RHE	64.73	−0.66 *vs.* RHE	Chemical reduction	269
10	$NiCo_2O_4$/CC	Graphite rod	Hg/HgO	0.1 M NaOH and 0.1 M $NaNO_3$	−0.1 to −0.6	973.2 μmol h^{-1} cm^{-2}	−0.6 V	99	−0.3 V	Hydrothermal followed by annealing	270
11	Fe SAC	Platinum foil	SCE	0.1 M K_2SO_4 and 0.5 M KNO_3	−0.5 to −0.85	20 000	−0.85 V	75	−0.66 V	TM-assisted carbonization method	271
12	Polycrystalline copper	Platinum plate	SCE	0.5 M Na_2SO_4 + 0.1 M KNO_3	−0.066 to −0.466 V	101.4 μmol h^{-1} cm^{-2}	−0.266 V *vs.* RHE	93.91	−0.26 V *vs.* RHE	Electro-deposition	272
13	FePc/TiO_2 NSs	Platinum foil	Ag/AgCl electrode	0.1 M HNO_3/ 0.4 M KNO_3	0 to −0.8 V	17.4 mg h^{-1} cm^{-2}	−0.2 V *vs.* RHE	90.6	−0.2 V *vs.* RHE	—	273
14	$NiCoO_2$@Cu	Platinum foil	Ag/AgCl electrode	0.1 M Na_2SO_4 + 0.1 M $NaNO_3$	−0.5 to −0.9 V	5940.73 μg h^{-1} cm^{-2}	−0.7 V *vs.* RHE	94.2	−0.7 V *vs.* RHE	Chemical deposition	274
15	Ru–Fe_2O_3	Stone grinding rod	Ag/AgCl electrode	0.1 M $NaNO_3$ + 0.5 M Na_2SO_4	−0.5 to −0.9 V	329 μmol cm^{-2} h^{-1}	−0.9 V *vs.* RHE	72.8	−0.9 V *vs.* RHE	Impregnation	275
16	B–MoS_2	Platinum foil	Saturated Hg/ HgO	0.5 M Na_2SO_4 + 0.1 M $NaNO_3$	−0.3 to −0.8 V	10.8 mg h^{-1} cm^{-2}	−0.7 V *vs.* RHE	92.3	−0.7 V *vs.* RHE	Hydrothermal	276
17	$NiCo_2O_4$ nanowire	Graphite rod	Hg/HgO	0.1 M KOH + 0.1 M $NaNO_3$	−0.1 to −0.6	973.2 μmol h^{-1} cm^{-2}	−0.6 V	99	−0.3 V	Hydrothermal followed by annealing	270

Table 11 (*Contd.*)

S. no.	Working electrode	Counter electrode	Reference electrode	Electrolyte	Applied voltage range (V)	Yield rate (μg h^{-1} mg_{cat}^{-1})	Voltage at maximum yield (V)	Faradaic efficiency (%)	Voltage at maximum faradaic efficiency (V)	Catalyst synthesis method	Ref.
18	$ZnCo_2O_4$ nanoarray	Carbon rod	Hg/HgO	0.1 M KOH + 0.1 M $NaNO_3$	−0.8 to −0.2	634.74 mmol h^{-1} cm^{-2}	−0.8 V	99	−0.6 V	Hydrothermal followed by annealing	277
19	BCDs/$NiCo_2O_4$ nanowire	Pt foil	Saturated calomel electrode (SCE)	0.5 M K_2SO_4 + 200 ppm NO_3^-	−0.7 to −0.1	173.9 μmol h^{-1} cm^{-2}	−0.55 V	100	−0.55 V	Hydrothermal followed by annealing	278
20	Co-doped Fe/Fe_2O_3	Platinum wire	Saturated calomel electrode (SCE)	0.1 M Na_2SO_4 + 50 ppm NO_3^-	−0.5 to 1.0	1505.9 μg h^{-1} cm^{-2}	−0.95 V	85.2	−0.95 V	—	279
21	$CoTiO_{3-x}$ nanofibers	Carbon rod	Hg/HgO	0.1 M NaOH + 0.1 M $NaNO_3$	−0.6 to −1.1	30.4 mg h^{-1} mg_{cat}^{-1}	−1.1 V	92.6	−1 V	Hydrogen plasma etching treatment of electrospun $CoTiO_3$ precursor	280
22	RuO_x/Pd	—	—	1 M KOH + 0.1 M KNO_3	0 to −0.7 V	23.5 mg h^{-1} cm^{-2}	−0.5 V *vs.* RHE	98.6	−0.5 V *vs.* RHE	—	281
23	Co_1–P/NPG	Platinum foil	Ag/AgCl electrode	0.5 M K_2SO_4 + 0.1 M KNO_3	−0.5 to −0.9 V	8.6 mg h^{-1} mg_{cat}^{-1}	−0.7 V *vs.* RHE	93.8	−0.7 V *vs.* RHE	Pyrolysis	282
24	$Cu@Cu_{2+1}O$ nanowires	Platinum foil	SCE	0.5 M K_2SO_4 + 50 mg L^{-1} NO_3^-	−1.1 to −1.5	576.53	−0.545 *vs.* RHE	87.7	−0.545 *vs.* RHE	—	283
25	CuO_x/TiO_2	Graphite rod	Ag/AgCl	0.5 M Na_2SO_4 + 100 ppm NO_3^-	−0.45 to −0.95	1241.81 μg h^{-1} cm^{-2}	−0.75 *vs.* RHE	92.34	−0.75 *vs.* RHE	Electrodeposition and calcination	281
26	Co-doped TiO_2 nanosheet	Graphite rod	Hg/HgO	0.1 M NaOH + 0.1 M NO_3^-	−0.2 to −0.9	1127 μmol h^{-1} cm^{-2}	−0.9 *vs.* RHE	98.2	−0.5 *vs.* RHE	Solvothermal followed by ion exchange and annealing	284
27	$Co@TiO_2$	Carbon rod	Ag/AgCl	0.1 M PBS + 0.1 M NO_3^-	−0.3 to −1.0	800 μmol h^{-1} cm^{-2}	−1.0 *vs.* RHE	96.7	−0.7 *vs.* RHE	Hydrothermal and ion exchange followed by calcination	285
28	$FeS_2@TiO_2$	Pt	Hg/HgO	0.1 M NaOH + 0.1 M $NaNO_3$	−0.2 to −0.7	860.3 μmol h^{-1} cm^{-2}	−0.7 *vs.* RHE	97	−0.4 *vs.* RHE	Hydrothermal and ion exchange followed by calcination	286
29	Cu-doped Co_3O_4 nanowire	Pt	Ag/AgCl	0.1 M Na_2SO_4 + 500 ppm NO_3^-	−0.3 to −0.7	36.71 mmol h^{-1} g^{-1}	−0.6 *vs.* RHE	86.5	−0.6 *vs.* RHE	Hydrothermal and annealing	287
30	Co_3O_4 nanosheets with Co vacancies	Carbon rod	Hg/HgO	0.1 M NaOH + 0.1 M $NaNO_3$	−0.1 to −0.6	517.5 μmol h^{-1} cm^{-2}	−0.6 *vs.* RHE	97.2	−0.4 *vs.* RHE	Hydrothermal, annealing followed by etching	288
31	$Co_{0.5}Cu_{0.5}$	—	—	1 M KOH + 50 mM KNO_3	0.2 to −0.3	4250	−0.25 V *vs.* RHE	95	−0.03 V *vs.* RHE	Dip-coating and annealing	289
32	Ag@NiO/CC	Graphite plate	Hg/HgO	0.1 M NaOH with 0.1 M NO_2^-	−0.2 to −0.7	57 510	−0.7 V *vs.* RHE	97.7	−0.4 V *vs.* RHE	Magnetron sputtering	290

Table 11 (*Contd.*)

S. no.	Working electrode	Counter electrode	Reference electrode	Electrolyte	Applied voltage range (V)	Yield rate (μg h^{-1} mg_{cat}^{-1})	Voltage at maximum yield (V)	Faradaic efficiency (%)	Voltage at maximum faradaic efficiency (V)	Catalyst synthesis method	Ref.
33	Pd/TiO_2	Platinum plate	Ag/AgCl electrode	1 M LiCl or 1 M LiCl + 0.25 M $LiNO_3$	−0.3 to −0.8 V	1.12 mg cm^{-2} h^{-1}	−0.7 V *vs.* RHE	92.1	−0.7 V *vs.* RHE	Ion exchange followed by hydrothermal and annealing	291

producing defects that lead to increased catalytic activity. The $NiCoO_2$@Cu[274] catalysts are synthesized by growing cobalt-based MOFs on the scaffold of copper foams, while Ag@NiO/CC and Ag/CC[290] catalysts are fabricated using magnetron sputtering for precise metal loading to improve uniformity and catalytic performance. Each method presents particular advantages for controlling the composition and structure of the catalyst, which is directly correlated with enhancing catalytic performance during challenging reactions.

As discussed, the NRR faces the issue of low faradaic efficiency due to the competing HER, and the sluggish kinetics of N_2 dissociation also result in a low ammonia synthesis rate. An ideal electrocatalyst must possess an active site that has empty d-orbitals to accommodate lone pair of electrons of N_2 for adsorption. For the dissociation of the adsorbed N_2 molecule, the catalyst must be able to donate the d-orbital electrons to the anti-bonding orbitals of nitrogen. This would aid in overcoming the barrier of the N≡N triple bond dissociation. To overcome the issue of HER, the electrocatalyst must favour the adsorption of nitrogen over protons. Additionally, an electrolyte with a low proton donor activity can help solve this problem.

With respect to the NRR, we find that a lot of studies involve the use of titanium-based compounds as electrocatalysts due to its high redox activity and low toxicity. Qian *et al.*[234] used a titanium-based MXene due to its unique layered structure, hydrophilicity, flexibility and high conductivity. The MXene by itself however reduces the specific surface area and diffusivity of ions between layers due to its lamellar structure, which makes stacking very easy. In order to prevent this stacking issue, the authors used the edge Ti atoms as nucleation sites to generate stable TiO_2, which prevented microstacking and enhanced the specific surface area.

The catalyst was found to be electrochemically durable after checking the ammonia yield and FE for six consecutive cycles, which were found to be almost similar throughout (Fig. 31a). The chronoamperometry curve (Fig. 31b) shows that there was minimal current density loss after continuous electrolysis for 12 h, which further confirms that the catalyst is highly stable during the NRR. The ammonia yield remained unaffected despite varying the flow rate of N_2 (Fig. 31c), which shows that the N_2 flow does not affect the rate of the reaction. The ^{1}H NMR spectrum shows a specific double peak for $^{15}NH_4^+$ and three $^{14}NH_4^+$signals (Fig. 31d) corresponding to the $^{14}N_2$ and $^{15}N_2$ isotopes, respectively, indicating that NH_3 was generated through electrocatalytic N_2 reduction. This catalyst achieved a high faradaic efficiency (FE) of 44.68% at −0.75 V *vs.* RHE and a large NH_3 yield of 44.17 μg h^{-1} mg_{cat}^{-1} at −0.95 V.[234] Wang *et al.* also used a similar Ti-based MXene modified by BiOCl. The halide of bismuth is a well-known photocatalyst with excellent stability; however, its use as an electrocatalyst was not explored. This modified Ti MXene achieved an ammonia synthesis rate of 4.06 μg h^{-1} cm^{-2} at −0.10 V (*vs.* RHE) with a faradaic efficiency of 11.98%, which was higher than that of BiOCl and Ti MXene individually.[249] Titanium dioxide has also attracted significant attention as a promising NRR catalyst due to its abundance, non-toxicity and high thermal stability. It is also widely known as a photocatalyst and has been used in

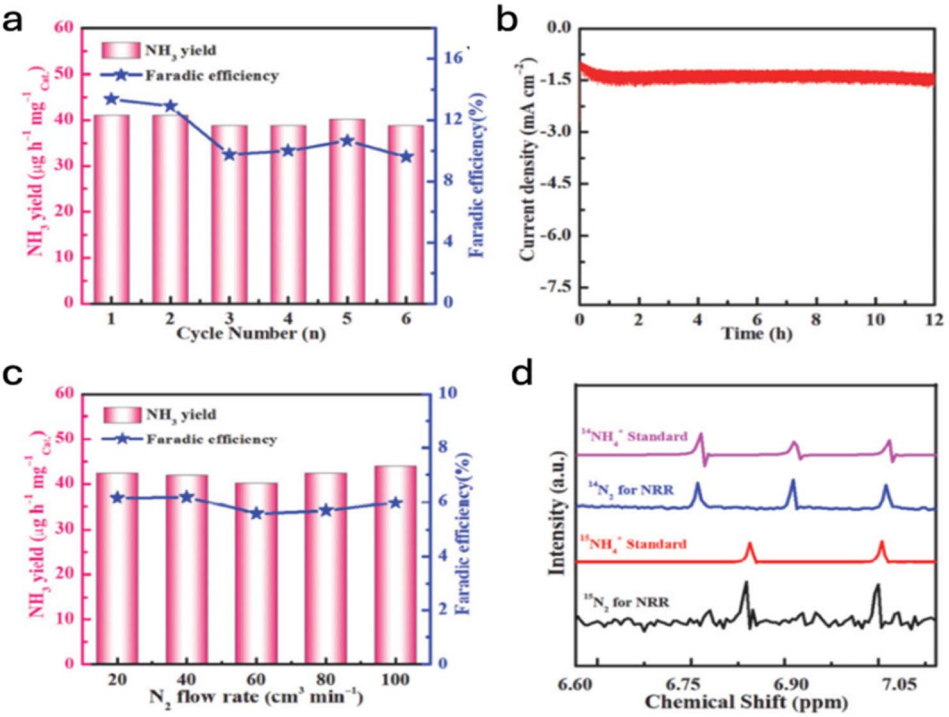

Fig. 31 (a) Ammonia yield and faradaic efficiency of the $TiO_2/Ti_3C_2T_x$ MXene at −0.95 V during six consecutive cycling tests. (b) Chronoamperometry curve of the $TiO_2/Ti_3C_2T_x$ MXene composites after electrolysis at −0.95 V for 12 h. (c) Ammonia yield and faradaic efficiency of the $TiO_2/Ti_3C_2T_x$ MXene composites under different N_2 flow rates. (d) ^1H NMR spectra of $^{14}NH_4^+$ and $^{15}NH_4^+$ yielded from the nitrogen reduction reaction at −0.95 V using $^{14}N_2$ and $^{15}N_2$ as the N_2 source, respectively. Adapted with permission from ref. 234. Copyright 2022, Elsevier.

numerous photochemical reactions after specific modifications. However, it faces two challenges as a catalyst for the NRR: the relatively low conductivity, and the low N_2 adsorption. In order to overcome these challenges, Chen *et al.* synthesized a Mn-doped TiO_2 catalyst which gave an ammonia yield rate of 20.05 μg h^{-1} mg_{cat}^{-1} and a faradaic efficiency of 11.93%, which was much higher than that of undoped TiO_2. The enhancement was attributed to the fact that Mn (after doping) introduced oxygen vacancy concentration, which enhanced N_2 activation.[236] They have also conducted another study where TiO_2 was combined with carbon microtubes derived from *Juncus effusus* (a plant commonly known as soft rush, generally found near wetlands and marshes) for the NRR. Biomass carbon was used as the multi-scale porous structure that easily disperses nanoparticles and enhances the diffusion of electrolyte. The 3D cross-linked hollow tubular structure of the catalyst resulted in an ammonia yield of 20.03 μg h^{-1} mg_{cat}^{-1} and a FE of 10.76%.[237]

A remarkable study was conducted by Rasyotra *et al.* where titanium diboride (TiB_2) was used as an electrocatalyst for the NRR. The unique electronic structure of boron enhances N_2 adsorption and reduces the binding strength with proton, thus inhibiting the HER. A high ammonia yield rate of 318 μg h^{-1} cm^{-2} (−0.2 V *vs.* RHE) was achieved, with an FE close to 57%. Using DFT, the authors found the presence of electron-deficient and electron-rich sites which function as "frustrated" Lewis pairs. The Ti and B atoms act as a Lewis base and Lewis acid, respectively, where the electron-rich Ti pushes the electron density towards N_2 molecules from where the electron-deficient B pulls it. This synergy weakens the triple bond and activates the N_2 molecule.[245] Zhou *et al.* also studied a transition metal diboride for the NRR. Using DFT calculations, they proposed the use of MoB_2 due to reasons similar to the previous study. Upon experimental validation, an ammonia synthesis rate of 40.94 ± 0.97 μg h^{-1} mg^{-1} (−0.4 V *vs.* RHE) and an FE of 30.84 ± 0.91% (−0.3 V *vs.* RHE) were achieved.[255]

Liu *et al.* presented an interesting article where they emphasized that the morphology of the catalyst has a huge impact on the catalyst performance. They used Cu_3P nanoribbons as catalysts for the NRR and achieved a rate of 18.9 μg h^{-1} mg_{cat}^{-1} with an FE of 37.8% at −0.2 V in an acid electrolyte, which was four times higher than those of Cu_3P nanoparticles. The nanoribbon material had the flexibility of one-dimensional nanoparticles and the high surface area of two-dimensional nanoparticles, which aided in the improvement of ammonia formation.[241]

The nitrate reduction reaction has garnered a lot of attention due to its potential to mitigate the harmful effects of nitrate pollution in water, as discussed earlier. The development of catalysts to convert nitrate ions into the economically valuable ammonia has been a hot topic and may even have attracted more number of studies as compared to the NRR. Mu *et al.* and Li *et al.* studied the use of Pd metallene to support sub-nm RuO_x clusters, so that they can be used as the catalyst for nitrate reduction reaction (NO_3RR). Using this as a working electrode, gave a very high ammonia yield rate of 23.5 mg h^{-1} cm^{-2} and a high faradaic efficiency of 98.6% at −0.5 V *vs.* RHE. This is due

to the low adsorption energy of NO_3^-, achieved by a synergistic effect between RuO_x clusters and Pd metallene. Pd is responsible for dissociation of H_2O to H^+, and RuO_x clusters facilitate the adsorption of NO_3^-. The adsorbed electron flow over the surface of Pd to the interface of RuO_x/Pd and enable the reduction of nitrate.[224,292]

Single-atom catalysts (SAC) have been studied extensively for their use as electrocatalysts for the NO_3 RR over metal-based catalysts due to the lack of active adjacent sites. This ensures that the coupling of N–N is prevented during the reduction of NO_3^-. Wu *et al.* reported that the Fe SAC gave a maximum faradaic efficiency of 75% at −0.66 V *vs.* reversible hydrogen electrode (RHE) and an impressive NH_3 yield rate of ∼20 000 μg h^{-1} mg_{cat}^{-1}.[271] Recent studies have shown that the results obtained with a metal-nonmetal catalytic pair are better than those achieved using SACs. This is due to the sluggish dissociation of water over the surface of transition metals SACs. The Co_1–P/NPG (Co–P catalytic pair with strong electronic interaction with N,P-doped graphitic carbon) exhibits extraordinary NO_3^- reduction with a maximum ammonia yield rate of 8.6 mg_{NH_3} h^{-1} $mg_{catalyst}^{-1}$ and a faradaic efficiency of 93.8% at −0.7 V *vs.* RHE. The Co site acts as an adsorption site for NO_3^- and the P site is responsible for the generation of H^+ by water dissociation.[282] Hai *et al.* studied the bimetallic synergistic effect in the $NiCoO_2$@Cu catalyst, which showed a high faradaic efficiency of 94.2% at −0.7 V *vs.* RHE and an average ammonia yield rate of 5940.73 μg h^{-1} cm^{-2}. The adsorption of NO_3^- occurs through bimetallic sites of Ni and Co, where each site adsorbs one oxygen, whereas in Co_3O_4, the two oxygen atoms are adsorbed on Co. Adsorption with $NiCoO_2$ is more stable than adsorption with Co_3O_4 (E_{ads} of −2.29 eV at Co adsorption site on $NiCoO_2$ and E_{ads} of −0.69 eV at Co adsorption site on Co_3O_4).[274]

Some studies have shown that Fe_2O_3 possesses a good adsorption rate of nitrate ions. The synergetic effect of these two could achieve extraordinary results. This was confirmed by Luo *et al.* through their study of Ru nanoparticles loaded on Fe_2O_3 for ammonia synthesis, which achieved a faradaic efficiency of 72.8% and an ammonia yield rate of 329 μmol cm^{-1} h^{-1}.[275] Luo *et al.* also studied boron-doped MoS_2 catalyst, which gave a NH_3 yield rate of 10.8 mg h^{-1} cm^{-2} at −0.7 V *vs.* RHE, with a faradaic efficiency of 92.3%. The introduction of boron as a dopant increased the binding energy of the 3-d orbital of Mo and 2-p orbital of S by 0.2 eV and 0.15 eV, respectively. As a result, boron extracts electrons from MoS_2 to the doping site and makes the surface electron deficient. This resulted in an increased adsorption of NO_3^- ions. Since boron is electron rich, it can donate electrons to the antibonding orbital of nitrate ions and help in its activation. Moreover, B–MoS_2 also exhibits high adsorption energy of H, which inhibits the occurrence of HERs, thereby resulting in higher efficiency.[276]

While electrochemical ammonia synthesis is an exciting and sustainable approach, overcoming its current limitations requires a multi-faceted strategy involving catalyst innovation, reactor design improvements, and process optimization. Research must focus on the development of advanced catalysts that enhance nitrogen activation, improve faradaic efficiency, and suppress the HER. Transition metal-based materials, single-atom catalysts, and surface-modified electrodes hold promise for addressing these challenges. Additionally, optimizing electrolytes by using non-aqueous systems or ionic liquids can help regulate proton availability and improve selectivity toward ammonia formation. Beyond materials development, reactor engineering is crucial for scaling up the process. Innovations such as flow-cell reactors, membrane-based systems, and high-surface-area electrodes could enhance mass transport and charge transfer, making large-scale operation feasible. Furthermore, integrating external stimuli such as thermal or photo-assisted techniques could accelerate reaction kinetics and improve ammonia production rates. By addressing these challenges, this technology can transition toward higher technology readiness level (TRL) and become a viable alternative for green ammonia production in the future.

7. Conclusion

Ammonia has long been essential as a fertilizer and is now gaining attention for its hydrogen storage and fuel potential. However, industrial ammonia synthesis is highly energy- and carbon-intensive, contributing to 2% of global energy use and 1.44% of CO_2 emissions. Therefore, much of the ongoing research on ammonia is focused on developing catalysts for its sustainable production.

In this review paper, we summarised the three major routes for low-temperature ammonia synthesis (thermochemical, electrochemical and non-thermal plasma-assisted synthesis) with a comprehensive discussion on the catalytic advancements made in each of these methods. The high cost of renewable energy coupled with its intermittency has resulted in a very high cost of ammonia produced from the electrochemical and NTP methods. Moreover, their modularity makes them more suitable for small-scale ammonia production, where it could be produced on demand to meet the regional needs. From the standpoint of large-scale ammonia production, the technology readiness level (TRL) of these methods is very low, and hence, the HB process is still going to sustain the global ammonia demand for the next few decades. Therefore, while this paper presents a detailed understanding of different modes of ammonia production and the corresponding catalytic developments, it is primarily focused on low-temperature catalysts for the production of ammonia following the HB route.

Several classes of catalysts have been studied for their ability to perform at low temperatures, with some materials such as hydrides and electrides yielding a decent ammonia production rate at temperatures as low as 250–300 °C. Optimising the cost of the catalyst has been the main challenge that researchers are trying to overcome. For instance, ruthenium is an excellent catalyst if we look at the rate of ammonia produced. However, due to its very high cost, it is not feasible for industrial applications. While obtaining a good ammonia formation rate is important, it is how we are cutting down the catalyst cost efficiently, which plays a pivotal role in transforming the HB process. Maximising the TOF can be useful in this regard; a higher TOF would mean that the catalyst converts more reactants per active site per unit time, resulting in a lesser amount of catalysts being used to produce

a given amount of ammonia. The ammonia production rate, while seeming to be a good metric to judge the performance of the catalyst, masks two very necessary points that we must consider.

(i) First, it is necessary to understand that these studies are on a laboratory scale, and only the inspection of catalytic activity for large-scale production would give an idea of how readily the material can be adopted for industrial ammonia production.

(ii) Second, it is necessary to analyse the viability of implementing that catalyst for industrial use. While the initial cost of catalyst is important to consider, it is also necessary that the spent catalyst withstands a large number of cycles, so that it does not have to be continually replaced with a fresh catalyst. Often, complex formulations with very precise synthesis techniques are reported, but if this compromises the ease of operation, then it might not be feasible to use that material for large-scale production.

For future research on catalysts, it is recommended to formulate quantitative parameters which can include catalyst cost, lifetime, activity, and consumption in the perspective of ammonia manufacture. Currently, the activities of newer catalysts are compared with the conventional HB catalysts, which does not provide clarity over the several complexities in the catalyst design. This includes varying costs of transition metals, intricacies in the synthesis procedures and the important role of ammonia synthesis loop. Hence, it is vital for future studies on the design and development of catalysts to consider:

(i) Tailoring active sites of the catalysts to address the issues related to nitrogen activation, hydrogen activation, and hydrogenation of adsorbed nitrogen molecules, and desorption of NH_x species.

(ii) Developing facile synthesis procedures for such catalysts with high intrinsic activity and ability to maximize the utility of available active sites.

(iii) Addressing the issue to prolong the lifetime of catalysts, particularly to match the scale and intermittency when coupled with renewable energy sources.

Moreover, the commercial catalyst has only seen a few modifications despite decades of operation, indicating that it is also necessary to investigate other ways to optimize the HB process. Designing an efficient reactor configuration to reduce the heat and compressor duty would synergise the enhancement offered by the catalyst and enable us to synthesize ammonia under optimal conditions at an optimal cost. While the above-mentioned changes can help alleviate the environmental concerns associated with the HB process, it is the decentralised production of green ammonia that could bring the concept of "circular ammonia economy" to reality. Small-scale plants are not much affected by the intermittency of renewable energy sources and are perfect to implement lab-scale studies on green ammonia production on a relatively large scale. Renewable energy could be used to drive the water splitting reaction to produce hydrogen on-site. This could then be used by the small-scale ammonia production plant to produce green ammonia, which can then be used for various purposes based on the location of the plant. Technologies with a low TRL or those that cannot withstand the harsh requirements of the industrial process can be implemented in these small-scale plants. Electrochemical and NTP methods can particularly be used in this scenario, as it is assumed that the ammonia supply chain in the future will be driven by an entirely carbon-free process. We can also obtain insights into the ground-level problems faced in the implementation of these methods. Hence, while the optimized HB process can meet the larger demands, increasing the number of these decentralised ammonia production plants would not only enrich the local supply chain of ammonia, but would also ease the transition to 100% green ammonia production in the future. Ammonia has a vast potential to mitigate carbon emissions due to its ability to act as an alternative to fossil fuels. The proposed decentralised model for ammonia production would not only benefit the billions of people dependent on ammonia but also push us closer to our sustainable development goals.

Data availability

The data presented in this article are gathered from the literature and are cited as per the reference style of the journal.

Conflicts of interest

There are no conflicts to declare.

Acknowledgements

S. K. extends gratitude to Central Power of Research Institute (CPRI) for providing fund grants to conduct the work (CPRI/R&D/TC/GDEC/2024). Authors thank the Indian Institute of Technology Patna (IIT Patna) for providing the required facilities to conduct the literature reviews. P. K. Roy and N. Wagh acknowledge IIT Patna and CPRI for their fellowships, respectively.

References

1 S. Giddey, S. P. S. Badwal, C. Munnings and M. Dolan, *ACS Sustain. Chem. Eng.*, 2017, **5**, 10231–10239.
2 Global ammonia annual production capacity|Statista, **https://www.statista.com/statistics/1065865/ammonia-production-capacity-globally/**, accessed 23 August 2024.
3 A. E. Yüzbaşıoğlu, C. Avşar and A. O. Gezerman, *Curr. Res. Green Sustainable Chem.*, 2022, **5**, 100307.
4 B. Yang, W. Ding, H. Zhang and S. Zhang, *Energy Environ. Sci.*, 2021, **14**, 672–687.
5 Ammonia – American Chemical Society, **https://www.acs.org/molecule-of-the-week/archive/a/ammonia.html**, accessed 23 August 2024.
6 Ammonia as a Refrigerant: Efficient and Eco-Friendly Choice, **https://ammoniagas.com/ammonia-as-a-refrigerant/**,accessed 22 August 2024.
7 Benefits of Ammonia Use in Refrigeration|Danfoss, **https://www.danfoss.com/en-in/markets/refrigeration-and-air-conditioning/dcs/industrial-refrigeration/ammonia-in-industrial-refrigeration/why-ammonia/**, accessed 23 August 2024.

8 Top Reasons to Avoid Ammonia Cleaners, https://www.freshwaveworks.com/blogs/tips-how-to-use/top-reasons-to-avoid-ammonia-cleaners, accessed 23 August 2024.
9 Z. Wan, Y. Tao, J. Shao, Y. Zhang and H. You, *Energy Convers. Manage.*, 2021, **228**, 113729.
10 A. Valera-Medina, F. Amer-Hatem, A. K. Azad, I. C. Dedoussi, M. de Joannon, R. X. Fernandes, P. Glarborg, H. Hashemi, X. He, S. Mashruk, J. McGowan, C. Mounaim-Rouselle, A. Ortiz-Prado, A. Ortiz-Valera, I. Rossetti, B. Shu, M. Yehia, H. Xiao and M. Costa, *Energy Fuels*, 2021, **35**, 6964–7029.
11 Ammonia's Role in a Net-Zero Hydrogen Economy – Kleinman Center for Energy Policy, https://kleinmanenergy.upenn.edu/research/publications/ammonias-role-in-a-net-zero-hydrogen-economy/, accessed 23 August 2024.
12 D. R. MacFarlane, P. V. Cherepanov, J. Choi, B. H. R. Suryanto, R. Y. Hodgetts, J. M. Bakker, F. M. Ferrero Vallana and A. N. Simonov, *Joule*, 2020, **4**, 1186–1205.
13 M. El-Shafie and S. Kambara, *Int. J. Hydrogen Energy*, 2023, **48**, 11237–11273.
14 O. Herbinet, P. Bartocci and A. Grinberg Dana, *Fuel Commun.*, 2022, **11**, 100064.
15 X. Xu, E. Liu, N. Zhu, F. Liu, F. Qian, X. Xu, E. Liu, N. Zhu, F. Liu and F. Qian, *Energies*, 2022, **15**, 1023.
16 J. Li, R. Zhang, J. Pan, H. Wei, G. Shu and L. Chen, *Energy Convers. Manage.*, 2023, **280**, 116827.
17 D. Erdemir and I. Dincer, *Int. J. Energy Res.*, 2021, **45**, 4827–4834.
18 G. Langella, M. de Joannon, P. Sabia, P. Iodice and A. Amoresano, *J. Phys.:Conf. Ser.*, 2022, **2385**, 012036.
19 A. Wojcik, H. Middleton, I. Damopoulos and J. Van Herle, *J. Power Sources*, 2003, **118**, 342–348.
20 G. Cinti, L. Barelli and G. Bidini, *AIP Conf. Proc.*, 2019, **2191**, 020048.
21 S. S. Rathore, S. Biswas, D. Fini, A. P. Kulkarni and S. Giddey, *Int. J. Hydrogen Energy*, 2021, **46**, 35365–35384.
22 M. Otto, L. Vesely, J. Kapat, M. Stoia, N. D. Applegate, G. Natsui, M. Asme, G. E. Aerospace and G. E. Research, *ASME Open J. Eng.*, 2023, **2**, 021033.
23 H. Cao, J. Guo, F. Chang, C. Pistidda, W. Zhou, X. Zhang, A. Santoru, H. Wu, N. Schell, R. Niewa, P. Chen, T. Klassen and M. Dornheim, *Chem. – Eur. J.*, 2017, **23**, 9766–9771.
24 J. Humphreys, R. Lan and S. Tao, *Adv. Energy Sustainability Res.*, 2021, **2**, 2000043.
25 M. Hattori, S. Iijima, T. Nakao, H. Hosono and M. Hara, *Nat. Commun.*, 2020, **111**, 1–8.
26 M. Hattori, N. Okuyama, H. Kurosawa and M. Hara, *J. Am. Chem. Soc.*, 2023, **145**, 7888–7897.
27 H. D. Vandervell and K. C. Waugh, *Chem. Phys. Lett.*, 1990, **171**, 462–468.
28 G. Ertl, S. B. Lee and M. Weiss, *Surf. Sci.*, 1982, **114**, 527–545.
29 C. T. Rettner and H. Stein, *Phys. Rev. Lett.*, 1987, **59**, 2768–2771.
30 T. Oguri, *J. Phys. Soc. Jpn.*, 1964, **19**, 77–83.
31 P. K. Roy and S. Kumar, *J. Environ. Chem. Eng.*, 2023, **11**, 109097.
32 M. Kitano, Y. Inoue, M. Sasase, K. Kishida, Y. Kobayashi, K. Nishiyama, T. Tada, S. Kawamura, T. Yokoyama, M. Hara and H. Hosono, *Angew. Chem., Int. Ed.*, 2018, **57**, 2648–2652.
33 Y. Kobayashi, M. Kitano, S. Kawamura, T. Yokoyama and H. Hosono, *Catal. Sci. Technol.*, 2017, **7**, 47–50.
34 S. Siporin, *J. Catal.*, 2004, **225**, 359–368.
35 A. Borodziński and M. Bonarowska, *Langmuir*, 1997, **13**, 5613–5620.
36 H. Liu and W. Han, *Catal. Today*, 2017, **297**, 276–291.
37 R. Kojima and K. Aika, *Appl. Catal., A*, 2001, **218**, 121–128.
38 Ammonia Production|Encyclopedia MDPI, https://encyclopedia.pub/entry/1129, accessed 23 August 2024.
39 T. Wang and F. Abild-Pedersen, *Proc. Natl. Acad. Sci. U. S. A.*, 2021, **118**, e2106527118.
40 International Energy Agency (IEA), *Ammonia technology roadmap*, 2021, DOI: 10.1787/f6daa4a0-en.
41 K. Smart, *Johnson Matthey Technol. Rev.*, 2022, **66**, 230–244.
42 M. Malmali, Y. Wei, A. McCormick and E. L. Cussler, *Ind. Eng. Chem. Res.*, 2016, **55**, 8922–8932.
43 M. Malmali, G. Le, J. Hendrickson, J. Prince, A. V. McCormick and E. L. Cussler, *ACS Sustain. Chem. Eng.*, 2018, **6**, 6536–6546.
44 M. Malmali, M. Reese, A. V. McCormick and E. L. Cussler, *ACS Sustain. Chem. Eng.*, 2018, **6**, 827–834.
45 F. Tian, J. Li, W. Chen, L. Tang and M. Wu, *Int. J. Hydrogen Energy*, 2024, **78**, 92–122.
46 F. Tian, N. Zhou, W. Chen, J. Zhan, L. Tang and M. Wu, *Adv. Sustainable Syst.*, 2024, **8**, 2300618.
47 V. Shahed Gharahshiran and Y. Zheng, *J. Energy Chem.*, 2024, **96**, 1–38.
48 J. Mu, X. Gao, T. Yu, L. Zhao, W. Luo, H. Yang, Z. Liu, Z. Sun, Q. Gu and F. Li, *Adv. Sci.*, 2024, **11**, 2308979.
49 X. Long, F. Huang, Z. Yao, P. Li, T. Zhong, H. Zhao, S. Tian, D. Shu and C. He, *Small*, 2024, **20**, 2400551.
50 H. Wan, A. Bagger and J. Rossmeisl, *Angew. Chem., Int. Ed.*, 2021, **60**, 21966–21972.
51 N. Segal, *J. Catal.*, 1967, **8**, 113–119.
52 D. King, *J. Catal.*, 1965, **4**, 253–259.
53 M. R. Hillis, C. Kemball and M. W. Roberts, *Trans. Faraday Soc.*, 1966, **62**, 3570.
54 R. Kojima and K. Aika, *Appl. Catal., A*, 2001, **209**, 317–325.
55 D. Mckay, J. S. J. S. J. Hargreaves, J. L. L. Rico, J. L. L. Rivera and X.-L. L. Sun, *J. Solid State Chem.*, 2008, **181**, 325–333.
56 R. Kojima and K. Aika, *Appl. Catal., A*, 2001, **215**, 149–160.
57 N. Bion, F. Can, J. Cook, J. S. J. S. J. Hargreaves, A. L. L. Hector, W. Levason, A. R. R. McFarlane, M. Richard and K. Sardar, *Appl. Catal., A*, 2015, **504**, 44–50.
58 C. J. H. H. Jacobsen, *Chem. Commun.*, 2000, 1057–1058.
59 C. J. H. H. Jacobsen, S. Dahl, B. S. G. S. Clausen, S. Bahn, A. Logadottir and J. K. Nørskov, *J. Am. Chem. Soc.*, 2001, **123**, 8404–8405.
60 A. Logadottir, T. Rod, J. Nørskov, B. Hammer, S. Dahl and C. J. Jacobsen, *J. Catal.*, 2001, **197**, 229–231.

61 Y. Cao, E. Toshcheva, W. Almaksoud, R. Ahmad, T. Tsumori, R. Rai, Y. Tang, L. Cavallo, H. Kageyama and Y. Kobayashi, *ChemSusChem*, 2023, **16**, e202300234.
62 C. Zhang, S. Shi, B. Fang, J. Ni, J. Lin, X. Wang, B. Lin and L. Jiang, *Chin. Chem. Lett.*, 2023, **34**, 107237.
63 M. Miyazaki, K. Ikejima, K. Ogasawara, M. Kitano and H. Hosono, *ChemSusChem*, 2023, **16**, e202300551.
64 S. Al Sobhi, J. S. J. Hargreaves, A. L. Hector and S. Laassiri, *Dalton Trans.*, 2019, **48**, 16786–16792.
65 Y. Zhou, X. Peng, T. Zhang, H. Cai, B. Lin, L. Zheng, X. Wang and L. Jiang, *ACS Catal.*, 2022, **12**, 7633–7642.
66 S. Al Sobhi, N. Bion, J. S. J. Hargreaves, A. L. Hector, S. Laassiri, W. Levason, A. W. Lodge, A. R. McFarlane and C. Ritter, *Mater. Res. Bull.*, 2019, **118**, 110519.
67 X. Peng, H. X. Liu, Y. Zhang, Z. Q. Huang, L. Yang, Y. Jiang, X. Wang, L. Zheng, C. Chang, C. T. Au, L. Jiang and J. Li, *Chem. Sci.*, 2021, **12**, 7125–7137.
68 Y. Zhou, C. Wang, X. Peng, T. Zhang, X. Wang, Y. Jiang, H. Qi, L. Zheng, J. Lin and L. Jiang, *CCS Chem.*, 2022, **4**, 1758–1769.
69 R. Kojima and K. I. Aika, *Appl. Catal., A*, 2001, **215**, 149–160.
70 T.-N. N. Ye, S.-W. W. Park, Y. Lu, J. Li, M. Sasase, M. Kitano, T. Tada and H. Hosono, *Nature*, 2020, **583**, 391–395.
71 T.-N. N. Ye, S.-W. W. Park, Y. Lu, J. Li, M. Sasase, M. Kitano and H. Hosono, *J. Am. Chem. Soc.*, 2020, **142**, 14374–14383.
72 Y. Zhou, C.-Q. Q. Xu, Z. Tan, H. Cai, X. Wang, J. J. Li, L. Zheng, C. T. Au, J. J. Li and L. Jiang, *ACS Catal.*, 2022, **12**, 2651–2660.
73 J. Humphreys, R. Lan, S. Chen, M. Walker, Y. Han and S. Tao, *Appl. Catal., B*, 2021, **285**, 119843.
74 Z. Chen, Y. Ye, T. Peng, C. Wu, H. Li, X. Pan and X. Bao, *ACS Catal.*, 2023, **13**, 14385–14394.
75 S. Ghosh, S. M. Jeong and S. R. Polaki, *Korean J. Chem. Eng.*, 2018, **35**, 1389–1408.
76 Y. Zhang, J. Zhao, D. Yang, B. Wang, Y. Zhou, J. Wang, H. Chen, T. Mei, S. Ye and J. Qu, *Nat. Chem.*, 2022, **14**, 46–52.
77 R. Morimoto, T. Ogawa, K. Torii, T. Seno, H. Okumura and K. N. Ishihara, *ChemRxiv*, 2023, DOI: **10.26434/chemrxiv-2023-ng4n7-v2**.
78 Y. Cao, A. Saito, Y. Kobayashi, H. Ubukata, Y. Tang and H. Kageyama, *ChemCatChem*, 2021, **13**, 191–195.
79 Q. Wang, H. Wen, Y. Guan, S. Zhang, W. Gao, J. Guo and P. Chen, *ACS Catal.*, 2023, **13**, 9882–9890.
80 H. Yan, W. Gao, Q. Wang, J. Guo and P. Chen, *Faraday Discuss.*, 2023, **243**, 55–64.
81 C. Liu, Q. Wang, J. Guo, T. Vegge, P. Chen and H. A. Hansen, *ACS Catal.*, 2022, **12**, 4194–4202.
82 W. Gao, Q. Wang, Y. Guan, H. Yan, J. Guo and P. Chen, *Faraday Discuss.*, 2023, **243**, 27–37.
83 Y. Goto, M. Kikugawa, K. Kobayashi, Y. Manaka, T. Nanba, H. Matsumoto, M. Matsumoto, M. Aoki and H. Imagawa, *RSC Adv.*, 2023, **13**, 15410–15415.
84 M. Hara, M. Hattori and H. Kurosawa, *Iron to catalyze ammonia synthesis at low temperature*, 2022, DOI: **10.21203/RS.3.RS-1426351/V2**.
85 P. Wang, F. Chang, W. Gao, J. Guo, G. Wu, T. He and P. Chen, *Nat. Chem.*, 2017, **9**, 64–70.
86 H. Yan, W. Gao, Q. Wang, J. Guo and P. Chen, *Faraday Discuss.*, 2023, **243**, 55–64.
87 Y. Inoue, M. Kitano, K. Kishida, H. Abe, Y. Niwa, M. Sasase, Y. Fujita, H. Ishikawa, T. Yokoyama, M. Hara and H. Hosono, *ACS Catal.*, 2016, **6**, 7577–7584.
88 P. K. Roy and S. Kumar, *Int. J. Hydrogen Energy*, 2024, **64**, 497–506.
89 Q. Wang, J. Pan, J. Guo, H. A. Hansen, H. Xie, L. Jiang, L. Hua, H. Li, Y. Guan, P. Wang, W. Gao, L. Liu, H. Cao, Z. Xiong, T. Vegge and P. Chen, *Nat. Catal.*, 2021, **411**(4), 959–967.
90 P. K. Roy and S. Kumar, *ACS Appl. Energy Mater.*, 2020, **3**, 7167–7179.
91 M. Kitano, S. Kanbara, Y. Inoue, N. Kuganathan, P. V. Sushko, T. Yokoyama, M. Hara and H. Hosono, *Nat. Commun.*, 2015, **61**(6), 1–9.
92 S. Kanbara, M. Kitano, Y. Inoue, T. Yokoyama, M. Hara and H. Hosono, *J. Am. Chem. Soc.*, 2015, **137**, 14517–14524.
93 Y. Gong, J. Wu, M. Kitano, J. Wang, T. N. Ye, J. Li, Y. Kobayashi, K. Kishida, H. Abe, Y. Niwa, H. Yang, T. Tada and H. Hosono, *Nat. Catal.*, 2018, **13**(1), 178–185.
94 Y. Lu, J. Li, T. Tada, Y. Toda, S. Ueda, T. Yokoyama, M. Kitano and H. Hosono, *J. Am. Chem. Soc.*, 2016, **138**, 3970–3973.
95 T. N. Ye, Y. Lu, J. Li, T. Nakao, H. Yang, T. Tada, M. Kitano and H. Hosono, *J. Am. Chem. Soc.*, 2017, **139**, 17089–17097.
96 C. Li, Z. Zhang, Y. Zheng, B. Fang, J. Ni, J. Lin, B. Lin, X. Wang and L. Jiang, *Chem. Eng. Sci.*, 2022, **251**, 117434.
97 T.-N. N. Ye, Y. Lu, Y. Kobayashi, J. Li, S.-W. W. Park, M. Sasase, M. Kitano and H. Hosono, *J. Phys. Chem. C*, 2020, **124**, 28589–28595.
98 Y. Gong, H. Li, J. Wu, X. Song, X. Yang, X. Bao, X. Han, M. Kitano, J. Wang and H. Hosono, *J. Am. Chem. Soc.*, 2022, **144**, 8683–8692.
99 C. Croisé, K. Alabd, S. Tencé, E. Gaudin, A. Villesuzanne, X. Courtois, N. Bion and F. Can, *ChemCatChem*, 2023, **15**, e202201172.
100 G. Liang, J. Huot and R. Schulz, *J. Alloys Compd.*, 2001, **320**, 133–139.
101 H. J. Ahn and J. Y. Lee, *Int. J. Hydrogen Energy*, 1991, **16**, 93–99.
102 R. L. Cohen and K. W. West, *J. Less-Common Met.*, 1983, **95**, 17–23.
103 Y. Nakamura, K. Sato, S. Fujitani, K. Nishio, K. Oguro and I. Uehara, *J. Alloys Compd.*, 1998, **267**, 205–210.
104 H. Li, Y. Gong, H. Yang, X. Yang, K. Li, J. Wang and H. Hosono, *ChemSusChem*, 2023, **16**, e202301016.
105 C. Croisé, K. Alabd, A. Villesuzanne, F. Can, X. Courtois, E. Gaudin, S. Tencé and N. Bion, *Catal. Commun.*, 2023, **179**, 106689.
106 H. Hosono and M. Kitano, *Chem. Rev.*, 2021, **121**, 3121–3185.
107 J. L. Dye, *Acc. Chem. Res.*, 2009, **42**, 1564–1572.
108 Y. Jiang, R. Takashima, T. Nakao, M. Miyazaki, Y. Lu, M. Sasase, Y. Niwa, H. Abe, M. Kitano and H. Hosono, *J. Am. Chem. Soc.*, 2023, **145**, 10669–10680.
109 Y. Gong, H. Li, C. Li, X. Yang, J. Wang and H. Hosono, *Chem. Mater.*, 2022, **34**, 1677–1685.

110 J. Kammert, J. Moon, Y. Cheng, L. Daemen, S. Irle, V. Fung, J. Liu, K. Page, X. Ma, V. Phaneuf, J. Tong, A. J. Ramirez-Cuesta and Z. Wu, *J. Am. Chem. Soc.*, 2020, **142**, 7655–7667.
111 M. Kitano, Y. Inoue, Y. Yamazaki, F. Hayashi, S. Kanbara, S. Matsuishi, T. Yokoyama, S. W. Kim, M. Hara and H. Hosono, *Nat. Chem.*, 2012, **411**(4), 934–940.
112 Z. Kowalczyk, S. Jodzis, W. Raróg, J. Zieliński, J. Pielaszek and A. Presz, *Appl. Catal., A*, 1999, **184**, 95–102.
113 W. Raróg-Pilecka, E. Miśkiewicz, S. Jodzis, J. Petryk, D. Łomot, Z. Kaszkur, Z. Karpiński and Z. Kowalczyk, *J. Catal.*, 2006, **239**, 313–325.
114 Y. Kadowaki and K. I. Aika, *J. Catal.*, 1996, **161**, 178–185.
115 X. Zhang, L. Liu, J. Wang, X. Ju, R. Si, J. Feng, J. Guo and P. Chen, *J. Catal.*, 2023, **417**, 382–395.
116 H. Ronduda, M. Zybert, A. Dziewulska, W. Patkowski, K. Sobczak, A. Ostrowski and W. Raróg-Pilecka, *Surf. Interfaces*, 2023, **36**, 102530.
117 J. Feng, L. Liu, X. Ju, Q. Jiang, J. Wang, J. Guo, T. He and P. Chen, *Catal. Sci. Technol.*, 2023, **13**, 4156–4167.
118 W. J. Movick, F. Kishimoto and K. Takanabe, *Chem. Eng. J.*, 2023, **452**, 139525.
119 C. Li, M. Li, Y. Zheng, B. Fang, J. Lin, J. Ni, B. Lin and L. Jiang, *Appl. Catal., B*, 2023, **320**, 121982.
120 Y. Baik, M. Kwen, K. Lee, S. Chi, S. Lee, K. Cho, H. Kim and M. Choi, *J. Am. Chem. Soc.*, 2023, **145**, 11364–11374.
121 W. Patkowski, M. Zybert, H. Ronduda, G. Gawrońska, A. Albrecht, D. Moszyński, A. Fidler, P. Dłużewski and W. Raróg-Pilecka, *Catal*, 2023, **13**, 405.
122 R. Javaid and T. Nanba, *Int. J. Hydrogen Energy*, 2023, **48**, 11214–11224.
123 R. Javaid and T. Nanba, *Top. Catal.*, 2023, **66**, 452–460.
124 J. Feng, L. Liu, X. Zhang, J. Wang, X. Ju, R. Li, J. Guo, T. He and P. Chen, *Catal. Sci. Technol.*, 2023, **13**, 844–853.
125 H. M. Vieri, A. Badakhsh and S. H. Choi, *Int. J. Energy Res.*, 2023, **2023**, 2072245.
126 X. Zhang, L. Liu, A. Wu, J. Zhu, R. Si, J. Guo, R. Chen, Q. Jiang, X. Ju, J. Feng, Z. Xiong, T. He and P. Chen, *ACS Catal.*, 2022, **12**, 2178–2190.
127 M. Osozawa, A. Hori, K. Fukai, T. Honma, K. Oshima and S. Satokawa, *Int. J. Hydrogen Energy*, 2022, **47**, 2433–2441.
128 B. Fang, C. Zhang, Z. Qi, C. Li, J. Ni, X. Wang, J. Lin, C. T. Au, B. Lin and L. Jiang, *AIChE J.*, 2022, **68**, e17849.
129 S. I. Miyahara, K. Sato, K. Tsujimaru, Y. Wada, Y. Ogura, T. Toriyama, T. Yamamoto, S. Matsumura, K. Inazu and K. Nagaoka, *ACS Omega*, 2022, **7**, 24452–24460.
130 S. E. Sivan, K. H. Kang, S. J. Han, O. Francis Ngome Okello, S. Y. Choi, V. Sudheeshkumar, R. W. J. Scott, H. J. Chae, S. Park and U. H. Lee, *J. Catal.*, 2022, **408**, 316–328.
131 J. Wang, L. Liu, X. Zhang, J. Yu, X. Ju, J. Feng, J. Guo, T. He and P. Chen, *Catal. Sci. Technol.*, 2022, **12**, 7501–7509.
132 S. ichiro Miyahara, K. Sato, Y. Kawano, K. Imamura, Y. Ogura, K. Tsujimaru and K. Nagaoka, *Catal. Today*, 2021, **376**, 36–40.
133 H. Ronduda, M. Zybert, W. Patkowski, K. Sobczak, D. Moszyński, A. Albrecht, A. Sarnecki and W. Raróg-Pilecka, *RSC Adv.*, 2022, **12**, 33876–33888.
134 C. Li, S. Yu, Y. Shi, M. Li, B. Fang, J. Lin, J. Ni, X. Wang, B. Lin and L. Jiang, *Chem. Eng. Sci.*, 2022, **262**, 118045.
135 B. Lin, B. Fang, Y. Wu, C. Li, J. Ni, X. Wang, J. Lin, C. T. Au and L. Jiang, *ACS Catal.*, 2021, **11**, 1331–1339.
136 J. Huang, J. Pan, Z. You and X. Jiang, *Int. J. Hydrogen Energy*, 2022, **47**, 28019–28024.
137 R. Woo, K. Lee, B. S. An, S. H. Kim, H. K. Ju, J. H. Kim, J. Shim, H. T. Beum, K. Cho, Y. S. Bae and H. C. Yoon, *Chem. Eng. J.*, 2023, **475**, 146354.
138 Y. Zhao, J. Huang, M. Yuan, X. Li, Y. Wang, M. Li, J. Li and Z. You, *Catal. Lett.*, 2024, **154**, 1715–1729.
139 Y. Zhou, J. Wang, L. Liang, Q. Sai, J. Ni, C. tong Au, X. Lin, X. Wang, Y. Zheng, L. Zheng and L. Jiang, *J. Catal.*, 2021, **404**, 501–511.
140 H. Kim, A. Jan, D. H. Kwon, H. Il Ji, K. J. Yoon, J. H. Lee, Y. Jun, J. W. Son and S. Yang, *Small*, 2023, **19**, 2205424.
141 K. Sato and K. Nagaoka, *Chem. Lett.*, 2021, **50**, 687–696.
142 W. Rarogpilecka, E. Miskiewicz, L. Kepinski, Z. Kaszkur, K. Kielar and Z. Kowalczyk, *J. Catal.*, 2007, **249**, 24–33.
143 M. Karolewska, E. Truszkiewicz, M. Wściseł, B. Mierzwa, L. Kępiński and W. Raróg-Pilecka, *J. Catal.*, 2013, **303**, 130–134.
144 B. Lin, Y. Qi, K. Wei and J. Lin, *RSC Adv.*, 2014, **4**, 38093.
145 K. Sato, K. Nagaoka, S. I. Miyahara, K. Tsujimaru, Y. Wada, T. Toriyama, T. Yamamoto, S. Matsumura, K. Inazu, H. Mohri, T. Iwasa and T. Taketsugu, *ACS Catal.*, 2021, **11**, 13050–13061.
146 H. Ronduda, M. Zybert, W. Patkowski, A. Ostrowski, P. Jodłowski, D. Szymański and W. Raróg-Pilecka, *Int. J. Hydrogen Energy*, 2022, **47**, 35689–35700.
147 H. Ronduda, M. Zybert, W. Patkowski, A. Ostrowski, P. Jodłowski, D. Szymański, L. Kępiński and W. Raróg-Pilecka, *RSC Adv.*, 2021, **11**, 14218–14228.
148 H. Ronduda, M. Zybert, W. Patkowski, A. Ostrowski, P. Jodłowski, D. Szymański, L. Kępiński and W. Raróg-Pilecka, *Int. J. Hydrogen Energy*, 2022, **47**, 6666–6678.
149 E. Apen and J. L. Gland, *Surf. Sci.*, 1994, **321**, 308–317.
150 M. K. Agusta and H. Kasai, *Surf. Sci.*, 2012, **606**, 766–771.
151 X. Lu, S. Francis, D. Motta, N. Dimitratos and A. Roldan, *Phys. Chem. Chem. Phys.*, 2020, **22**, 3883–3896.
152 M. Chen, M. Yuan, J. Li and Z. You, *Appl. Catal., A*, 2018, **554**, 1–9.
153 J. Huang, M. Yuan, X. Li, Y. Wang, M. Li, J. Li and Z. You, *J. Catal.*, 2020, **389**, 556–565.
154 J. Huang, M. Yuan, X. Li, Y. Wang, M. Li, J. Li and Z. You, *Appl. Catal., A*, 2021, **615**, 118058.
155 K. ichi Aika, T. Takano and S. Murata, *J. Catal.*, 1992, **136**, 126–140.
156 D. Szmigiel, W. Raróg-Pilecka, E. Miśkiewicz, M. Gliński, M. Kielak, Z. Kaszkur and Z. Kowalczyk, *Appl. Catal., A*, 2004, **273**, 105–112.
157 D. Szmigiel, H. Bielawa, M. Kurtz, O. Hinrichsen, M. Muhler, W. Raróg, S. Jodzis, Z. Kowalczyk, L. Znak and J. Zieliński, *J. Catal.*, 2002, **205**, 205–212.
158 S. E. Siporin and R. J. Davis, *J. Catal.*, 2004, **222**, 315–322.
159 Y. Baik, M. Kwen, K. Lee, S. Chi, S. Lee, K. Cho, H. Kim and M. Choi, *J. Am. Chem. Soc.*, 2023, **145**, 11364–11374.

160 K. Lee, R. Woo, H. C. Woo, G. Ko, K. Cho, Y. Park, M. Choi and H. C. Yoon, *J. Catal.*, 2024, **434**, 115530.
161 S. Murata and K. I. Aika, *J. Catal.*, 1992, **136**, 110–117.
162 C. Fernández, N. Bion, E. M. Gaigneaux, D. Duprez and P. Ruiz, *J. Catal.*, 2016, **344**, 16–28.
163 B. Lin, L. Heng, B. Fang, H. Yin, J. Ni, X. Wang, J. Lin and L. Jiang, *ACS Catal.*, 2019, **9**, 1635–1644.
164 S. Wu, Y.-K. Peng, T.-Y. Chen, J. Mo, A. Large, I. McPherson, H.-L. Chou, I. Wilkinson, F. Venturini, D. Grinter, P. Ferrer Escorihuela, G. Held and S. C. E. Tsang, *ACS Catal.*, 2020, **10**, 5614–5622.
165 The Ammonia-Synthesis Catalyst of the Next Generation: Barium-Promoted Oxide-Supported Ruthenium – Bielawa – 2001 – Angewandte Chemie International Edition – Wiley Online Library, **https://onlinelibrary.wiley.com/doi/abs/10.1002/1521-3773(20010316)40:6%3C1061::AID-ANIE10610%3E3.0.CO;2-B**, accessed 24 August 2024.
166 C. J. H. Jacobsen, S. Dahl, P. L. Hansen, E. Törnqvist, L. Jensen, H. Topsøe, D. V. Prip, P. B. Møenshaug and I. Chorkendorff, *J. Mol. Catal. A:Chem.*, 2000, **163**, 19–26.
167 K. Sato, K. Imamura, Y. Kawano, S. ichiro Miyahara, T. Yamamoto, S. Matsumura and K. Nagaoka, *Chem. Sci.*, 2016, **8**, 674–679.
168 Y. Niwa and K. I. Aika, *J. Catal.*, 1996, **162**, 138–142.
169 Y. Ogura, K. Sato, S. I. Miyahara, Y. Kawano, T. Toriyama, T. Yamamoto, S. Matsumura, S. Hosokawa and K. Nagaoka, *Chem. Sci.*, 2018, **9**, 2230–2237.
170 Y. Ogura, K. Tsujimaru, K. Sato, S. Miyahara, T. Toriyama, T. Yamamoto, S. Matsumura and K. Nagaoka, *ACS Sustain. Chem. Eng.*, 2018, **6**, 17258–17266.
171 Z. Wang, Z. Cai and Z. Wei, *ACS Sustain. Chem. Eng.*, 2019, **7**, 8226–8235.
172 Z. You, K. Inazu, K. ichi Aika and T. Baba, *J. Catal.*, 2007, **251**, 321–331.
173 Y. Wu, C. Li, B. Fang, X. Wang, J. Ni, B. Lin, J. Lin and L. Jiang, *Chem. Commun.*, 2020, **56**, 1141–1144.
174 K. Sato, S. Miyahara, Y. Ogura, K. Tsujimaru, Y. Wada, T. Toriyama, T. Yamamoto, S. Matsumura and K. Nagaoka, *ACS Sustain. Chem. Eng.*, 2020, **8**, 2726–2734.
175 K. Sato, S. Miyahara, K. Tsujimaru, Y. Wada, T. Toriyama, T. Yamamoto, S. Matsumura, K. Inazu, H. Mohri, T. Iwasa, T. Taketsugu and K. Nagaoka, *ACS Catal.*, 2021, **11**, 13050–13061.
176 J. P. Lange, *Angew. Chem., Int. Ed.*, 2015, **54**, 13186–13197.
177 J. P. Lange, *Catal. Sci. Technol.*, 2016, **6**, 4759–4767.
178 J. Zhang, X. Li, J. Zheng, M. Du, X. Wu, J. Song, C. Cheng, T. Li and W. Yang, *Energy Convers. Manage.*, 2023, **293**, 117482.
179 M. L. Carreon, *J. Phys. D Appl. Phys.*, 2019, **52**, 483001.
180 P. Shrestha, D. P. Subedi and U. M. Joshi, *Electrical characterization of atmospheric pressure dielectric barrier discharge in air*, IAEA-TECDOC-CD-1713, International Atomic Energy Agency, Division of Physical and Chemical Sciences, Vienna, Austria, 2013.
181 U. N. Pal, M. Kumar, H. Khatun and A. K. Sharma, *J. Phys.:Conf. Ser.*, 2008, **114**, 012065.
182 K. Ollegott, P. Wirth, C. Oberste-Beulmann, P. Awakowicz and M. Muhler, *Chem. Ing. Tech.*, 2020, **92**, 1542–1558.
183 Dielectric barrier discharge (DBD)|Institute of Interfacial Process Engineering and Plasma Technology|University of Stuttgart, **https://www.igvp.uni-stuttgart.de/en/research/plasma-technology/sources/barrier/**, accessed 25 August 2024.
184 J. R. Roberts, *Vac. Ultrav. Spectrosc.*, 2000, 37–63.
185 E. N. Eremin, A. N. Maltsev and V. L. Syaduk, *Russ. J. Phys. Chem.*, 1971, **45**(5), 635.
186 L. R. Winter, B. Ashford, J. Hong, A. B. Murphy and J. G. Chen, *ACS Catal.*, 2020, **10**, 14763–14774.
187 Y. Wang, W. Yang, S. Xu, S. Zhao, G. Chen, A. Weidenkaff, C. Hardacre, X. Fan, J. Huang and X. Tu, *J. Am. Chem. Soc.*, 2022, **144**, 12020–12031.
188 Q. Xie, S. Zhuge, X. Song, M. Lu, F. Yu, R. Ruan and Y. Nie, *J. Phys. D Appl. Phys.*, 2019, **53**, 064002.
189 F. Gorky, S. R. Guthrie, C. S. Smoljan, J. M. Crawford, M. A. Carreon and M. L. Carreon, *J. Phys. D Appl. Phys.*, 2021, **54**, 264003.
190 T. Mizushima, K. Matsumoto, H. Ohkita and N. Kakuta, *Plasma Chem. Plasma Process.*, 2007, **27**, 1–11.
191 K. Li, S. Chen, H. Wang and F. Wang, *Appl. Catal., A*, 2023, **650**, 118983.
192 S. Li, Y. Shao, H. Chen and X. Fan, *Ind. Eng. Chem. Res.*, 2022, **61**, 3292–3302.
193 Y. Wang, M. Craven, X. Yu, J. Ding, P. Bryant, J. Huang and X. Tu, *ACS Catal.*, 2019, **9**, 10780–10793.
194 X. Zhu, X. Hu, X. Wu, Y. Cai, H. Zhang and X. Tu, *J. Phys. D Appl. Phys.*, 2020, **53**, 164002.
195 M. Iwamoto, M. Horikoshi, R. Hashimoto, K. Shimano, T. Sawaguchi, H. Teduka and M. Matsukata, *Catal*, 2020, **10**, 590.
196 Y. Zhang, J. Niu, S. Chen, J. Sun, Q. Chen, X. Zhao, B. S. Patil, A. S. R. van Kaathoven, F. J. J. Peeters, N. Cherkasov, J. Lang, Q. Wang and V. Hessel, *J. Phys. D Appl. Phys.*, 2020, **53**, 144003.
197 J. R. Shah, F. Gorky, J. Lucero, M. A. Carreon and M. L. Carreon, *Ind. Eng. Chem. Res.*, 2020, **59**, 5167–5176.
198 A. Gómez-Ramírez, J. Cotrino, R. M. Lambert and A. R. González-Elipe, *Plasma Sources Sci. Technol.*, 2015, **24**, 065011.
199 A. Gómez-Ramírez, A. M. Montoro-Damas, J. Cotrino, R. M. Lambert and A. R. González-Elipe, *Plasma Processes Polym.*, 2017, **14**, 1600081.
200 K. Aihara, M. Akiyama, T. Deguchi, M. Tanaka, R. Hagiwara and M. Iwamoto, *Chem. Commun.*, 2016, **52**, 13560–13563.
201 M. Iwamoto, M. Akiyama, K. Aihara and T. Deguchi, *ACS Catal.*, 2017, **7**, 6924–6929.
202 C. Ndayirinde, Y. Gorbanev, R. G. Ciocarlan, R. De Meyer, A. Smets, E. Vlasov, S. Bals, P. Cool and A. Bogaerts, *Catal. Today*, 2023, **419**, 114156.
203 B. S. Patil, N. Cherkasov, N. V. Srinath, J. Lang, A. O. Ibhadon, Q. Wang and V. Hessel, *Catal. Today*, 2021, **362**, 2–10.
204 T. Mizushima, K. Matsumoto, J. I. Sugoh, H. Ohkita and N. Kakuta, *Appl. Catal., A*, 2004, **265**, 53–59.

205 X. Hu, X. Zhu, X. Wu, Y. Cai and X. Tu, *Plasma Processes Polym.*, 2020, **17**, 2000072.
206 P. Peng, Y. Li, Y. Cheng, S. Deng, P. Chen and R. Ruan, *Plasma Chem. Plasma Process.*, 2016, **36**, 1201–1210.
207 H. H. Kim, Y. Teramoto, A. Ogata, H. Takagi and T. Nanba, *Plasma Processes Polym.*, 2017, **14**, 1600157.
208 P. Peng, Y. Cheng, R. Hatzenbeller, M. Addy, N. Zhou, C. Schiappacasse, D. Chen, Y. Zhang, E. Anderson, Y. Liu, P. Chen and R. Ruan, *Int. J. Hydrogen Energy*, 2017, **42**, 19056–19066.
209 Y. Wang, M. Craven, X. Yu, J. Ding, P. Bryant, J. Huang and X. Tu, *ACS Catal.*, 2019, **9**, 10780–10793.
210 P. Mehta, P. Barboun, F. A. Herrera, J. Kim, P. Rumbach, D. B. Go, J. C. Hicks and W. F. Schneider, *Nat. Catal.*, 2018, **14**(1), 269–275.
211 Y. Liu, C.-W. Wang, X.-F. Xu, B.-W. Liu, G.-M. Zhang, Z.-W. Liu, Q. Chen and H.-B. Zhang, *Plasma Chem. Plasma Process.*, 2022, **42**, 267–282.
212 F. Gorky, A. Best, J. Jasinski, B. J. Allen, A. C. Alba-Rubio and M. L. Carreon, *J. Catal.*, 2021, **393**, 369–380.
213 A. Bajpai and S. Kumar, *Mol. Catal.*, 2024, **557**, 113961.
214 H. Shen, C. Choi, J. Masa, X. Li, J. Qiu, Y. Jung and Z. Sun, *Chem*, 2021, **7**, 1708–1754.
215 Who really discovered the Haber process?|Feature|RSC Education, **https://edu.rsc.org/feature/who-really-discovered-the-haber-process/2020277.article**, accessed 25 August 2024.
216 A. U. Shetty and R. Sankannavar, *J. Energy Chem.*, 2024, **92**, 681–697.
217 P. A. Kempler and A. C. Nielander, *Nat. Commun.*, 2023, **141**, 1–4.
218 W. Guo, K. Zhang, Z. Liang, R. Zou and Q. Xu, *Chem. Soc. Rev.*, 2019, **48**, 5658–5716.
219 M. Zhang, X. Ai, X. Liang, H. Chen and X. Zou, *Adv. Funct. Mater.*, 2023, **33**, 2306358.
220 X. Yang, F. Ling, J. Su, X. Zi, H. Zhang, H. Zhang, J. Li, M. Zhou and Y. Wang, *Appl. Catal., B*, 2020, **264**, 118477.
221 Q. Li, L. He, C. Sun and X. Zhang, *J. Phys. Chem. C*, 2017, **122**(121), 27563–27568.
222 D. Krishnamurthy, N. Lazouski, M. L. Gala, K. Manthiram and V. Viswanathan, *ACS Cent. Sci.*, 2021, **7**, 2073–2082.
223 M. M. M. Kuypers, H. K. Marchant and B. Kartal, *Nat. Rev. Microbiol.*, 2018, **165**(16), 263–276.
224 J. Mu, X. W. Gao, T. Yu, L. K. Zhao, W. Bin Luo, H. Yang, Z. M. Liu, Z. Sun, Q. F. Gu and F. Li, *Adv. Sci.*, 2024, **11**, 2308979.
225 X. Zhang, Y. Wang, C. Liu, Y. Yu, S. Lu and B. Zhang, *Chem. Eng. J.*, 2021, **403**, 126269.
226 S. Niu, *J. Energy Chem.*, 2023, **86**, 69–83.
227 J. Long, S. Chen, Y. Zhang, C. Guo, X. Fu, D. Deng and J. Xiao, *Angew. Chem., Int. Ed.*, 2020, **59**, 9711–9718.
228 H. Niu, Z. Zhang, X. Wang, X. Wan, C. Kuai, Y. Guo, H. Niu, X. Wang, X. Wan, C. Kuai, Y. Guo and Z. Zhang, *Small*, 2021, **17**, 2102396.
229 L. Chen, D. Shen, B. Li, Z. Xiao, W. Sun, X. Liu, J. Ma, C. Li and W. Wang, *Ceram. Int.*, 2023, **49**, 23129–23139.
230 Q. Wu, H. Wang, S. Shen, B. Huang, Y. Dai and Y. Ma, *J. Mater. Chem. A*, 2021, **9**, 5434–5441.
231 Y. Li, C. Cheng, S. Han, Y. Huang, X. Du, B. Zhang and Y. Yu, *ACS Energy Lett.*, 2022, **7**, 1187–1194.
232 C. He, H. Yang, M. Xi, L. Fu, J. Huo and C. Zhao, *Environ. Res.*, 2022, **212**, 113479.
233 J. Wu and Y. X. Yu, *Int. J. Hydrogen Energy*, 2023, **48**, 5961–5975.
234 X. Qian, Y. Wei, M. Sun, Y. Han, X. Zhang, J. Tian and M. Shao, *Chin. J. Catal.*, 2022, **43**, 1937–1944.
235 Y. Cui, A. Dong, Y. Qu, J. Zhang, M. Zhao, Z. Wang and Q. Jiang, *Chem. Eng. J.*, 2021, **426**, 131843.
236 H. Chen, T. Wu, X. Li, S. Lu, F. Zhang, Y. Wang, H. Zhao, Q. Liu, Y. Luo, A. M. Asiri, Z. Feng, Y. Zhang and X. Sun, *ACS Sustain. Chem. Eng.*, 2021, **9**, 1512–1517.
237 H. Chen, J. Liang, K. Dong, L. Yue, T. Li, Y. Luo, Z. Feng, N. Li, M. S. Hamdy, A. A. Alshehri, Y. Wang, X. Sun and Q. Liu, *Inorg. Chem. Front.*, 2022, **9**, 1514–1519.
238 G. Lin, Q. Ju, X. Guo, W. Zhao, S. Adimi, J. Ye, Q. Bi, J. Wang, M. Yang and F. Huang, *Adv. Mater.*, 2021, **33**, 2007509.
239 Z. Du, J. Liang, S. Li, Z. Xu, T. Li, Q. Liu, Y. Luo, F. Zhang, Y. Liu, Q. Kong, X. Shi, B. Tang, A. M. Asiri, B. Li and X. Sun, *J. Mater. Chem. A*, 2021, **9**, 13861–13866.
240 T. Xu, J. Liang, Y. Wang, S. Li, Z. Du, T. Li, Q. Liu, Y. Luo, F. Zhang, X. Shi, B. Tang, Q. Kong, A. M. Asiri, C. Yang, D. Ma and X. Sun, *Nano Res.*, 2022, **15**, 1039–1046.
241 Q. Liu, Y. Lin, S. Gu, Z. Cheng, L. Xie, S. Sun, L. Zhang, Y. Luo, A. A. Alshehri, M. S. Hamdy, Q. Kong, J. Wang and X. Sun, *Nano Res.*, 2022, **15**, 7134–7138.
242 S. Li, Y. Wu, Q. Liu, B. Li, T. Li, H. Zhao, A. A. Alshehri, K. A. Alzahrani, Y. Luo, L. Li and X. Sun, *Inorg. Chem. Front.*, 2021, **8**, 3105–3110.
243 J. Mu, Z. Zhao, X. W. Gao, Z. M. Liu, W. Bin Luo, Z. Sun, Q. F. Gu and F. Li, *Adv. Energy Mater.*, 2024, **14**, 2303558.
244 K. Chen, R. Wang, Q. Mei, F. Ding, H. Liu, G. Yang, B. Bai and Q. Wang, *Appl. Catal., B*, 2024, **344**, 123670.
245 A. Rasyotra, A. Thakur, B. Gaykwad, R. Mandalia, R. Ranganathan and K. Jasuja, *ACS Appl. Mater. Interfaces*, 2024, **16**, 24473–24482.
246 J. Xia, H. Guo, M. Cheng, C. Chen, M. Wang, Y. Xiang, T. Li and E. Traversa, *J. Mater. Chem. A*, 2021, **9**, 2145–2151.
247 Z. Wang, Z. Dai, S. Wang, H. Zhang, W. Tian, Y. Xu, X. Li, L. Wang and H. Wang, *Chem. Eng. J.*, 2021, **416**, 129105.
248 S. Murmu, S. Paul, S. Kapse, R. Thapa, S. Chattopadhyay, A. N., S. N. Jha, D. Bhattacharyya and U. K. Ghorai, *J. Mater. Chem. A*, 2021, **9**, 14477–14484.
249 Y. Wang, M. Batmunkh, H. Mao, H. Li, B. Jia, S. Wu, D. Liu, X. Song, Y. Sun and T. Ma, *Chin. Chem. Lett.*, 2022, **33**, 394–398.
250 M. Liu, S. Yin, T. Ren, Y. Xu, Z. Wang, X. Li, L. Wang and H. Wang, *ACS Appl. Mater. Interfaces*, 2021, **13**, 47458–47464.
251 J. Liang, H. Chen, T. Mou, L. Zhang, Y. Lin, L. Yue, Y. Luo, Q. Liu, N. Li, A. A. Alshehri, I. Shakir, P. O. Agboola, Y. Wang, B. Tang, D. Ma and X. Sun, *J. Mater. Chem. A*, 2022, **10**, 6454–6462.

252 L. Zhang, X. Ji, X. Ren, Y. Ma, X. Shi, Z. Tian, A. M. Asiri, L. Chen, B. Tang, X. Sun, L. Zhang, X. Ji, X. Ren, X. Sun, Y. Ma, X. Shi, B. Tang, Z. Tian, L. Chen and A. M. Asiri, *Adv. Mater.*, 2018, **30**, 1800191.

253 J. Kong, M.-S. S. Kim, R. Akbar, H. S. H. Y. Park, J. H. Jang, H. Kim, K. Hur and H. S. H. Y. Park, *ACS Appl. Mater. Interfaces*, 2021, **13**, 24593–24603.

254 U. K. Ghorai, S. Paul, B. Ghorai, A. Adalder, S. Kapse, R. Thapa, A. Nagendra and A. Gain, *ACS Nano*, 2021, **15**, 5230–5239.

255 H. Y. Zhou, Y. Bin Qu, J. C. Li, Z. L. Wang, C. C. Yang and Q. Jiang, *Appl. Catal., B*, 2022, **305**, 121023.

256 J. Liang, W. F. Hu, B. Song, T. Mou, L. Zhang, Y. Luo, Q. Liu, A. A. Alshehri, M. S. Hamdy, L. M. Yang and X. Sun, *Inorg. Chem. Front.*, 2022, **9**, 1366–1372.

257 Y. Luo, Q. Li, Y. Tian, Y. Liu and K. Chu, *J. Mater. Chem. A*, 2022, **10**, 1742–1749.

258 X. Zhu, J. Zhao, L. Ji, T. Wu, T. Wang, S. Gao, A. A. Alshehri, K. A. Alzahrani, Y. Luo, Y. Xiang, B. Zheng and X. Sun, *Nano Res.*, 2020, **13**, 209–214.

259 K. Chu, Y. Liu, Y. Li, Y. Guo and Y. Tian, *ACS Appl. Mater. Interfaces*, 2020, **12**, 7081–7090.

260 Y. Gu, B. Xi, W. Tian, H. Zhang, Q. Fu, S. Xiong, Y. Gu, B. J. Xi, W. Z. Tian, H. Zhang, Q. Fu and S. L. Xiong, *Adv. Mater.*, 2021, **33**, 2100429.

261 N. Mukherjee, A. Adalder, N. Barman, R. Thapa, R. Urkude, B. Ghosh and U. K. Ghorai, *J. Mater. Chem. A*, 2024, **12**, 3352–3361.

262 S. Ye, Z. Chen, G. Zhang, W. Chen, C. Peng, X. Yang, L. Zheng, Y. Li, X. Ren, H. Cao, D. Xue, J. Qiu, Q. Zhang and J. Liu, *Energy Environ. Sci.*, 2022, **15**, 760–770.

263 Z. Song, Y. Liu, Y. Zhong, Q. Guo, J. Zeng, Z. Geng, Z. Song, Y. Liu, Y. Zhong, J. Zeng, Z. Geng and Q. Guo, *Adv. Mater.*, 2022, **34**, 2204306.

264 X. Li, X. Zhao, Y. Zhou, J. Hu, H. Zhang, X. Hu and G. Hu, *Appl. Surf. Sci.*, 2022, **584**, 152556.

265 M. Jiang, A. Tao, Y. Hu, L. Wang, K. Zhang, X. Song, W. Yan, Z. Tie and Z. Jin, *ACS Appl. Mater. Interfaces*, 2022, **14**, 17470–17478.

266 Y. Xu, K. Ren, T. Ren, M. Wang, Z. Wang, X. Li, L. Wang and H. Wang, *Appl. Catal., B*, 2022, **306**, 121094.

267 M. Liu, Q. Mao, K. Shi, Z. Wang, Y. Xu, X. Li, L. Wang and H. Wang, *ACS Appl. Mater. Interfaces*, 2022, **14**, 13169–13176.

268 Y. Xu, K. Ren, T. Ren, M. Wang, M. Liu, Z. Wang, X. Li, L. Wang and H. Wang, *Chem. Commun.*, 2021, **57**, 7525–7528.

269 Y. Xu, Y. Sheng, M. Wang, T. Liu, H. Yu, K. Deng, Z. Wang, L. Wang and H. Wang, *J. Mater. Chem. A*, 2022, **10**, 16290–16296.

270 Q. Liu, L. Xie, J. Liang, Y. Ren, Y. Wang, L. Zhang, L. Yue, T. Li, Y. Luo, N. Li, B. Tang, Y. Liu, S. Gao, A. A. Alshehri, I. Shakir, P. O. Agboola, Q. Kong, Q. Wang, D. Ma, X. Sun, Q. Liu, L. Xie, Q. Kong, Q. Wang, J. Liang, Y. Ren, L. Zhang, L. Yue, T. Li, Y. Luo, X. Sun, Y. Wang, D. Ma, N. Li, B. Tang, Y. Liu, S. Gao, A. A. Alshehri, I. Shakir and P. O. Agboola, *Small*, 2022, **18**, 2106961.

271 Z. Y. Wu, M. Karamad, X. Yong, Q. Huang, D. A. Cullen, P. Zhu, C. Xia, Q. Xiao, M. Shakouri, F. Y. Chen, J. Y. (Timothy) Kim, Y. Xia, K. Heck, Y. Hu, M. S. Wong, Q. Li, I. Gates, S. Siahrostami and H. Wang, *Nat. Commun.*, 2021, **121**, 1–10.

272 Y. Zhao, Y. Liu, Z. Zhang, Z. Mo, C. Wang and S. Gao, *Nano Energy*, 2022, **97**, 107124.

273 R. Zhang, C. Li, H. Cui, Y. Wang, S. Zhang, P. Li, Y. Hou, Y. Guo, G. Liang, Z. Huang, C. Peng and C. Zhi, *Nat. Commun.*, 2023, **141**, 1–11.

274 Y. Hai, X. Li, Y. Cao, X. Wang, L. Meng, Y. Yang and M. Luo, *ACS Appl. Mater. Interfaces*, 2024, **16**, 11431–11439.

275 S. Luo, H. Guo, T. Li, H. Wu, F. Zhang, C. Tang, G. Chen, G. Yang and Y. Zhou, *Appl. Catal., B*, 2024, **351**, 123967.

276 Y. Luo, K. Chen, P. Shen, X. Li, X. Li, Y. Li and K. Chu, *J. Colloid Interface Sci.*, 2023, **629**, 950–957.

277 Z. Li, J. Liang, Q. Liu, L. Xie, L. Zhang, Y. Ren, L. Yue, N. Li, B. Tang, A. A. Alshehri, M. S. Hamdy, Y. Luo, Q. Kong and X. Sun, *Mater. Today Phys.*, 2022, **23**, 100619.

278 X. Lu, J. Yu, J. Cai, Q. Zhang, S. Yang, L. Gu, G. I. N. Waterhouse, S. Q. Zang, B. Yang and S. Lu, *Cell Rep. Phys. Sci.*, 2022, **3**, 100961.

279 S. Zhang, M. Li, J. Li, Q. Song and X. Liu, *Proc. Natl. Acad. Sci. U. S. A.*, 2022, **119**, e2115504119.

280 X. Fan, J. Liang, L. Zhang, D. Zhao, L. Yue, Y. Luo, Q. Liu, L. Xie, N. Li, B. Tang, Q. Kong and X. Sun, *Carbon Neutralization*, 2022, **1**, 6–13.

281 W. Qiu, X. Chen, Y. Liu, D. Xiao, P. Wang, R. Li, K. Liu, Z. Jin and P. Li, *Appl. Catal., B*, 2022, **315**, 121548.

282 J. Ni, J. Yan, F. Li, H. Qi, Q. Xu, C. Su, L. Sun, H. Sun, J. Ding and B. Liu, *Adv. Energy Mater.*, 2024, **14**, 2400065.

283 T. Ren, K. Ren, M. Wang, M. Liu, Z. Wang, H. Wang, X. Li, L. Wang and Y. Xu, *Chem. Eng. J.*, 2021, **426**, 130759.

284 D. Zhao, C. Ma, J. Li, R. Li, X. Fan, L. Zhang, K. Dong, Y. Luo, D. Zheng, S. Sun, Q. Liu, Q. Li, Q. Lu and X. Sun, *Inorg. Chem. Front.*, 2022, **9**, 6412–6417.

285 X. Fan, D. Zhao, Z. Deng, L. Zhang, J. Li, Z. Li, S. Sun, Y. Luo, D. Zheng, Y. Wang, B. Ying, J. Zhang, A. A. Alshehri, Y. Lin, C. Tang, X. Sun and Y. Zheng, *Small*, 2023, **19**, 2208036.

286 H. Wang, D. Zhao, C. Liu, X. Fan, Z. Li, Y. Luo, D. Zheng, S. Sun, J. Chen, J. Zhang, Y. Liu, S. Gao, F. Gong and X. Sun, *J. Mater. Chem. A*, 2022, **10**, 24462–24467.

287 Z. Niu, S. Fan, X. Li, Z. Liu, J. Wang, J. Duan, M. O. Tadé and S. Liu, *ACS Appl. Mater. Interfaces*, 2022, **14**, 35477–35484.

288 Z. Deng, C. Ma, Z. Li, Y. Luo, L. Zhang, S. Sun, Q. Liu, J. Du, Q. Lu, B. Zheng and X. Sun, *ACS Appl. Mater. Interfaces*, 2022, **14**, 46595–46602.

289 T. H. Jeon, Z.-Y. Wu, F.-Y. Chen, W. Choi, P. J. J. Alvarez and H. Wang, *J. Phys. Chem. C*, 2022, **126**, 6982–6989.

290 Q. Liu, G. Wen, D. Zhao, L. Xie, S. Sun, L. Zhang, Y. Luo, A. Ali Alshehri, M. S. Hamdy, Q. Kong and X. Sun, *J. Colloid Interface Sci.*, 2022, **623**, 513–519.

291 Y. Guo, R. Zhang, S. Zhang, Y. Zhao, Q. Yang, Z. Huang, B. Dong and C. Zhi, *Energy Environ. Sci.*, 2021, **14**, 3938–3944.

292 X. Li, P. Shen, X. Li, D. Ma and K. Chu, *ACS Nano*, 2023, **17**, 1081–1090.